Available online at www.sciencedirect.com

SciVerse ScienceDirect

Procedia Engineering 00 (2012) 000–000

Procedia Engineering

www.elsevier.com/locate/procedia

5th BSME International Conference on Thermal Engineering

Numerical Study of Fluid Flow on Magneto-Hydrodynamic Mixed Convection in a Lid Driven Cavity Having a Heated Circular Hollow Cylinder

S.K. Farid[a,b]*, M. M. Billah[b,d], M. M. Rahman[c], Uddin Md. Sharif[b]

[a]Mirpur Girls Ideal Laboratory Institute, Mirpur-10, Dhaka-1216, Bangladesh
[b]Department of Mathematics
Jahangirnagar University, Savar, Dhaka-1342, Banglsdesh
[c]Department of Mathematics
Bangladesh University of Engineering and Technology (BUET), Dhaka-1000, Bangladesh
[d]Department of Arts and Sciences
Ahsanullah University of Science and Technology (AUST), Dhaka-1208, Bangladesh

Abstract

Magneto-hydrodynamic mixed convection in a lid driven cavity along with a heated circular hollow cylinder positioned at the centre of the cavity is studied numerically. The left and right vertical walls are kept at a constant temperature T_c while the top and bottom horizontal walls of the cavity are insulated. The left vertical wall is moving in its own plane of a constant speed while all other walls are fixed. A uniform magnetic field is applied to the horizontal direction normal to the moving wall. A Galerkin weighted residual finite element method with a Newton Raphson iterative algorithm is adopted to solve the governing equations. The computations are carried out for wide ranges of the Hartmann number (*Ha*) and Richardson number (*Ri*). The results are presented in the form of streamlines, isothermal lines and average Nusselt number for the aforementioned parameters. The results show that the aforesaid parameters have noticeable effect on the flow pattern and heat transfer characteristics inside the cavity.

Keywords: Magneto-hydrodynamic, mixed convection, lid-driven cavity, hollow cylinder, and finite element method.

Nomenclature

B_0	magnetic field strength	(x, y)	dimensional coordinates (m)
C_p	Specific heat of fluid at constant pressure	(X, Y)	dimensionless coordinates
g	gravitational acceleration (ms^{-2})	*Greek symbols*	
Ha	Hartmann number	α	thermal diffusivity (m^2s^{-1})
k	thermal conductivity of fluid ($Wm^{-1}K^{-1}$)	β	thermal expansion coefficient (K^{-1})
k_s	thermal conductivity of solid ($Wm^{-1}K^{-1}$)	θ	non-dimensional temperature
K	thermal conductivity ratio of the solid and fluid	μ	dynamic viscosity of the fluid (Kg $m^{-1}s^{-1}$)
L	length of the cavity (m)	ν	kinematic viscosity of the fluid (m^2s^{-1})
Nu	Nusselt number	σ	electrical conductivity of the fluid ($Wm^{-1}K^{-1}$)
p	dimensional pressure (Nm^{-2})	ρ	density of the fluid (Kg m^{-3})
P	non-dimensional pressure	ψ	stream function
Pr	Prandtl number	*subscripts*	
Re	Reynolds number	*c*	less heated wall
Ri	Richardson number	*h*	heated wall
T	dimensional temperature (K)	*s*	solid
u, v	velocity components (ms^{-1})		
U, V	non-dimensional velocity components		

* Corresponding author. Tel.: +8801670847730; fax:
E-mail address: sheikh.farid94@gmail.com

1. Introduction

Mixed convection is that type of heat transfer in which there is a noteworthy interaction between free and forced convection. Analysis of mixed convection in a lid-driven cavity is relevant to much engineering and environmental applications. These applications include heat exchanger, cooling of electronic equipments, nuclear reactors, solar receiver, thermal storage, chemical processing equipments and drying or geophysics studies, etc. Studies associated with mixed convection in open cavities have received increasing consideration. Literature on the body inserted lid-driven cavity is sparse. Dagtekin and Oztop, 2002 inserted an isothermally heated rectangular block in a lid-driven cavity at different positions to simulate the cooling of electronic equipments. The authors concluded that dimension of the body is the most effective parameter on mixed convection flow. Mamun et al, 2010 performed a numerical study on the effect of a heated hollow cylinder on mixed convection in a ventilated cavity.

Magneto-hydrodynamics (MHD) is that branch of science, which studies the dynamics of electrically conducting fluids in the presence of electromagnetic fields. MHD is usually regarded as a very up to the date subject, because it has many engineering applications such as liquid-metal cooling of nuclear reactors and electromagnetic casting, etc. Rahman et al, 2009 investigated the effect of a heat conducting horizontal circular cylinder on MHD mixed convection in a lid-driven cavity along with joule heating. MHD mixed convection flow in a vertical lid-driven square enclosure, including a heat conducting horizontal circular cylinder with Joule heating was analyzed by Rahman and Alim, 2010. Piazza and Ciofalo, 2002 carried out a numerical investigation on buoyancy-driven magneto-hydrodynamic flow in a liquid-metal filled in a cubic enclosure. The authors found that increasing Hartmann number suppressed the convective motions. Chamkha, 2002 made a study for mixed convection in a square cavity in the presence of magnetic field and an internal heat generation and absorption. He concluded that the flow behavior inside the cavity and heat transfer rate is strongly affected by the magnetic field. Xu et al, 2006 completed an experimental study on natural convection of a molten metal contained in a rectangular enclosure in the presence of an external magnetic field. Oztop et al, 2009 studied the effects of sinusoidal temperature boundary conditions on magnetohydrodynamic buoyancy-induced flow in a non-isothermally heated square enclosure. Sarries et al, 2005 performed a numerical study on unsteady natural convection of an electrically conducting fluid in a laterally and volumetrically heated square cavity under the influence of a magnetic field. Rahman et al, 2010 conducted a numerical study on the conjugate effect of joule heating and magnato-hydrodynamics mixed convection in an obstructed lid-driven square cavity, where the developed mathematical model was solved by employing Galerkin weighted residual method of finite element formulation. Bhuvaneswari et al, 2011 carried out a computational study of convective flow and heat transfer in a cavity in the presence of uniform magnetic field. Rahman et al, 2010 investigated the effect of Reynolds and Prandtl numbers effects on MHD mixed convection in a lid-driven cavity along with joule heating and a centered heat conducting circular block.

As it is clear from the above literature that the combined heat transfer by mixed convection in a lid-driven cavity has been received a great interest in recent years. Nevertheless, to the best knowledge of the authors, combined heat transfer by MHD mixed convection in a lid-driven cavity with heated circular hollow cylinder has received a little attention in the literature. The main purpose of this study is to examine the MHD mixed convection heat transfer and fluid flow and effects of magnetic force in a lid driven cavity for different Richardson number.

2. Physical Model

The physical system under study with the system of coordinates is sketched in Fig. 1. The problem deals with a heated circular hollow cylinder with a diameter d and thermal conductivity k_s located at the center of a square enclosure with sides of length L. The two sidewalls are maintained at uniform constant temperatures T_c, while the horizontal top and bottom walls are adiabatic. The left vertical wall of the cavity is allowed to move upward in its own plane at a constant velocity V_0, while the other walls remain stationary. In addition, the gravity acts in the negative y-direction. Moreover, the radiation, pressure work and viscous dissipation are assumed to be negligible and Boussinesq approximation is assumed to be valid. Magnetic force is induced in the horizontal direction to the cavity. All solid boundaries are assumed to be rigid no-slip walls.

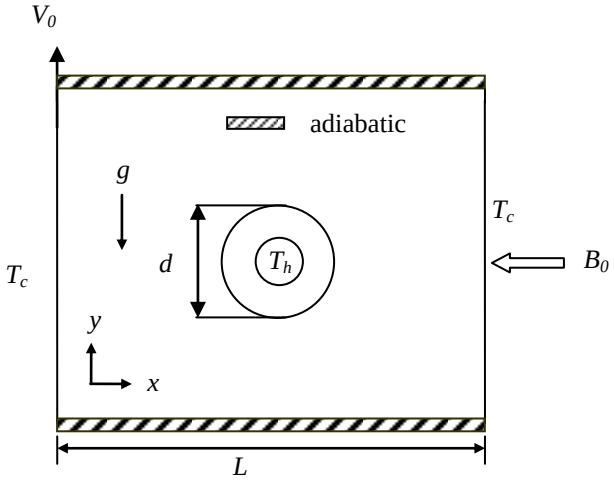

Fig. 1. Schematic of the problem with the domain

3. Mathematical Formulation

The governing equations for this investigation are based on the usual balance laws of mass, momentum and energy modified to account for combined buoyancy effects, and hydromagnetic effects. The flow is considered steady, laminar, incompressible and two-dimensional. The variation of fluid properties with temperature has been neglected with the only exception of the buoyancy term, for the Boussinesq approximation has been adopted. The governing equations and the boundary conditions are thrown in the dimensionless form using the following dimensionless variables:

$$X=\frac{x}{L},\ Y=\frac{y}{L},\ U=\frac{u}{V_0},\ V=\frac{v}{V_0},\ P=\frac{p}{\rho {V_0}^2},\ D=\frac{d}{L},\ \theta=\frac{(T-T_c)}{(T_h-T_c)},\ \theta_s=\frac{(T_s-T_c)}{(T_h-T_c)}$$

Taking into account the above-mentioned assumptions, the non-dimensional governing equations are as follows:

$$\frac{\partial U}{\partial X}+\frac{\partial V}{\partial Y}=0 \tag{1}$$

$$U\frac{\partial U}{\partial X}+V\frac{\partial U}{\partial Y}=-\frac{\partial P}{\partial X}+\frac{1}{Re}\left(\frac{\partial^2 U}{\partial X^2}+\frac{\partial^2 U}{\partial Y^2}\right) \tag{2}$$

$$U\frac{\partial V}{\partial X}+V\frac{\partial V}{\partial Y}=-\frac{\partial P}{\partial Y}+\frac{1}{Re}\left(\frac{\partial^2 V}{\partial X^2}+\frac{\partial^2 V}{\partial Y^2}\right)+Ri\,\theta-\frac{Ha^2}{Re}V \tag{3}$$

$$U\frac{\partial \theta}{\partial X}+V\frac{\partial \theta}{\partial Y}=\frac{1}{RePr}\left(\frac{\partial^2 \theta}{\partial X^2}+\frac{\partial^2 \theta}{\partial Y^2}\right) \tag{4}$$

For solid region, the energy equation is

$$\frac{\partial^2 \theta_s}{\partial X^2}+\frac{\partial^2 \theta_s}{\partial Y^2}=0 \tag{5}$$

The non-dimensional parameters that appear in the above formulation are the Reynolds number ($Re=V_0L/\upsilon$), Prandtl number ($Pr=\nu/\alpha$), Richardson number ($Ri=g\beta\Delta TL/{V_0}^2$), Hartmann number ($Ha^2=\frac{\sigma B_0^2 L^2}{\mu}$) and solid fluid thermal conductivity ratio $\left(K=k_s/k_f\right)$,

The boundary conditions used in the current study are

At the left vertical lid: $U=0, V=1, \theta=0$

At the right vertical wall: $U=0, V=0, \theta=0$

At the top and bottom walls: $U=0,\ V=0,\ \frac{\partial \theta}{\partial N}=0$

At the outer surface of the hollow cylinder: $\begin{cases} U=0, V=0 \\ \left(\frac{\partial\theta}{\partial N}\right)_{fluid} = K\left(\frac{\partial\theta_s}{\partial N}\right)_{solid} \end{cases}$

At the inner surface of the hollow cylinder: $U=0, V=0, \theta=1$. Here N is the non-dimensional distances either along X or Y direction acting normal to the surface. The average Nusselt number at the heated surface of the cylinder based on the dimensionless quantities may be expressed by $Nu = -\frac{1}{\pi}\int_0^{\pi}\frac{\partial\theta}{\partial n}d\varphi$ and the average temperature of the fluid in the cavity is defined by $\theta_{av} = \int\theta d\overline{V}/\overline{V}$, where n represents the unit normal vector on the surface of the cylinder and $\overline{V}$ is the cavity volume. The stream function is calculated from its definition as

$U = \frac{\partial\psi}{\partial Y}, V = -\frac{\partial\psi}{\partial X}.$

4. Solution Scheme

The governing equations have been solved by using the Galerkin weighted residual finite element technique. The basic unknowns for the governing equations are the velocity components (U, V), the temperature θ and the pressure P. The six node triangular element is used in this work for the development of the finite element equations. All six nodes are associated with velocities as well as temperature; only the corner nodes are associated with pressure. This means that a lower order polynomial is chosen for pressure and, which is satisfied through continuity equation. The velocity component and the temperature distributions and linear interpolation for the pressure distribution according to their highest derivative orders in the differential equations (2) - (5) can be expressed as

$U(X,Y) = N_\beta U_\beta$, $V(X,Y) = N_\beta V_\beta$, $\theta(X,Y) = N_\beta\theta_\beta$, $\theta_s(X,Y) = N_\beta\theta_{s_\beta}$, $P(X,Y) = H_\lambda P_\lambda$, where β = 1, 2, … … , 6; λ = 1, 2, 3.

Substituting the element velocity component distributions, the temperature distribution and the pressure distribution from equations (2) - (5) the finite element equations can be written in the form

$$K_{\alpha\beta\gamma x}U_\beta U_\gamma + K_{\alpha\beta\gamma y}V_\gamma U_\gamma + M_{\alpha\mu x}P_\mu + \frac{1}{Re}\left(S_{\alpha\beta xx} + S_{\alpha\beta yy}\right)U_\beta = Q_{\alpha u} \quad (6)$$

$$K_{\alpha\beta\gamma x}U_\beta V_\gamma + K_{\alpha\beta\gamma y}V_\gamma V_\gamma + M_{\alpha\mu y}P_\mu + \frac{1}{Re}\left(S_{\alpha\beta xx} + S_{\alpha\beta yy}\right)V_\beta - Ri\,K_{\alpha\beta}\theta_\beta = Q_{\alpha v} \quad (7)$$

$$K_{\alpha\beta\gamma x}U_\beta\theta_\gamma + K_{\alpha\beta\gamma y}V_\beta\theta_\gamma + \frac{1}{RePr}\left(S_{\alpha\beta xx} + S_{\alpha\beta yy}\right)\theta_\beta = Q_{\alpha\theta} \quad (8)$$

$$\left(S_{\alpha\beta xx} + S_{\alpha\beta yy}\right)\theta_\beta = Q_{\alpha\theta_s} \quad (9)$$

where the coefficients in element matrices are in the form of the integrals over the element area and along the element edges S_0 and S_w as

$K_{\alpha\beta x} = \int_A N_\alpha N_{\beta,x}dA$; $K_{\alpha\beta y} = \int_A N_\alpha N_{\beta,y}dA$; $K_{\alpha\beta\gamma x} = \int_A N_\alpha N_\beta N_{\gamma,x}dA$; $K_{\alpha\beta\gamma y} = \int_A N_\alpha N_\beta N_{\gamma,y}dA$

$K_{\alpha\beta} = \int_A N_\alpha N_\beta dA$; $S_{\alpha\beta xx} = \int_A N_{\alpha,x}N_{\beta,x}dA$; $S_{\alpha\beta yy} = \int_A N_{\alpha,y}N_{\beta,y}dA$; $M_{\alpha\mu x} = \int_A H_\alpha H_{\mu,x}dA$

$M_{\alpha\mu y} = \int_A H_\alpha H_{\mu,y}dA$; $Q_{\alpha u} = \int_{S_0} N_\alpha S_x dS_0$; $Q_{\alpha v} = \int_{S_0} N_\alpha S_y dS_0$; $Q_{\alpha\theta} = \int_{S_w} N_\alpha q_{1w}dS_w$; $Q_{\alpha\theta s} = \int_{S_w} N_\alpha q_{2w}dS_w$

The set of non-linear algebraic equations (6) - (9) are solved using reduced integration technique and Newton-Raphson method The convergence of solutions is assumed when the relative error for each variable between consecutive iterations is recorded below the convergence criterion ε such that $\left|\Psi^{n+1} - \Psi^n\right| \le 10^{-4}$, n is number of iteration and Ψ is a function of U, V, θ and θ_s.

5. Findings

A numerical study has been performed to determine the effects of magnetic force on the mixed convection flow of an electrically conducting fluid in a lid-driven cavity. For the intention of discussing the results, the numerical calculations are presented in the form of streamlines, isotherms. With this aim, different parameters such as Reynolds number (*Re*), Prandtl number (*Pr*), Richardson number (*Ri*), Hartmann number (*Ha*) and cylinder diameter (D) are considered. Moreover, Prandtl number, Richardson number and Reynolds number are held fixed at 0.7, 1.0 and 100 respectively.

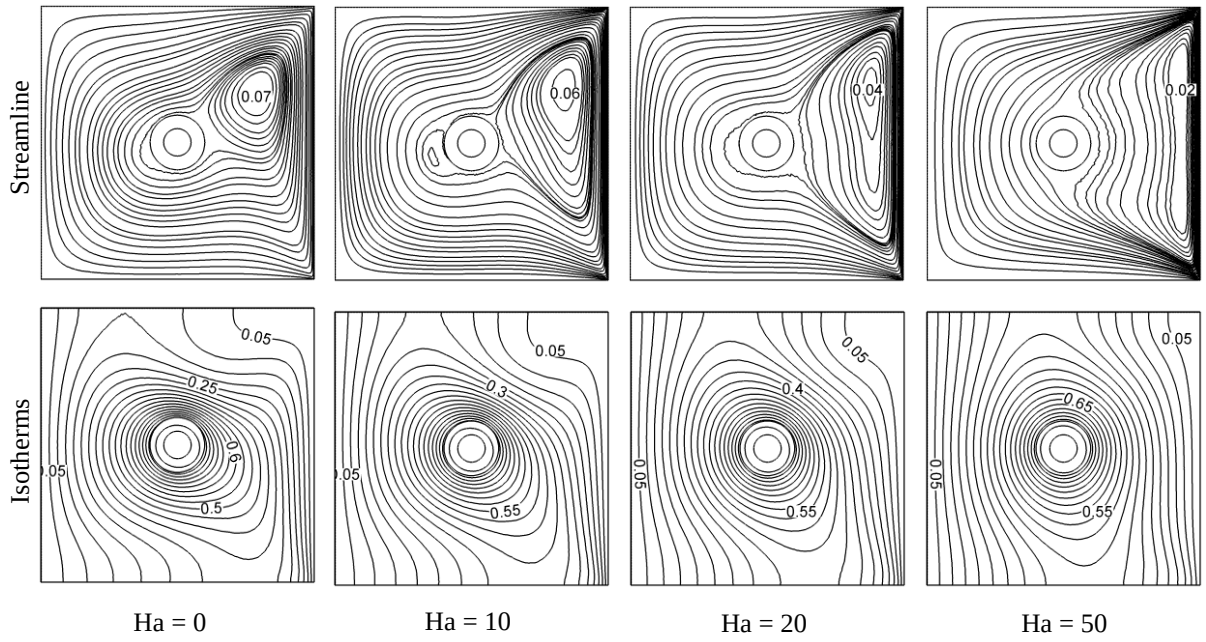

Fig. 2. Effect of Hartmann number on streamlines and isotherms, while Ri = 1.

Fig. 2 shows the streamlines and isotherms for different values of Hartmann number *Ha* = 10, 20, 50 and 100 at *Ri* = 1. As seen from the first row of this figure, an amount of fluid near the heated hollow cylinder in the cavity is activated so as to create a buoyancy-induced clockwise rotating cell for the lowest value of *Ha* = 0. It is also observed that the uni-cellular clockwise eddy appears near the right vertical wall, which we call primary eddy, is generated due to the motion of the left vertical wall. As the Hartmann number increases the strength of the rotating cell is reduced and pushed to the right wall of the cavity indicating the establishment of conduction mode of heat transfer. One may notice that the shape of the cell changes from circular to elliptic with the increasing Ha. As the value of *Ha* increases the core vortices expand vertically. It indicates the reduction of the flow strength of those vortices. The corresponding effect of Hartmann number *Ha* on the isotherms is depicted in the second row of Fig. 2. The temperature field shows that in the absence of magnetic field the isothermal lines form a thin thermal boundary layer near the vicinity of the heated hollow circular cylinder inside the cavity. In addition, from this figure it can easily be seen that the isotherms are almost parallel to the vertical walls for the highest value of *Ha* (= 50.0) at the three values of *Ri*, indicating that most of the heat transfer process is carried out by conduction.

The effect of Hartmann number on average Nusselt number *Nu* at the hot surface and average temperature θ of the fluid in the cavity with Richardson number is shown in the Fig. 3. The average Nusselt number *Nu* decreases with increasing *Ha* for all *Ri*. Moreover, in absence of magnetic field (*Ha* = 0), *Nu* is always higher for all *Ri*. On the other hand, average temperature θ of the fluid in the cavity increases with increasing *Ha* for lower values of *Ri* (= 0.1 and 1).

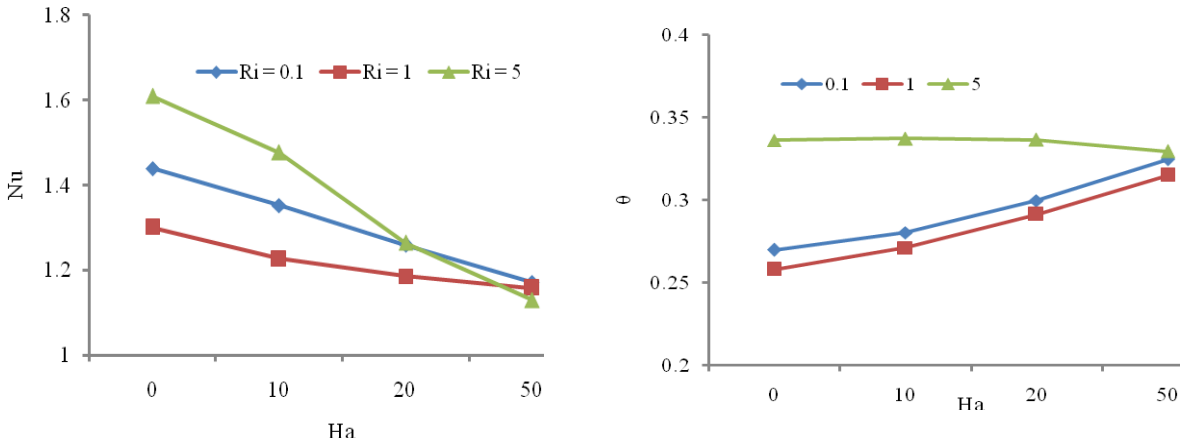

Fig. 3. Effect of Hartmann number *Ha* on average Nusselt number (left) and average fluid temperature in the cavity (right).

6. Concluding Remarks

A computational study is performed to investigate the MHD mixed convection flow in a lid driven enclosure with circular heated hollow cylinder. Results are obtained for wide ranges of Hartmann number *Ha*. The main findings from this work can be listed as follows.

- Flow velocity is reduced with increasing of Hartmann number, and this reduces flow strength and heat transfer. Thus, magnetic field can be a control parameter for heat transfer and fluid flow in lid-driven cavity.
- Thinner thermal boundary layer is observed for lower values of Hartmann numbers.

Higher heat transfer is formed for lower Hartmann number.

Acknowledgements

The authors like to express their gratitude to the department of mathematics, Jahangirnagar University, Savar, Dhaka-1342, Banglsdesh.

References

[1] Dagtekin, I., Oztop HF., 2002. "Mixed convection in an enclosure with a vertical heated block located''. In: Proceeding of ESDA2002: Sixth Biennial Conference on Engineering Systems Design and Analysis, p. 1-8.

[2] Mamun, MAH. M., Rahman, MM., Billah, MM., Saidur, R., 2010. A numerical study on the effect of a heated hollow cylinder on mixed convection in a ventilated cavity. Int. Comm. in Heat and Mass Transfer.37, p. 1326–34.

[3] Rahman, MM., Mamun, MAH., Saidur, R.,2009. Shuichi Nagata. Effect of a heat conducting horizontal circular cylinder on MHD mixed convection in a lid-driven cavity along with joule heating. Int J of Mechanical and Materials 4, p. 256-65.

[4] Rahman, MM., Alim, MA., 2010. MHD mixed convection flow in a vertical lid-driven square enclosure including a heat conducting horizontal circular cylinder with Joule heating, Nonlinear Analysis: Modelling and Control 15, p.199–211.

[5] Piazza, ID., Ciofalo, M., 2002. MHD free convection in a liquid-metal filled cobic enclosure I Differential heating, Int J Heat Mass Transfer. 45, p. 1477–92.

[6] Chamkha, AJ., 2002. Hydromagnetic combined convection flow in a vertical lid-driven cavity with internal heat generation or absorption. Numer Heat Transfer. 41, p. 529-46.

[7] Xu, B., Li, BQ., Stock, DE., 2006. An experimental study of thermally induced convection of molten gallium in magnetic fields. Int J Heat Mass Transfer. 49, p. 2009–19.

[8] Oztop, HF., Oztop, M., Varol, Y., 2009. Numerical simulation of Magnetohydrodynamic buoyancy-induced flow in a non-isothermally heated square enclosure. Commun. Nonlinear Sci. and Numer. Simulations. 14, p. 770-78.

[9] Sarries, IE., Kakarantzas, SC., Grecos, AP., Vlachos, NS., 2005. MHD natural convection in a laterally and volumetrically heated square cavity. Int J Heat Mass Transfer. 48, p. 3443–53.

[10] Rahman, MM., Alim, MA., Sarker, MMA., 2010. Numerical study on the conjugate effect of joule heating and magnato-hydrodynamics mixed convection in an obstructed lid-driven square cavity. Int Commun. Heat and Mass Transfer. 37, p. 524-34.

[11] Bhuvaneswari, M., Sivasankaran, S., Kim, YJ., 2011. Magnetoconvection in a square enclosure with sinusoidal temperature distributions on both side walls, Numer. Heat Transfer A. 59, p. 167-84.

[12] Rahman, MM., Billah, MM., Mamun, MAH., Saidur, R., Hassanuzzaman, M., 2010. Reynolds and Prandtl numbers effects on MHD mixed convection in a lid-driven cavity along with joule heating and a centered heat conducting circular block. Int J Mechanical and Materials Engineering. 2, p. 163-70.

Available online at www.sciencedirect.com

SciVerse ScienceDirect

Procedia Engineering 00 (2012) 000–000

Procedia Engineering

www.elsevier.com/locate/procedia

5th BSME International Conference on Thermal Engineering

Double Diffusive Natural Convective Flow Characteristics in a Cavity

Salma Parvin*, Rehena Nasrin, M.A. Alim, N.F. Hossain

Department of Mathematics, Bangladesh University of Engineering & Technology, Dhaka-1000, Bangladesh

Abstract

The influences of Soret and Dufour coefficients on free convection flow phenomena in a partially heated square cavity filled with water-Al_2O_3 nanofluid is studied numerically. The top surface has constant temperature T_c, while bottom surface is partially heated T_h, with $T_h > T_c$. The concentration in top wall is maintained higher than bottom wall ($C_c < C_h$). The remaining bottom wall and the two vertical walls are considered adiabatic. Water is considered as the base fluid. By Penalty Finite Element Method the governing equations are solved. The effect of the Soret and Dufour coefficients on the flow pattern and heat and mass transfer has been depicted. Comprehensive average Nusselt and Sherwood numbers, average temperature and concentration and mid-height horizontal and vertical velocities inside the cavity are presented as a function of the governing parameters. Results shows that both heat and mass transfer increased by Soret and Dufour coefficients.

Keywords: Soret and Dufour coefficients, double-diffusive natural convection, finite element method, water-Al_2O_3 nanofluid.

Nomenclature

c	Dimensional concentration (kg m^{-3})
C	Non-dimensional concentration
C_p	Specific heat at constant pressure (kJ kg^{-1} K^{-1})
C_s	Concentration susceptibility
D	Solutal diffusivity (m^2 s^{-1})
D_f	Dufour parameter
g	Gravitational acceleration (m s^{-2})
h	Local heat transfer coefficient (W m^{-2} K^{-1})
k	Thermal conductivity (W m^{-1} K^{-1})
K_T	Thermal diffusion ratio
L	Lengh of the enclosure (m)
Nu	Nusselt number,
Pr	Prandtl number
Sc	Schmidt number
Sh	Sherwood number
S_r	Soret parameter

* Corresponding author. Tel.: 880-9665650-ext 7912.
E-mail address: salpar@math.buet.ac.bd

Ra	Rayleigh number
T	Dimensional temperature (^{o}K)
u, *v*	Dimensional *x* and *y* components of velocity (m s^{-1})
U, *V*	Dimensionless velocities, $U = u / L, \quad V = v / L$
X, *Y*	Dimensionless coordinates, $X = x / L, \quad Y = y / L$
x, *y*	Dimensional coordinates (m)
Greek Symbols	
α	Fluid thermal diffusivity (m^2 s^{-1})
β	Thermal expansion coefficient (K^{-1})
ϕ	Nanoparticles volume fraction
θ	Dimensionless temperature
μ	Dynamic viscosity (N s m^{-2})
ν	Kinematic viscosity (m^2 s^{-1})
ρ	Density (kg m^{-3})
Subscripts	
av	average
c	cold
f	fluid
h	hot
m	mean
nf	nanofluid
s	solid particle

1. Introduction

The natural convection in enclosures continues to be a very active area of research during the past few decades. While a good number of works have made significant contributions for the development of the theory, an equally good number of works have been devoted to many engineering applications that include electronic or computer equipment, thermal energy storage systems and etc.

Double diffusive convection of water has been studied by Nithyadevi and Yang [1] and Sivasankaran and Kandaswamy [2, 3]. Yet, most work done considers flow inside closed enclosures, the applications included, such as pollution dispersion inlakes, chemical deposition, and melting and solidification process. Diffusion of matter caused by temperature gradients (Soret effect) and diffusion of heat caused by concentration gradients (Dufour effect) become very significant when the temperature and concentration gradients are very large. Generally these effects are considered as second order phenomenon. These effects may become important in some applications such as the solidification of binary alloys, groundwater pollutant migration, chemical reactors, and geosciences. The importance of these effects has also seen in Mansour et al. [4], Platten [5] and Patha et al. [6].

Double diffusive and Soret induced convection in a shallow horizontal enclosure is studied numerically by Mansour et al. [4]. They found that the Nusselt number has decreases in general with the Soret parameter while the Sherwood number increases or decreases with this parameter depending on the temperature gradient induced by each solution.

In the above studies convection heat transfer is due to the imposed temperature gradient between the opposing walls of the enclosure taking the entire vertical wall to be thermally active. But in many naturally occurring situations and engineering applications it is only a part of the wall which is thermally active. For example in solar energy collectors due to shading, it is only the unshaded part of the wall that is thermally active. In order to have the results to possess applications, it is essential to study heat transfer in an enclosure with partially heated active walls. Only a few studies are reported in the literature concerning heat transfer in enclosures with partially heated side walls, by Oztop [7] and Erbay et al. [8].

Natural convection in an enclosure with partially active walls is studied by Nithyadevi et al. [9] and Kandaswamy et al. [10] without Soret and Dufour effects. Present study deals with the natural convection in a square enclosure filled with water and partially heated vertical walls for three different combinations of heating location in the presence of solute concentration with Soret and Dufour effects. The hot region is located at the top, middle and bottom of the left vertical wall of the enclosure.

Oztop and Abu-Nada [11] numerically studied natural convection in partially heated rectangular enclosures filled with nanofluids. Rouboa et al. [12] analyzed convective heat transfer in nanofluid. Esfahani and Bordbar [13] studied double diffusive natural convection heat transfer enhancement in a square enclosure using nanofluids. Gorla et al. [14] analyzed mixed convective boundary layer flow over a vertical wedge embedded in a porous medium saturated with a nanofluid:

Natural Convection Dominated Regime. Kuznetsov and Nield [15] performed double-diffusive natural convective boundary-layer flow of a nanofluid past a vertical plate where similarity solution was performed in order to obtain correlation formulas giving the reduced Nusselt number as a function of the various relevant parameters. The stability boundaries for both non-oscillatory and oscillatory cases had been approximated by simple analytical expressions. For the porous medium the Darcy model is employed.

Effects of Soret Dufour, chemical reaction and thermal radiation on MHD non-Darcy unsteady mixed convective heat and mass transfer over a stretching sheet was investigated by Pal and Mondal [16]. The author used shooting algorithm with Runge–Kutta–Fehlberg integration scheme to solve the governing equations. Natural convection heat transfer of nanofluids in a vertical cavity: Effects of non-uniform particle diameter and temperature on thermal conductivity was performed by Lin and Violi [17]. Moreover, Saleh et al. [18] studied natural convection heat transfer in a nanofluid-filled trapezoidal enclosure. They found that acute sloping wall and Cu nanoparticles with high concentration were effective to enhance the rate of heat transfer.

The present work discussed the effect of Soret and Dufour parameter on double diffusive natural convection in a partially heated cavity. The results are presented in the form of streamlines, isotherms, average Nusselt number Nu and average Sherwood number Sh, average temperature of the fluid and mid height velocity in the cavity for relevant parameter.

2. Physical Model

Fig. 1 shows a schematic diagram of a partially heated square enclosure. The fluid in the cavity is water-based nanofluid containing Al_2O_3 nanoparticles with Soret and Dufour coefficients. The nanofluid is assumed incompressible and the flow is considered to be laminar. It is taken that water and nanoparticles are in thermal equilibrium and no slip occurs between them. The top horizontal wall has constant temperature T_c, while bottom wall is partially heated T_h, with $T_h > T_c$. The concentration in top wall is maintained higher than bottom wall ($C_c < C_h$). The remaining bottom wall and the two vertical walls are considered adiabatic. The thermophysical properties of the nanofluid are taken from Saleh et al. [18] and given in Table 1. The density of the nanofluid is approximated by the Boussinesq model.

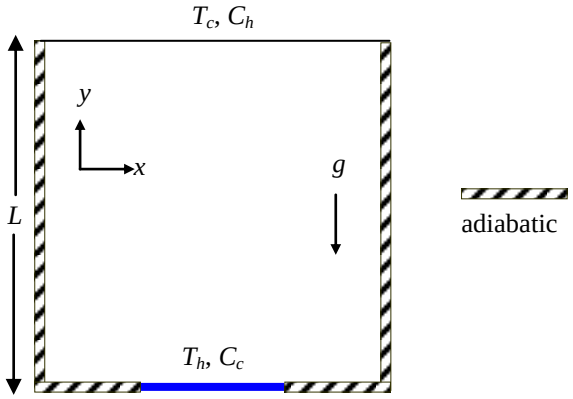

Fig. 1: Schematic diagram of the enclosure

Table 1. Thermo physical properties of fluid and nanoparticles [18]

Physical Properties	Fluid phase (Water)	Al_2O_3
C_p(J/kgK)	4179	765
ρ (kg/m^3)	997.1	3600
k (W/mK)	0.6	46
$\beta\times10^{-5}$ (1/K)	21	0.63

3. Governing Equations

The governing equations for laminar natural convection in a cavity filled with water-alumina nanofluid in terms of the

Navier-Stokes and energy equation (non dimensional form) are given as:

$$\frac{\partial U}{\partial X}+\frac{\partial V}{\partial Y}=0$$

$$U\frac{\partial U}{\partial X}+V\frac{\partial U}{\partial Y}=-\frac{\rho_f}{\rho_{nf}}\frac{\partial P}{\partial X}+Pr\frac{\nu_{nf}}{\nu_f}\left(\frac{\partial^2 U}{\partial X^2}+\frac{\partial^2 U}{\partial Y^2}\right)$$

$$U\frac{\partial V}{\partial X}+V\frac{\partial V}{\partial Y}=-\frac{\rho_f}{\rho_{nf}}\frac{\partial P}{\partial Y}+Pr\frac{\nu_{nf}}{\nu_f}\left(\frac{\partial^2 V}{\partial X^2}+\frac{\partial^2 V}{\partial Y^2}\right)+Ra\,Pr\frac{(1-\phi)\rho_f\beta_f+\phi\rho_s\beta_s}{\rho_{nf}\beta_f}(\theta+C)$$

$$U\frac{\partial \theta}{\partial X}+V\frac{\partial \theta}{\partial Y}=\frac{1}{Pr}\left(\frac{\partial^2 \theta}{\partial X^2}+\frac{\partial^2 \theta}{\partial Y^2}\right)+D_f\left(\frac{\partial^2 C}{\partial X^2}+\frac{\partial^2 C}{\partial Y^2}\right)$$

$$U\frac{\partial C}{\partial X}+V\frac{\partial C}{\partial Y}=\frac{1}{Sc}\left(\frac{\partial^2 C}{\partial X^2}+\frac{\partial^2 C}{\partial Y^2}\right)+S_r\left(\frac{\partial^2 \theta}{\partial X^2}+\frac{\partial^2 \theta}{\partial Y^2}\right)$$

The corresponding boundary conditions take the following form:

at all solid boundaries $U = V = 0$

at $Y = 0,\ 0.3 \le X \le 0.7,\quad \theta = 1,\ C = 0$

at $Y = 1,\quad \theta = 0,\ C = 1$

at the remaining boundaries $\frac{\partial \theta}{\partial N}=0,\ \frac{\partial C}{\partial N}=0$

the following dimensionless dependent and independent variables

$X=\frac{x}{L},\quad Y=\frac{y}{L},\quad U=\frac{uL}{\nu_f},\quad V=\frac{vL}{\nu_f},\quad P=\frac{pL^2}{\rho_f{\nu_f}^2},\quad \theta=\frac{T-T_c}{T_h-T_c},\ C=\frac{c-C_c}{C_h-C_c}$ are used to make the above equations non-dimensional.

where, $\rho_{nf}=(1-\phi)\rho_f+\phi\rho_s$ is the density,

$(\rho C_p)_{nf}=(1-\phi)(\rho C_p)_f+\phi(\rho C_p)_s$ is the heat capacitance,

$\beta_{nf}=(1-\phi)\beta_f+\phi\beta_s$ is the thermal expansion coefficient,

$\alpha_{nf}=k_{nf}/(\rho C_p)_{nf}$ is the thermal diffusivity,

the dynamic viscosity of Brinkman model [19] is $\mu_{nf}=\mu_f(1-\phi)^{-2.5}$

and the thermal conductivity of Maxwell Garnett (MG) model [20] is $k_{nf}=k_f\frac{k_s+2k_f-2\phi(k_f-k_s)}{k_s+2k_f+\phi(k_f-k_s)}$,

Prandtl number $Pr=\left(\frac{\nu}{\alpha}\right)_f$, Schmidt number $Sc=\left(\frac{\nu}{D}\right)_f$, thermal Rayleigh number $Ra_T=\frac{g\beta_{Tf}L^3(T_h-T_c)}{\nu_f^2}$, solutal Rayleigh number $Ra_c=\frac{g\beta_{cf}L^3(C_h-C_c)}{\nu_f^2}$, Dufour coefficient $D_f=\left(\frac{D}{\nu}\right)_f\frac{k_{Tf}(C_h-C_c)}{C_sC_p(T_h-T_c)}$ and Soret coefficient $S_r=\left(\frac{D}{\nu}\right)_f\frac{k_{Tf}(T_h-T_c)}{T_m(C_h-C_c)}$ are used.

The average Nusselt and Sherwood numbers at the heated and concentrated surfaces of the enclosure may be expressed, respectively as

$$Nu=-\frac{1}{L_s}\int_0^{L_s}\frac{\partial\theta}{\partial Y}dX \quad \text{and} \quad Sh=-\int_0^1\frac{\partial C}{\partial Y}dX\ .$$

4. Numerical Implementation

The Galerkin finite element method is used to solve the non-dimensional governing equations along with boundary

conditions for the considered problem. The equation of continuity has been used as a constraint due to mass conservation and this restriction may be used to find the pressure distribution. The penalty finite element method [21] is used to solve the Eqs. (2) - (4), where the pressure P is eliminated by a penalty constraint. The continuity equation is automatically fulfilled for large values of this penalty constraint. Then the velocity components (U, V), temperature (θ) and concentration (C) are expanded using a basis set. The Galerkin finite element technique yields the subsequent nonlinear residual equations. Three points Gaussian quadrature is used to evaluate the integrals in these equations. The non-linear residual equations are solved using Newton–Raphson method to determine the coefficients of the expansions. The convergence of solutions is assumed when the relative error for each variable between consecutive iterations is recorded below the convergence criterion ε such that $\left|\psi^{n+1}-\psi^{n}\right| \le 10^{-4}$, where n is the number of iteration and Ψ is a function of U, V, θ and C.

4.1. Grid Independent Test

An extensive mesh testing procedure is conducted to guarantee a grid-independent solution for $Ra = 10^4$, $Pr = 6.2$, $D_f = S_r = 0.5$, $Sc = 5$, $\phi = 5\%$ in the chamber. In the present work, we examine five different non-uniform grid systems with the following number of elements within the resolution field: 2569, 4730, 6516, 8457 and 10426. The numerical scheme is carried out for highly precise key in the average Nusselt (Nu) and Sherwood (Sh) numbers for the aforesaid elements to develop an understanding of the grid fineness as shown in Fig. 2. The scale of the average Nusselt and Sherwood numbers for 8457 elements shows a little difference with the results obtained for the other elements. Hence, considering the non-uniform grid system of 8457 elements is preferred for the computation.

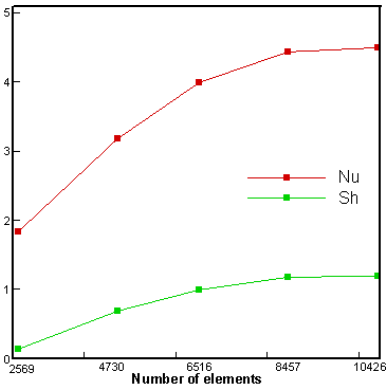

Fig. 2: Grid test for the geometry

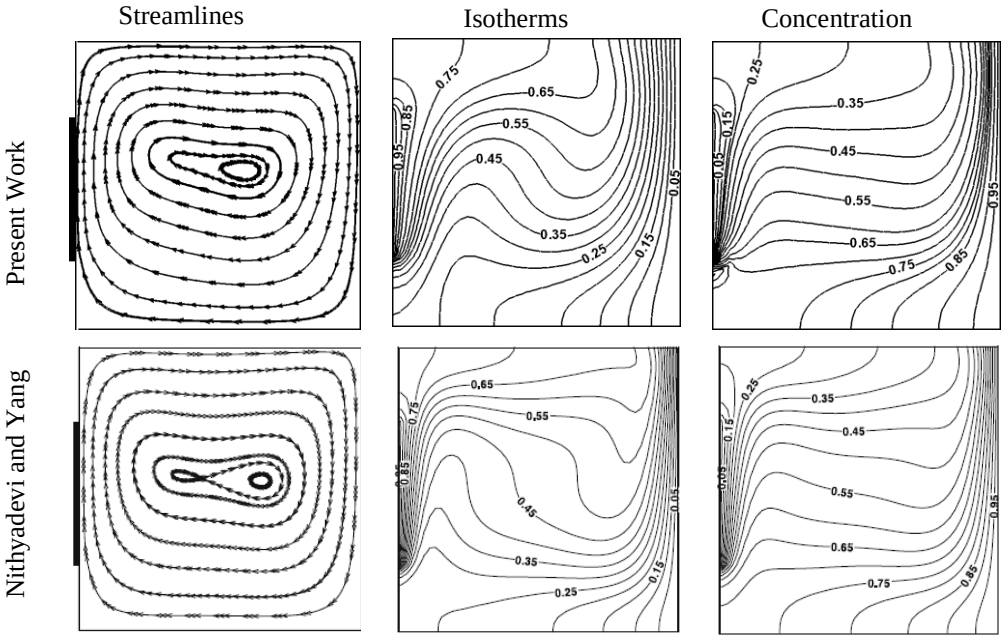

Fig. 3: Comparison between present work and Nithyadevi and Yang using $Pr = 11.573$, $D_f = S_r = 0.5$, $Sc = 5$ and $Ra_T = 10^5$

4.2. Code Validation

The present numerical solution is validated by comparing the current code results for streamlines, isotherms and concentration profiles using $D_f = S_r = 0.5$, $Sc = 5$, $Pr = 11.573$ and $Ra_T = 10^5$ with the graphical representation of Nithyadevi and Yang [2] which was reported for double diffusive natural convection in a partially heated enclosure with Soret and Dufour effects. Fig. 3 demonstrates the above stated comparison. As shown in Fig. 3, the numerical solutions (present work and Nithyadevi and Yang [2]) are in good agreement.

5. Results and Discussion

In this section, numerical results of streamlines and isotherms for various values of Soret (S_r) and Dufour (D_r) coefficients and with Al_2O_3/water nanofluid in a square enclosure are displayed. $Ra = Ra_T = Ra_c$ is assumed for the present numerical calculation. The considered values of D_f and S_r are $D_f = S_r$ = (0, 0.5 and 1). But the Prandtl number Pr = 6.2, the Rayleigh number $Ra = 10^4$, the Schmidt number Sc= 5 and solid volume fraction of the nanofluid ϕ = 5% are kept fixed for this study. In addition, the values of the average Nusselt and Sherwood numbers, mean temperature and concentration as well as horizontal and vertical velocities at the middle of the cavity have been calculated for different mentioned parameters.

Fig. 4 (a) - (c) exposes the effect of S_r on the flow, thermal and concentration fields while $D_f = 0.5$ and $Sc = 5$. At the absence of the Soret coefficient (S_r) a primary anticlockwise circulating cell occupies the bulk of the chamber. The size of the inner vortex of this cell becomes larger with the increasing of the Soret coefficient. In addition for the largest value of S_r, the streamlines form rectangular pattern whereas initially they are circular. As well as another vortex is appeared near the left wall of the chamber. The isotherms and iso-concentrations are crowded around the active location on the bottom surface of the enclosure for (S_r = 1). In addition, the temperature lines corresponding to S_r = 1 become less bended. Decreasing Soret effect leads to deformation of the thermal and concentration boundary layers at the right part of the cold upper wall and middle of the bottom surface.

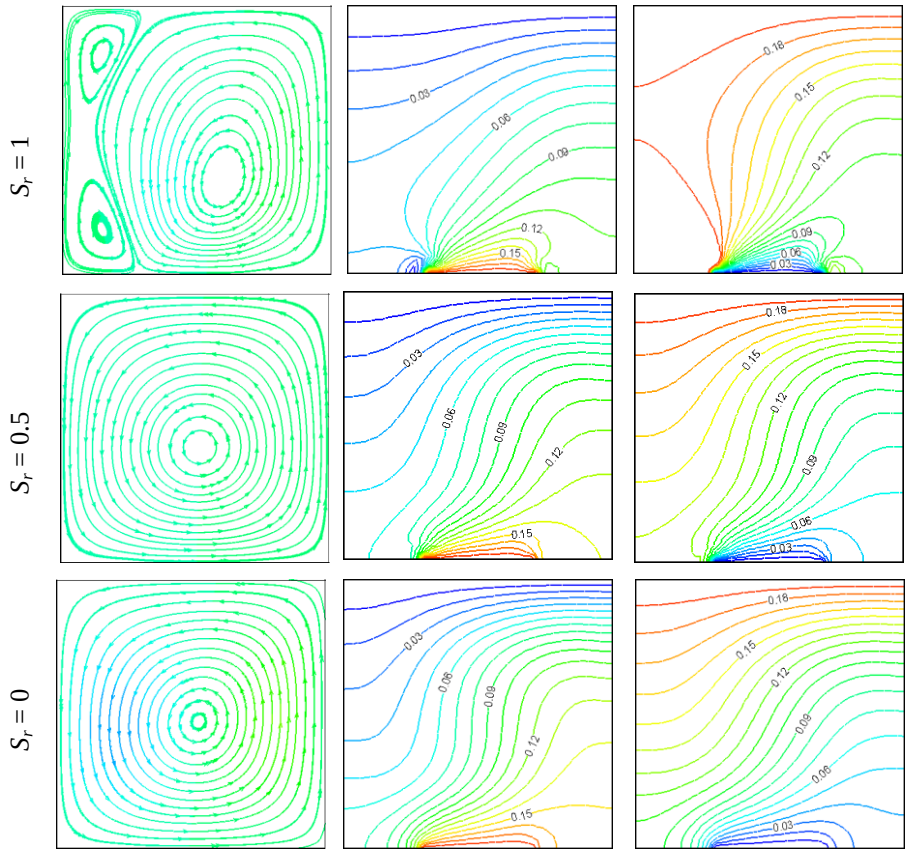

(a) (b) (c)

Fig. 4: Effect of S_r on (a) streamlines, (b) Isotherms and (c) Concentration at $D_f = 0.5$ and $Sc = 5$

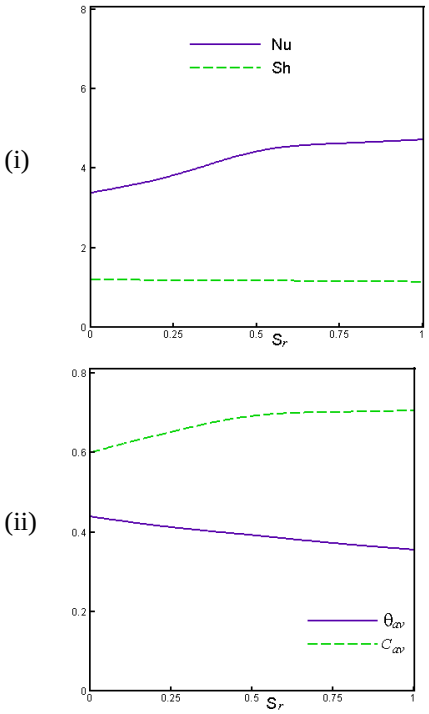

Fig. 5: Effect of S_r on (i) *Nu* and *Sh* and (ii) θ_{av} and C_{av} at D_f = 0.5 and *Sc* = 5

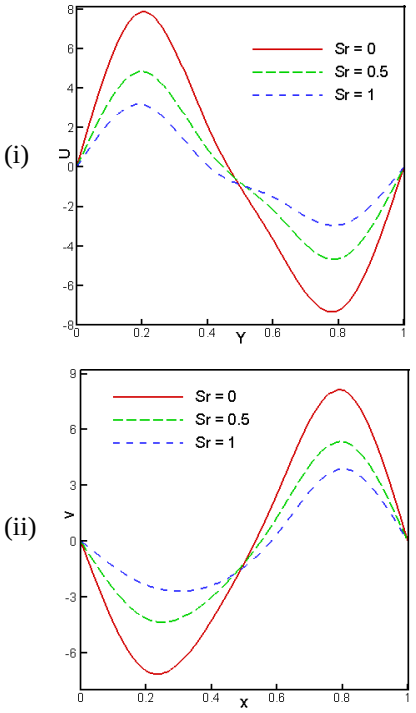

Fig. 6: Mid height (i) horizontal and (ii) vertical velocities for different S_r with D_f = 0.5 and *Sc* = 5

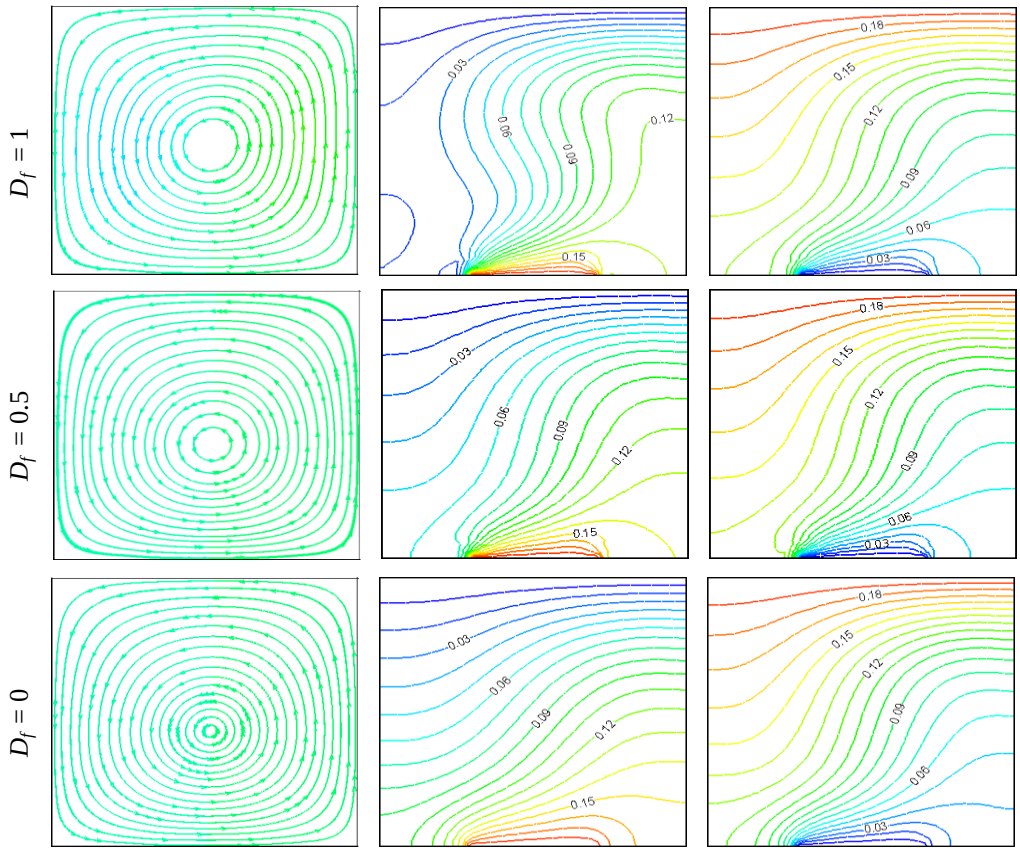

(a) (b) (c)

Fig. 7: Effect of D_f on (a) streamlines, (b) Isotherms and (c) Concentration at S_r = 0.5 and *Sc* = 5

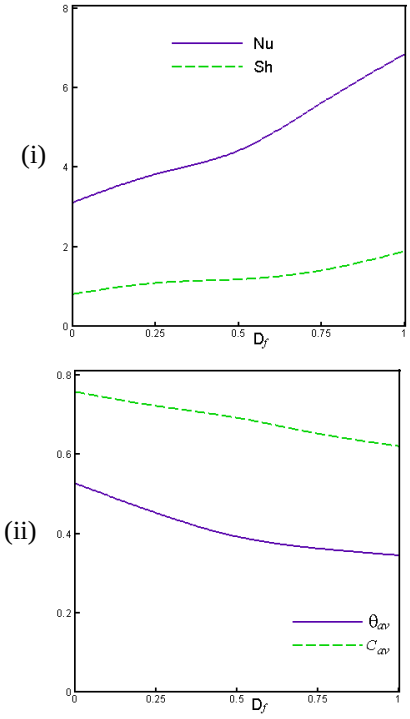

Fig. 8: Effect of D_f on (i) *Nu* and *Sh* and (ii) θ_{av} and C_{av} at $S_r = 0.5$ and $Sc = 5$

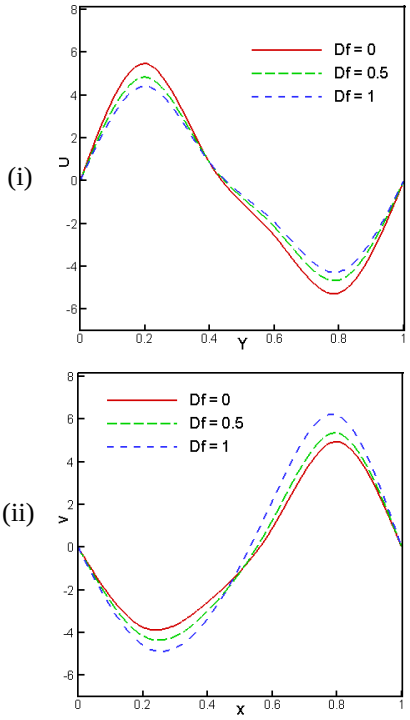

Fig. 9: Mid height (i) horizontal and (ii) vertical velocities for different D_f at $S_r = 0.5$ and $Sc = 5$

The average Nusselt (*Nu*) and Sherwood (*Sh*) numbers, average temperature (θ_{av}) and concentration (C_{av}) along with the Soret coefficient (S_r) are depicted in Fig. 5(i)-(ii). It is seen from Fig. 5(i) that *Nu* enhances gradually whereas *Sh* remains almost invariant for mounting S_r. Consequently Fig. 5(ii) shows that (θ_{av}) devalues and (C_{av}) rises sequentially for all values of Soret coefficient S_r.

Fig. 6(i)-(ii) shows the mid-height horizontal and vertical velocity profiles inside the chamber for different S_r effect. It is observed that the fluid particle moves with greater velocity for the absence of Soret coefficient S_r. The waviness devalues for higher values of S_r.

The effect of D_f on the flow, thermal and concentration fields is presented in Fig. 7 (a) - (c) while $S_r = 0.5$ and $Sc = 5$. A primary anticlockwise recirculation cell occupying the whole cavity is found for the absence of the Dufour coefficient (D_f). The fluid rises along the right wall and falls along the left wall. The size of the inner vortex of this cell becomes larger with the increasing of the Dufour coefficient. The strength of the flow circulation, the thermal current and concentration activities are much more activated with escalating D_f. Increasing D_f, the temperature and concentration lines at the middle part of the enclosure become vertical whereas initially they are almost horizontal. Due to rising values of D_f, the temperature and concentration distributions become distorted resulting in an increase in the overall heat and mass transfer. It is worth noting that as the Dufour coefficient increases, the thickness of the thermal boundary layer near the horizontal surfaces rises which indicates a steep temperature and concentration gradients. Hence, an increase in the overall heat and mass transfer within the cavity is observed.

Fig. 8(i)-(ii) displays the mean Nusselt and Sherwood numbers, average temperature (θ_{av}) and concentration (C_{av}) for the effect of Dufour coefficient D_f. Both *Nu* and *Sh* grow up for varying D_f. The rate of heat transfer is found to be more effective than the mass transfer rate. On the other hand, θ_{av} and C_{av} has notable changes with different values of D_f. The value of mean concentration is always higher than that of average temperature at a particular value of Dufour coefficient.

The *U* and *V* velocities at the middle of the cavity for various D_f are depicted in Fig. 9 (i)-(ii). A small variation in velocity is found due to changing D_f. Some perturbations are seen in the horizontal velocity graph for $D_f = 0$ and in the vertical velocity profile for $D_f = 1$.

6. Conclusion

The influence of nanoparticles on natural convection boundary layer flow inside a square cavity with water-Al_2O_3 nanofluid is accounted. Various Soret-Dufour coefficients and Schmidt number have been considered for the flow, temperature and concentration fields as well as the heat and mass transfer rate, horizontal and vertical velocities at the

middle height of the enclosure while *Pr*, *Ra* and ϕ are fixed at 6.2, 10^4 and 5% respectively. The results of the numerical analysis lead to the following conclusions:

- The structure of the fluid streamlines, isotherms and iso-concentrations within the chamber is found to significantly depend upon the Soret-Dufour coefficients..
- The Al_2O_3 nanoparticles with the highest S_r and D_f is established to be most effective in enhancing performance of heat transfer rate than the rate of mass transfer.
- Greater variation is observed in velocities at a particular point for the changes of S_r with compared to that of D_f.
- Average concentration is higher than average temperature inside the chamber for the pertinent parameters.

Overall the analysis also defines the operating range where water-Al_2O_3 nanofluid can be considered effectively in determining the level of heat and mass transfer augmentation.

Acknowledgements

The present work is fully supported by the department of Mathematics, Bangladesh University of Engineering & Technology.

References

[1] Nithyadevi, N., Yang, R.J., 2009. Double diffusive natural convection in a partially heated enclosure with Soret and Dufour effects, International Journal of Heat and Fluid Flow 30, p. 902.
[2] Sivasankaran, S., Kandaswamy, P., 2006. Double diffusive convection of water in a rectangular partitioned enclosure with temperature dependent species diffusivity, International Journal of Fluid Mechanics Research 33, p. 345.
[3] Sivasankaran, S., Kandaswamy, P., 2007. Double diffusive convection of water in a rectangular partitioned enclosure with concentration dependent species diffusivity, Journal of the Korean Society for Industrial and Applied Mathematics 11, p. 71.
[4] Mansour, A., Amahmid, A., Hasnaoui, M., Bourich, M., 2006. Multiplicity of solutions induced by thermosolutal convection in a square porous cavity heated from below and submitted to horizontal concentration gradient in the presence of Soret effect, Numerical Heat Transfer Part A: Applications 49, p. 69.
[5] Platten, J.K., 2006. The Soret effect: a review of recent experimental results, Journal of Applied Mechanics 73, p. 5.
[6] Patha, M.K., Murthy, P.V.S.N., Raja Sekhar, G.P., 2006. Soret and Dufour effects in a non-darcy porous medium. Journal of Heat Transfer 128, p. 605.
[7] Oztop, H.F., 2007. Natural convection in partially cooled and inclined porous rectangular enclosures. International Journal of Thermal Sciences 46, p. 149.
[8] Erbay, B., Altac, Z., Sulus, B., 2004. Entropy generation in a square enclosure with partial heating from a vertical lateral wall, Heat and Mass Transfer 40, p. 909.
[9] Nithyadevi, N., Kandaswamy, P., Lee, J., 2007. Natural convection in a rectangular cavity with partially active side walls. International Journal of Heat and Mass Transfer 50, p. 4688.
[10] Kandaswamy, P., Sivasankaran, S., Nithyadevi, N., 2007. Buoyancy-driven convection of water near its density maximum with partially active vertical walls. International Journal of Heat and Mass Transfer 50, p. 942.
[11] Oztop, H.F. Abu-Nada, E., 2008. Numerical study of natural convection in partially heated rectangular enclosures filled with nanofluids, International Journal of Heat and Fluid Flow 29, p. 1326.
[12] Rouboa, A.,Silva, A., Freire, A.J., Borges, A., Ribeiro, J., Silva, P., Alexandre, J.L., 2008. "Numerical analysis of convective heat transfer in nanofluid", AIP Conference Proceedings, pp. 819–822.
[13] Javad Abolfazli Esfahani and Vahid Bordbar, 2011. Double Diffusive Natural Convection Heat Transfer Enhancement in a Square Enclosure Using Nanofluids, Journal of Nanotechnology in Engineering and Medicine 2(2), p. 021002.
[14] Rama Subba Reddy Gorla, Ali Jawad Chamkha, Ahmed Mohamed Rashad, 2011. Mixed convective boundary layer flow over a vertical wedge embedded in a porous medium saturated with a nanofluid: Natural Convection Dominated Regime, Nanoscale Research Letters 6, p 207.
[15] Kuznetsov, A.V. , Nield, D.A. , 2011. Double-diffusive natural convective boundary-layer flow of a nanofluid past a vertical plate, International Journal of Thermal Sciences 50, p. 712.
[16] Pal, D., Mondal, H., 2011. Effects of SoretDufour, chemical reaction and thermal radiation on MHD non-Darcy unsteady mixed convective heat and mass transfer over a stretching sheet, Communications in Nonlinear Science and Numerical Simulation 16, p. 1942.
[17] Kuang C. Lin, Angela Violi, 2010. Natural convection heat transfer of nanofluids in a vertical cavity: Effects of non-uniform particle diameter and temperature on thermal conductivity, International Journal of Heat and Fluid Flow 31, p. 236.
[18] Saleh, H., Roslan, R., Hashim, I., 2011. Natural convection heat transfer in a nanofluid-filled trapezoidal enclosure, International Journal of Heat and Mass Transfer 54, p. 194.
[19] Brinkman, H.C. 1952. The viscosity of concentrated suspensions and solution, Journal of Chemical Physics 20, p. 571.
[20] Maxwell-Garnett, J.C., 1904. Colours in metal glasses and in metallic films, Philosophical Transactions of the Royal Society of London A 203, p. 385.
[21] Basak, T., Roy, S., Pop, I., 2009. Heat flow analysis for natural convection within trapezoidal enclosures based on heat line concept, International Journal of Heat and Mass Transfer 52, p. 2471.

Available online at www.sciencedirect.com

SciVerse ScienceDirect

Procedia Engineering 00 (2012) 000–000

Procedia Engineering

www.elsevier.com/locate/procedia

5th BSME International Conference on Thermal Engineering

Numerical Prediction of Unsteady Heat and Fluid Flow through a Curved Rectangular Duct of Large Aspect Ratio

Rabindra Nath Mondal[a]* and Md. Saidul Islam[b]

[a] *Department. of Mathematics, Faculty of Science, Jagannath University, Dhaka-1100, Bangladesh*
[b] *Mathematics Discipline; Science, Engineering and Technology School, Khulna University, Khulna-9208, Bangladesh*
Email: rnmondal71@yahoo.com

Abstract

In this paper, a comprehensive numerical study is presented for the fully developed two-dimensional flow of viscous incompressible fluid through a curved rectangular duct of aspect ratio 3. Unsteady solutions are obtained by using a spectral method and covering a wide range of Dean number $100 \le Dn \le 1000$ and the Grashof number $100 \le Gr \le 2000$. The outer wall of the duct is heated while the inner wall is cooled. The main concern of this study is to find out the unsteady flow behavior *i.e* whether the unsteady flow is steady-state, periodic, multi-periodic or chaotic, if the Dean number or the Grashof number is increased. It is found that the unsteady flow is a steady-state solution for Dn = 100 at $Gr = 100$ and $Gr = 2000$ but periodic at $Gr = 500, 1000, 1500$. If the Dean number is increased, the unsteady flow becomes chaotic for any value of Gr in the range. Contours of secondary flow patterns and temperature profiles are also obtained, and it is found that the unsteady flow consists of a two-, four-, six- and eight-vortex solutions. It is also found that the chaotic flow enhances heat transfer more significantly than the steady-state or periodic solutions, if the Dean number is increased.

Keywords: Curved rectangular duct, secondary flow, chaotic solution, Dean number, aspect ratio.

Nomenclature

Dn	: Dean number	T	: Temperature
g	: Gravitational acceleration	u	: Velocity components in the $x-$direction
Gr	: Grashof number	v	: Velocity components in the $y-$direction
h	: Half height of the cross section	w	: Velocity components in the $z-$direction
d	: Half width of the cross section	x	: Horizontal axis
L	: Radius of the curvature	y	: Vertical axis
P_r	: Prandtl number	z	: Axis in the direction of the main flow
t	: Time	λ	: Resistance coefficient

Greek letters

δ	: Curvature of the duct	υ	: Kinematic viscosity
ρ	: Density	κ	: Thermal diffusivity
ψ	: Sectional stream function	μ	: Viscosity

* Corresponding author. Tel.: +88-01710851580; Fax: +88-02-7113752.
E-mail address: rnmondal71@yahoo.com

1. Introduction

The study of flows and heat transfer through curved ducts and channels has been and continues to be an area of paramount interest of many researchers because of the diversity of their practical applications in fluids engineering, such as in fluid transportation, turbo machinery, refrigeration, air conditioning systems, heat exchangers, ventilators, centrifugal pumps and blade-to-blade passage for cooling system in modern gas turbines. Blood flow in the human and other animals also represents an important application of this subject because of the curvature of many blood vessels, particularly the aorta. Dean [1] first formulated the problem in mathematical terms under the fully developed flow conditions and showed the existence of a pair of counter rotating vortices in a curved pipe. In consideration of the importance, flows in curved ducts have been studied extensively in the literature for several decades, the readers are referred to Berger *et al*. [2], Nandakumar and Masliyah [3] and Yanase *et al.*[4] for some outstanding reviews on curved duct flows.

Considering the non-linear nature of the Navier-Stokes equation, the existence of multiple solutions does not come as a surprise. The solution structure of fully developed flow is commonly present in a bifurcation diagram which consists of a number of lines (branches) connecting different possible solutions. These branches can bifurcate and show multiple solutions in limit points (Mondal, [5]). An early complete bifurcation study of two-dimensional (2-D) flow through a curved duct of square cross section was conducted by Winters [6]. Very recently, Mondal *et al*. [7] performed comprehensive numerical study on fully developed bifurcation structure and stability of two-dimensional (2D) flow through a curved duct with square cross section and found a close relationship between the unsteady solutions and the bifurcation diagram of steady solutions. The flow through a curved duct with differentially heated vertical sidewalls has another aspect because secondary flows promote fluid mixing and heat transfer in the fluid (Yanase *et al*., [8]). Recently, Mondal *et al*. ([9], [10]) performed numerical investigations of non-isothermal flows through a curved duct with rectangular cross section, where they studied the flow characteristics with the effects of secondary flows on convective heat transfer.

In the present paper, a comprehensive numerical study is presented for the fully developed two-dimensional flow of viscous incompressible fluid flow through a curved rectangular duct of large aspect ratio. Flow characteristics are studied by using a spectral method and covering a wide range of the Dean number and the Grashof number.

2. Governing Equations

Consider an incompressible viscous fluid streaming through a curved duct with rectangular cross section whose width and height are 2*d* and 2*h*, respectively. The coordinate system with the relevant notations are shown in Fig. 1. It is assumed that the outer wall of the duct is heated while the inner one is cooled. The temperature of the outer wall is $T_0 + \Delta T$ and that of the inner wall is $T_0 - \Delta T$, where $\Delta T > 0$. The x, y, and z axes are taken to be in the horizontal, vertical, and axial directions, respectively. It is assumed that the flow is uniform in the axial direction, and that it is driven by a constant pressure gradient G along the center-line of the duct, i.e. the main flow in the axial direction as shown in Fig. 1.The variables are non-dimensionalized by using the representative length d and the representative velocity $U_0 = \nu/d$ .We introduce the non-dimensional variables defined as

$$u = \frac{u'}{U_0}, \qquad v = \frac{v'}{U_0}, \quad w = \frac{\sqrt{2\delta}}{U_0} w', \quad x = \frac{x'}{d}, \quad \bar{y} = \frac{y'}{d}, \quad z = \frac{z'}{d}$$

$$T = \frac{T'}{\Delta T}, \quad t = \frac{U_0}{d} t', \quad \delta = \frac{d}{L}, \quad P = \frac{P'}{\rho U_0^2}, G = \frac{\partial P^{'}}{\partial z^{'}} \frac{d}{\rho {U_O}^2}$$

where u, v, and w are the non-dimensional velocity components in the x, y, and z directions, respectively; t is the non-dimensional time, P the non-dimensional pressure, δ the non-dimensional curvature, and temperature is non-dimensionalized by ΔT. Henceforth, all the variables are nondimensionalized if not specified.

The sectional stream function ψ is introduced as

$$u = \frac{1}{1+\delta x} \frac{\partial \psi}{\partial \bar{y}}, v = -\frac{1}{1+\delta x} \frac{\partial \psi}{\partial x}. \tag{1}$$

A new coordinate variable y' is introduced in the y direction as $y = ly'$, where $l = h/d$ is the aspect ratio of the duct cross section. From now on y denotes y' for the sake of simplicity. Then the basic equations for w, ψ and T are derived from the Navier-Stokes equations and the energy equation under the *Boussinesq approximation* as,

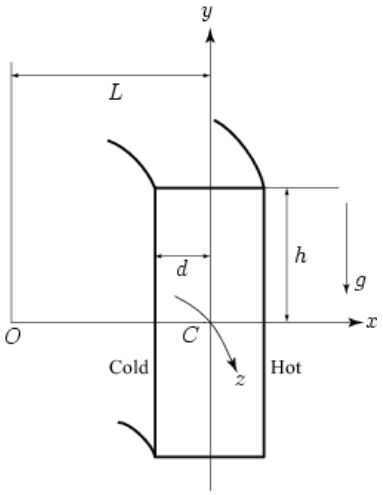

Fig. 1. Coordinate system of the curved rectangular duct

$$(1+\delta x)\frac{\partial w}{\partial t}+\frac{1}{l}\frac{\partial(w,\psi)}{\partial(x,y)}-D_n+\frac{\delta^2 w}{1+\delta x}=(1+\delta x)\Delta_2 w-\frac{\delta}{l(1+\delta x)}\frac{\partial\psi}{\partial y}w+\delta\frac{\partial w}{\partial x} \tag{2}$$

$$\left(\Delta_2-\frac{\delta}{1+\delta x}\frac{\partial}{\partial x}\right)\frac{\partial\psi}{\partial t}=-\frac{1}{l(1+\delta x)}\frac{\partial(\Delta_2\psi,\psi)}{\partial(x,y)}+\frac{\delta}{l\left(1+\delta x\right)^2}\times\left[\frac{\partial\psi}{\partial y}\left(2\Delta_2\psi-\frac{3\delta}{1+\delta x}\frac{\partial\psi}{\partial x}+\frac{\partial^2\psi}{\partial x^2}\right)-\frac{\partial\psi}{\partial x}\frac{\partial^2\psi}{\partial x\partial y}\right]+\frac{\delta}{\left(1+\delta x\right)^2}$$
$$\times\left[3\delta\frac{\delta^2\psi}{\partial x^2}-\frac{3\delta^2}{1+\delta x}\frac{\partial\psi}{\partial x}\right]-\frac{2\delta}{1+\delta x}\frac{\partial}{\partial x}\Delta_2\psi+\frac{1}{l}w\frac{\partial w}{\partial y}\times\Delta_2^2\psi-Gr(1+\delta x)\frac{\partial T}{\partial x}, \tag{3}$$

$$\frac{\partial T}{\partial t}+\frac{1}{l(1+\delta x)}\frac{\partial(T,\psi)}{\partial(x,y)}=\frac{1}{\mathrm{Pr}}\left(\Delta_2 T+\frac{\delta}{1+\delta x}\frac{\partial T}{\partial x}\right). \tag{4}$$

where

$$\Delta_2\equiv\frac{\partial^2}{\partial x^2}+\frac{1}{l^2}\frac{\partial^2}{\partial y^2},\quad \frac{\partial(f,g)}{\partial(x,y)}\equiv\frac{\partial f}{\partial x}\frac{\partial g}{\partial y}-\frac{\partial f}{\partial y}\frac{\partial g}{\partial x}. \tag{5}$$

The Dean number D_n, the Grashof number G_r, and the Prandtl number P_r, which appear in Eqs. (2) to (4) are defined as

$$D_n=\frac{Gd^3}{\mu\nu}\sqrt{\frac{2d}{L}},\quad G_r=\frac{\beta g\Delta T d^3}{\nu^2},\quad P_r=\frac{\nu}{k} \tag{6}$$

where μ,ν,k and g are the viscosity, the coefficient of thermal expansion, the coefficient of thermal diffusivity and the gravitational acceleration respectively.

The rigid boundary conditions for w and ψ are used as

$$w(\pm1,y)=w(x,\pm1)=\psi(\pm1,y)=\psi(x,\pm1)=\frac{\partial\psi}{\partial x}(\pm1,y)=\frac{\partial\psi}{\partial y}(x,\pm1)=0 \tag{7}$$

and the temperature T is assumed to be constant on the walls as

$$T(1,y)=1,\ T(-1,y)=-1,\ T(x,\pm1)=x. \tag{8}$$

The upper and lower walls are adiabatic. In the present study, *Dn* and *Gr* are varied while δ and *Pr* are fixed as δ = 0.1 and *Pr* = 7.0 (water).

3. Method of numerical calculation

In order to obtain the numerical solutions, spectral method is used. The main objective of the method is to use the expansion of the polynomial functions that is the variables are expanded in the series of functions consisting of Chebyshev polynomials. The expansion function $\phi_n(x)$ and $\psi_n(x)$ are expressed as

$$\Phi_n(x)=\left(1-x^2\right)C_n(x),\ \Psi_n(x)=\left(1-x^2\right)^2C_n(x), \tag{9}$$

where $C_n(x) = \cos(n\cos^{-1}(x))$ is the n^{th} order Chebyshev polynomial. $w(x,y,z)$, $\psi(x,y,t)$ and $T(x,y,t)$ are expanded in terms of $\Phi_n(x)$ and $\Psi_n(x)$ as

$$\left.\begin{aligned} w(x,y,z) &= \sum_{m=0}^{M}\sum_{n=0}^{N} w_{mn}(t)\Phi_m(x)\Phi_n(y), \\ \psi(x,y,t) &= \sum_{m=0}^{M}\sum_{n=0}^{N} \psi_{mn}(t)\Psi_m(x)\Psi_n(y), \\ T(x,y,t) &= \sum_{m=0}^{M}\sum_{n=0}^{N} T_{mn}(t)\Phi_m(x)\Phi_n(y) + x, \end{aligned}\right\} \tag{10}$$

where M and N are the truncation numbers in the x and y directions respectively. The expansion coefficients w_{mn}, ψ_{mn} and T_{mn} are then substituted into the basic Eqs. (2), (3) and (4) and the collocation method is applied. As a result, the nonlinear algebraic equations for w_{mn}, ψ_{mn} and T_{mn} are obtained. The collocation points are taken to be

$$\left.\begin{aligned} x_i &= \cos\left[\pi\left(1-\frac{i}{M+2}\right)\right], \quad i = 1,\ldots,M+1, \\ y_i &= \cos\left[\pi\left(1-\frac{i}{N+2}\right)\right], \quad j = 1,\ldots,N+1. \end{aligned}\right\} \tag{11}$$

where $i = 1,\ldots,M+1$ and $j = 1,\ldots,N+1$. In the present study, numerical calculations are carried out for $100 \le Dn \le 1000$ over a wide range of the Grashof number $100 \le Gr \le 2000$ for the rectangular duct of aspect ratio $l = 3$. For sufficient accuracy of the solutions, we used M = 16 and N = 48. Steady solutions are obtained by the Newton-Raphson iteration method. Finally, to calculate the unsteady solutions, Crank-Nicolson and Adams-Bashforth methods together with the function expansion and collocation methods are applied to the equations (2) to (4).

4. Resistance coefficient

We use the resistance coefficient λ as one of the representative quantities of the flow state. It is also called the *hydraulic resistance coefficient*, and is generally used in fluids engineering, defined as

$$\frac{P_1^* - P_2^*}{\Delta z^*} = \frac{\lambda}{dh^*}\frac{1}{2}\rho\left\langle w^* \right\rangle^2, \tag{12}$$

where quantities with an asterisk denote the dimensional ones, $\langle\rangle$ stands for the mean over the cross section of the rectangular duct, and $d_h^* = 4(2d \times 4dh)/(4d \times 8dh)$. Since $\left(P_1^* - P_2^*\right)/\Delta z^* = G$, λ is related to the mean non-dimensional axial velocity $\langle w \rangle$ as

$$\lambda = \frac{16\sqrt{2\delta}\,Dn}{3\langle w \rangle^2}, \tag{13}$$

where $\langle w \rangle = \sqrt{2\delta}\,d / v\left\langle w^* \right\rangle$. . In this paper, λ is used to find the unsteady solutions by numerical computations.

5. Results and Discussion

In this study, we have investigated time evolution of the resistance coefficient λ for the fluid flows through a curved rectangular duct of curvature $\delta = 0.1$ and aspect ratio $l = 3$ over a wide range of the Grashof number and the Dean number. In addition to the time evolution of λ, the secondary flow patterns and temperature profiles at various Dean numbers are also discussed.

5.1 Time evolution of the unsteady solutions

We performed time evolution of λ for Dn = 100 and Gr = 100, 500, 1000, 1500 and 2000 as shown in Fig. 2(a), and we see that the unsteady flow is a steady-state solution for Dn = 100 and Gr =100 and 1000 but periodic for rest of the cases. Figure 2(b) shows, for example, time evolution of λ for Dn = 100 and Gr = 1500 and we see that the flow is a periodic solution, which is well justified by drawing a phase space as shown in Fig. 2(c). In Fig. 2(c) we see that only a single orbit is

created for the time-periodic solution at *Dn* = 100 and *Gr* = 1500. To observe the periodic change of the flow evolution, we obtained typical contours of secondary flow patterns and temperature profiles for *Dn*=100 and *Gr*=1500 as shown in Fig. 2(d), where we see that the unsteady flow oscillates between asymmetric two-vortex solution, one is a large vortex dominating the smaller one. Then we performed time evolution of λ for *Dn* = 500 and *Gr* = 100, 500, 1000, 1500 and 2000 as shown in Fig. 3(a), and we see that the unsteady flow is a chaotic solution for all the cases except at *Dn* = 500 and *Gr* = 1000. At *Gr* =1000 we found that the unsteady flow is a periodic solution. Figure 3(b) shows unsteady solution for Dn = 500 and *Gr* = 100, which shows that the flow oscillates irregularly that is the flow is chaotic at *Dn* = 500 and *Gr* = 100. A phase space of the time change of λ at *Dn* = 500 and *Gr* = 100 is also shown in Fig. 3(c), where chaotic orbit is seen. Then in order to observe the chaotic flow behavior, we obtained typical contours of secondary flow patterns and temperature profiles for *Dn*=500 and *Gr*=100 as shown in Fig. 3(d). As seen in Fig. 3(d), the unsteady flow at *Dn*=500 and *Gr*=100 oscillates between asymmetric four- and six-vortex solutions. Then we perform time evolution of λ for the unsteady solution at Dn = 500 and *Gr* = 1000 as shown in Fig. 4(a). Figure 4(a) shows that the flow may be periodic or multi-periodic. However, to be sure, we draw the phase space of the time change of λ for *Dn* = 500 and *Gr* = 1000 as shown in Fig. 4(b), and it is found that the orbit is neither periodic nor chaotic. Thus the flow is *transitional chaos* (for details, see Mondal [7]). Then in order to observe the transitional chaotic flow behavior, we obtained typical contours of secondary flow patterns and temperature profiles for *Dn*=500 and *Gr*=1000 as shown in Fig. 4(c). It is found that the unsteady flow at *Dn*=500 and *Gr*=1000 oscillates between asymmetric four- and six-vortex solutions.

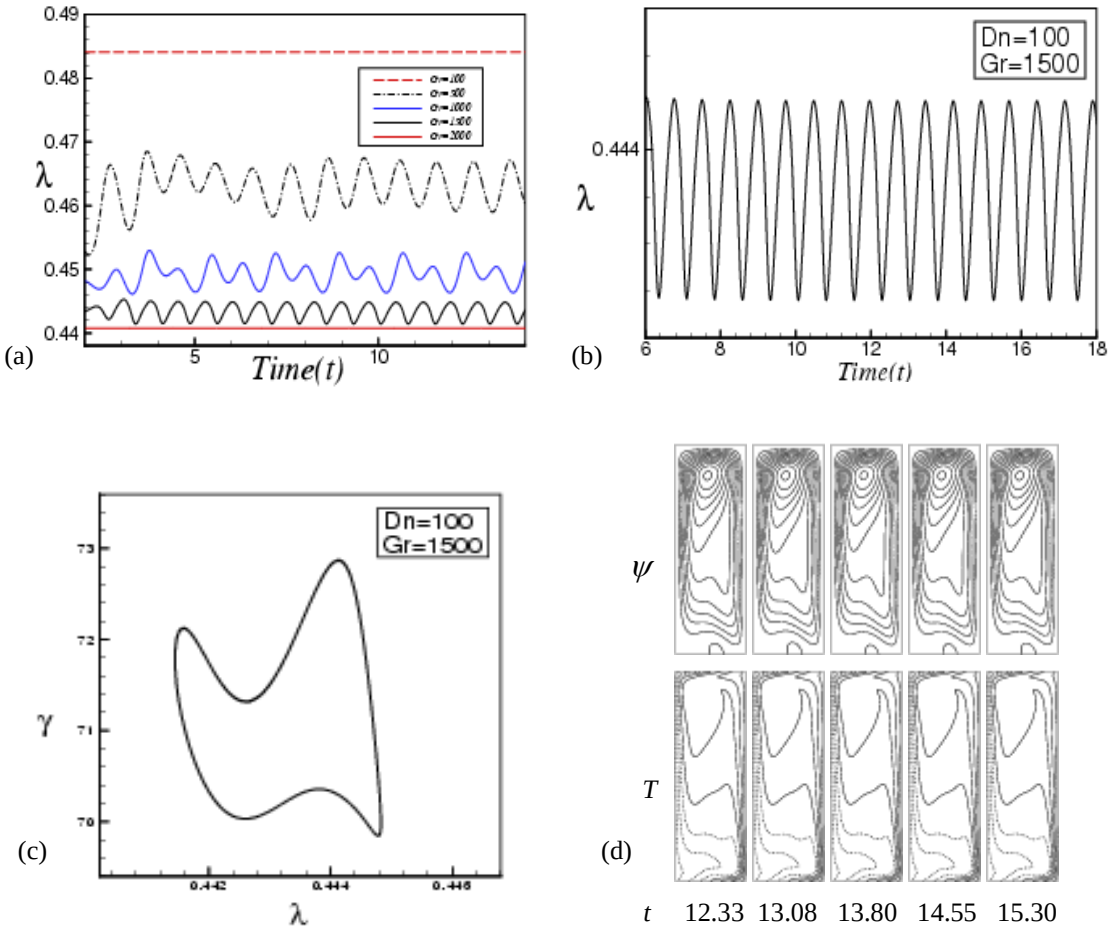

Fig. 2. (a) Time evolution of λ for *Dn* = 100 and Gr = 100, 500, 1000, 1500 and 2000, (b) Time evolution of λ for *Dn* = 100 and *Gr* = 1500 (c) Phase space of the time evolution for *Dn* = 100 and *Gr* =1500 (d) Contours of Secondary flow patterns (top) and Temperature profiles (bottom) for *Dn* =100 and *Gr* =1500.

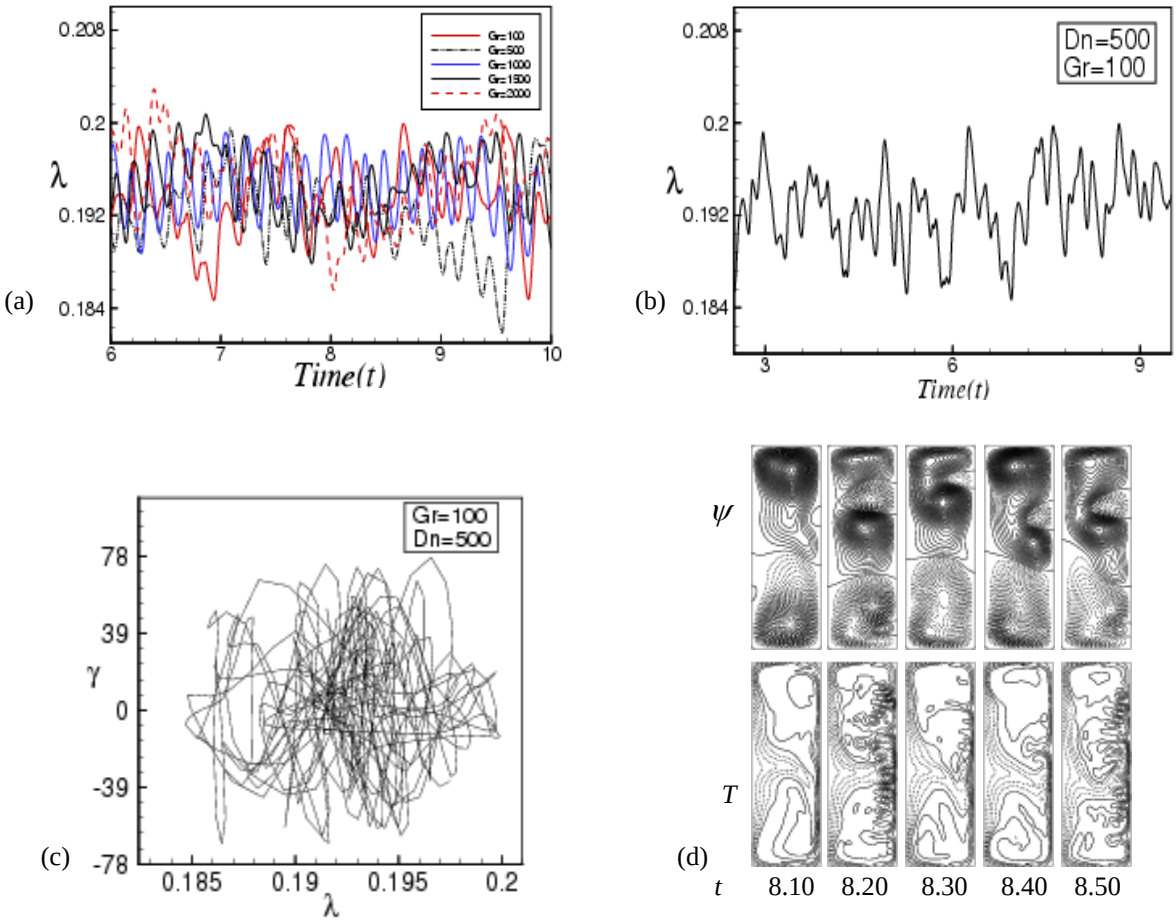

Fig. 3. (a) Time evolution of λ for *Dn* = 500 and *Gr* = 100, 500, 1000, 1500 and 2000, (b) Time evolution of λ for *Dn* = 500 and *Gr* = 100 (c) Phase space of the time evolution for *Dn*=500 and *Gr* =100 (d) Contours of secondary flow patterns (top) and Temperature profiles (bottom) for *Dn* =500 and *Gr* =100.

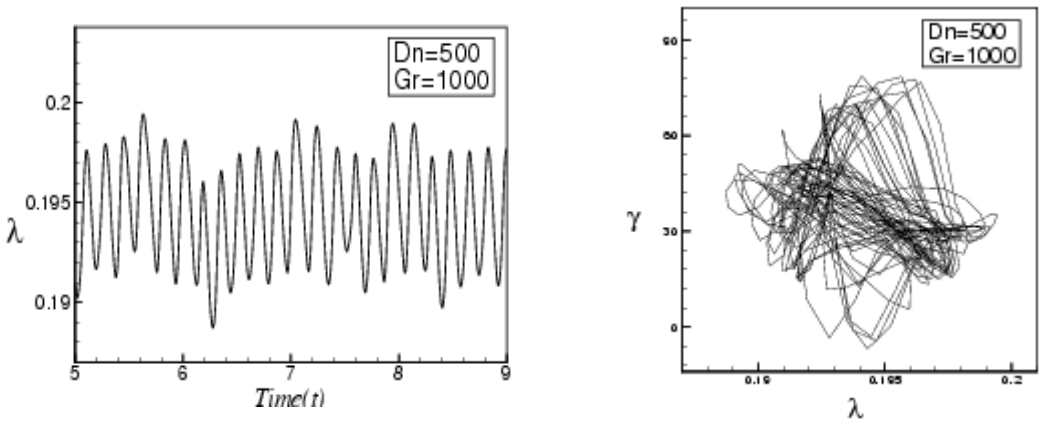

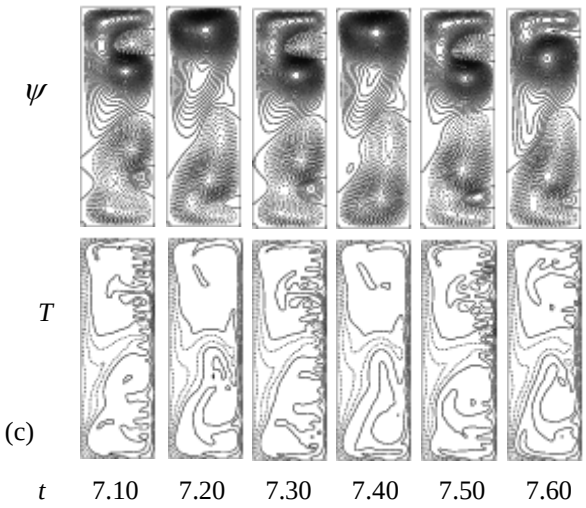

Fig. 4. (a) Time evolution of λ for *Dn* = 500 and *Gr* = 1000 (b) Phase space of the time evolution for *Dn*=500 and *Gr* =1000 (c) Contours of secondary flow patterns (top) and Temperature profiles (bottom) for *Dn* =500 and *Gr* =1000.

In order to investigate the non-linear behaviour of the unsteady solutions, we then performed time evolution of λ for *Dn* = 1000 and *Gr* = 100, 500, 1000, 1500 and 2000, as shown in Fig. 5(a). From Fig. 5(a), we see that the unsteady flow is a chaotic solution for all the cases. Figure 5(b) shows unsteady solution for *Dn* = 1000 and *Gr* = 1000, where we find that the flow oscillates irregularly that is the flow is chaotic at *Dn* = 1000 and *Gr* = 1000. Then we obtained typical contours of secondary flow patterns and temperature profiles for *Dn*=1000 and *Gr*=1000 as shown in Fig. 5(c), and we see that, the unsteady flow at *Dn*=1000 and *Gr*=1000 oscillates between asymmetric four- and six-vortex solutions.

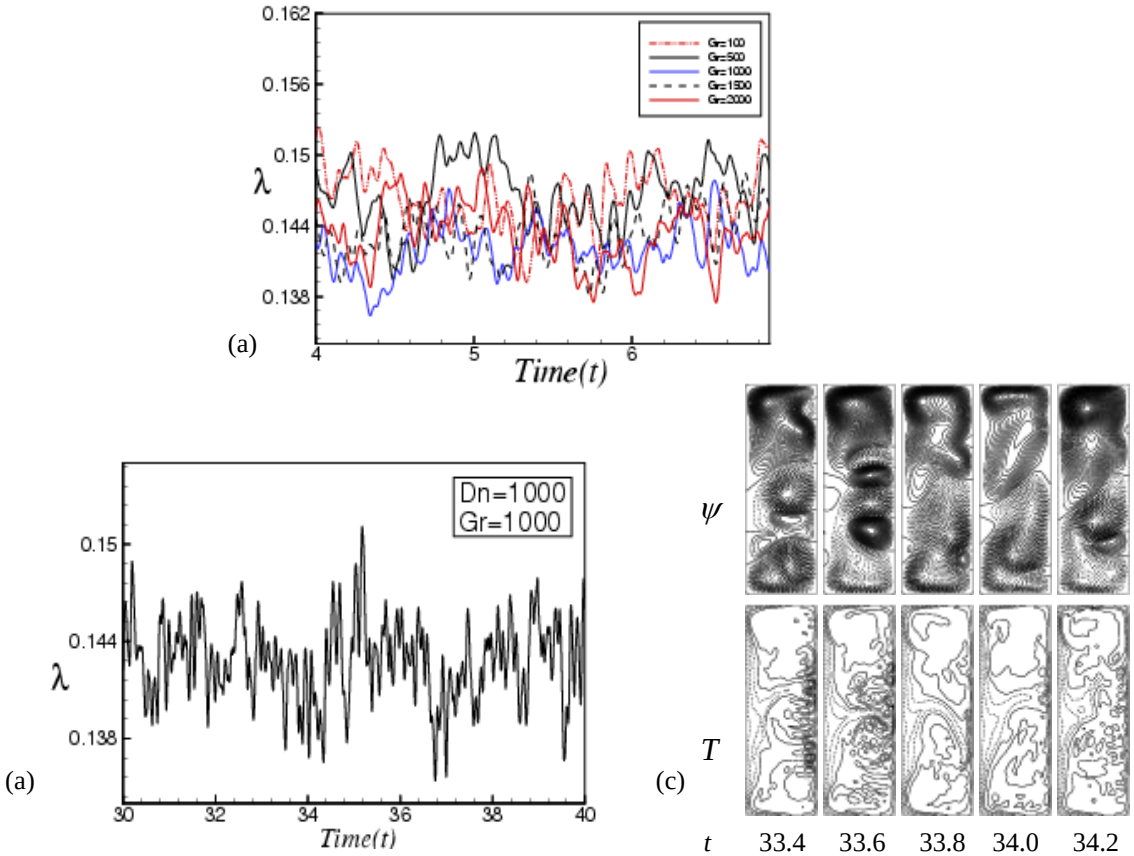

Fig. 5. (a) Time evolution of λ for various values of *Gr* at *Dn*=1000 (b) Time evolution of λ for *Dn*=1000 and *Gr* = 1000, (c) Contours of secondary flow patterns (top) and temperature profiles (bottom) for *Dn*=1000 and *Gr* =1000.

5.2.*Phase diagram in the Dn-Gr plane*

Finally, the complete unsteady solutions, obtained by the time evolution computations in the present study, are shown by a phase diagram in Fig. 6 in the Dean number vs. Grashof number plane for $100 \le Dn \le 1000$ and $100 \le Gr \le 2000$ for the aspect ratio 3. In this figure, the circles indicate steady-state solutions, crosses periodic solutions and triangles chaotic solutions. From Fig. 6, we can easily get to know about the unsteady flow characteristics for various *Dn* and *Gr*. As seen in Fig. 6, the unsteady flow undergoes through various flow instabilities if the Dean number or the Grashof number is increased. It is found that for large value of *Dn*, the flow is chaotic for any value of *Gr* lying in the range investigated in this study.

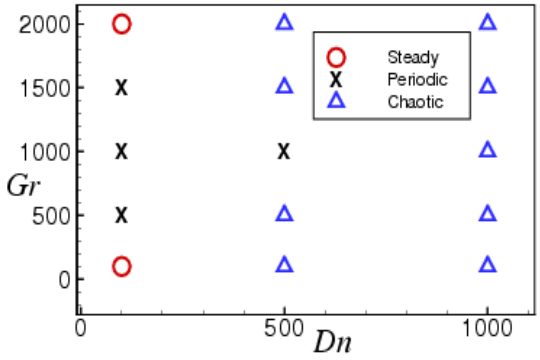

Fig. 6. Distribution of the unsteady solutions in the $Dn - Gr$ plane for $100 \le Dn \le 1000$ and $100 \le Gr \le 2000$ for the curved rectangular duct flow of aspect ratio 3 (○: steady-state solution, ×: periodic solution and △: chaotic solution).

6. Conclusion

In the present study, a comprehensive numerical result is presented for the unsteady flow characteristics through a curved rectangular duct of large aspect ratio 3 over a wide range of the Dean number and the Grashof number. Time evolution calculation as well as their phase spaces show that the unsteady flow is a steady-state solution for *Dn* = 100 at $Gr = 100$ and $Gr = 2000$ but time periodic at $Gr = 500, 1000, 1500$. If the Dean number is increased, the unsteady flow becomes chaotic for any value of *Gr* lying in the range. Contours of secondary flow patterns and temperature profiles are also obtained, and it is found that the unsteady flow consists of a two-, four-, six-, and eight-vortex solutions. It is also found that the chaotic flow enhances heat transfer more significantly than the steady-state or periodic solutions, if the Dean number is increased.

Acknowledgement

Rabindra Nath Mondal, one of the authors, would like to gratefully acknowledge the financial support (Code No.: MoE/Br-17/10 M-15/2007 (part-2)/230(3), dated 25 April 2011) from the Ministry of Education of Bangladesh to conduct this research work. The author would like to express his cordial thanks to this organization.

References

[1] Dean, W. R. (1927). Note on the motion of fluid in a curved pipe. *Phil. Mag.* Vol. **4**(20) pp. 208- 223.
[2] Berger, S.A., Talbot, L., Yao, L. S. (1983). Flow in Curved Pipes, *Annual. Rev. Fluid. Mech*., Vol. **35**, pp. 461-512.
[3] Nandakumar, K. and Masliyah, J. H. (1986). Swirling Flow and Heat Transfer in Coiled and Twisted Pipes, *Adv. Transport Process*., Vol. **4**, pp. 49-112.
[4] Yanase, S., Kaga, Y. and Daikai, R. (2002). Laminar flow through a curved rectangular duct over a wide range of the aspect ratio, *Fluid Dynamics Research*, Vol. **31,** pp. 151-183.
[5] Mondal, R. N. (2006). Isothermal and Non-isothermal Flows Through Curved ducts with Square and Rectangular Cross Sections, *Ph.D. Thesis*, Department of Mechanical Engineering, Okayama University, Japan.
[6] Winters, K. H., (1987). A bifurcation study of laminar flow in a curved tube of rectangular cross-section, *J. Fluid Mech*..Vol. **180**, pp. 343--369.
[7] Mondal, R. N., Kaga, Y., Hyakutake, T. and Yanase, S. (2007). Bifurcation Diagram for Two- dimensional Steady Flow and Unsteady Solutions in a Curved Square Duct, *Fluid Dynamics Research*. Vol. **39**, pp. 413-446.
[8] Yanase, S, Mondal, R. N. and Kaga, Y. (2005). Numerical study of non-isothermal flow with convective heat transfer in a curved rectangular duct., *International Journal of Thermal Sciences*, Vol. **44** (11), pp. 1047-1060.
[9] Mondal, R. N., Uddin, M. S. and Islam, A. (2008). Non-isothermal flow through a curved rectangular duct for large Grashof number, *J. Phy. Sci.*, Vol. **12**, pp. 109-121.
[10] Mondal, Rabindra Nath, Md. Kutub Uddin and Md. Rezaul Karim (2012). Viscous Incompressible Fluid Flow through a Curved Channel with Differentially heated vertical sidewalls, *Int. J. Appl. Engg. & Technology*, Vol. **2**(1), pp. 62-74.

Available online at www.sciencedirect.com

SciVerse ScienceDirect

Procedia Engineering 00 (2012) 000–000

Procedia Engineering

www.elsevier.com/locate/procedia

5th BSME International Conference on Thermal Engineering

Numerical investigation of turbulent heat convection from solid and longitudinally perforated rectangular fins

Md. Farhad Ismail*, M.O. Reza, M.A. Zobaer, Mohammad Ali

Department of Mechanical Engineering, Bangladesh University of Engineering and Technology, Dhaka-1000, Bangladesh

Abstract

Micro heat sinks are adopted in electronics cooling together with different technologies to enhance the heat transfer process. To improve the cooling performance of heat sink, perforations such as small channels of square and circular cross sections are arranged along with stream wise fin's length. A numerical investigation is conducted in this study for three-dimensional fluid flow and convective heat transfer from an array of solid and perforated fins that are mounted on a flat plate. Incompressible air as working fluid is modeled using the Navier–Stokes equations and RNG based k-ε turbulent model is used to predict turbulent flow parameters. Temperature field inside the fins is obtained by solving Fourier law of heat conduction equation. Flow and heat transfer characteristics are presented for Reynolds numbers from 2×10^4 to 3.9×10^4 based on the fin length and Prandtl number is taken as Pr = 0.71. Numerical simulation is validated with the published experimental results of the previous investigators and good agreement is observed. Results show that the fins of circular perforations have remarkable heat transfer enhancement and reduced pressure drop. The results of this study can help designing micro heat sinks for heat removal from electronic devices.

Keywords: Perforated fins; Turbulent flow; Fin effectiveness; Pressure drop, Micro Heat Sink.

1. Introduction

The removal of excessive heat from system components is essential to avoid damaging effects of burning or overheating. Therefore, the enhancement of heat transfer is an important subject of thermal engineering. Extended surfaces (fins) are frequently used in heat exchanging devices for the purpose of increasing the heat transfer between a primary surface and the surrounding fluid. Sahin and Demir, 2008 stated that heat transfer rate from fins can be improved by employing perforations, porosity or slots. They also studied that the heat transfer improvement may be achieved by either of increasing the heat transfer coefficients, or the heat transfer surface area or by both. Sparrow et al., 1982 conducted a numerical study of heat transfer enhancement by introducing strip fins. Due to high demand for lightweight, compact, and economical fins, the optimization of fin size is of great importance. Sparrow and Carranco Ortiz, 1982 experimentally determined heat transfer coefficient on an upstream facing surface that was contained a regular array of holes. El-Sayed et al. (2004) investigated experimentally to determine the optimal position of fin array for turbulent heat transfer, fluid flow and pressure drop in longitudinal rectangular fin array for three different orientations of tested models: (1) parallel flow, (2) impinging flow, and (3) reverse impinging flow in the flow field. Again, according to Fujii et al., 1988, heat transfer equipments have been required to be much more compact in size and light in weight because of space limitation. While a simple solid baffle plate attached to the duct wall enhances heat transfer, a perforated plate attached to

* Corresponding author.
E-mail address: farhadananda.128@gmail.com

the same duct has a better performance (Molki and Hashemi-Esfahanian, 1992). So far by use of perforated fins, one can gain both goals of fin optimization. Dorignac et al., 2005 experimentally determined convective heat transfer on a multi perforated plates and proposed an empirical relation for heat exchange at windward surface of a perforated flat plate.

Heat sink performance can be evaluated by several factors: material, surface area, fin configuration, pumping power and fan requirements. To obtain higher performance from a heat sink, more surface area, less weight, and lower cost are necessary. Thus, efforts to obtain more optimized designs for heat sinks are needed to achieve high thermal performance. Most of the previous studies on pin fins or parallel plate fin heat sinks have considered the geometric configurations of the fins such as shape, size or orientations. Shaeri et al., 2009 compared square perforated pin fin heatsink with solid parallel plate fin heat sinks. In our study, circular perforated pin fins are introduced and compared with the other types of heat sinks. Pressure drag co-efficient and pressure drop due to perforation are also considered as these parameters are responsible for the effective and efficient cooling performance of heat sinks. For this consideration, three-dimensional turbulent fluid flow and convective heat transfer around an array of solid and perforated fins are analyzed numerically. Fins having two perforations with square and circular cross sections are investigated. These perforations are along the fin and their cross section is perpendicular to the fluid flow direction. Boundary conditions, governing equations and computational domain of this study are the same as used by Velayati et al., 2005 and Shaeri et al., 2009.

Nomenclature

A	area	Re_L	Reynolds number, $(\rho UL)/\mu$
A_T	total fin area including perforation	R_{th}	thermal resistance of heat sink
C_P	pressure drag co-efficient	u	fluid velocity at X- direction
D	fin thickness	V	fin volume (L×H×D)
h	convection heat transfer coefficient	V_{void}	void volume ($L\times H_P\times W_P\times N$)
H_P	perforation height	v	inlet velocity
W_P	perforation width	ε_f	fin effectiveness
L	fin length	λ	fluid thermal conductivity
Nu	average Nusselt number, $(hL)/\lambda$	μ	fluid kinematics viscosity
Pr	Prandtl number	ρ	fluid density

3. Problem description

Typical bluff plate model is shown in Fig. 1. The airflow is considered to be steady and turbulent with constant properties. Moreover, air velocities are such that forced convection is dominant for heat transfer mechanism between fins and ambient air and in the perforations. Fin material is assumed to be aluminum with thermal conductivity of 160 $Wm^{-1}K^{-1}$. Such fins are widely used for heat removal from heating surfaces. Fins having the length (L), height (H) and thickness (D) equal to 24, 12 and 4 mm, respectively are assumed for this study. Each perforation has equal height (H_P) and width (W_P) of to 2.25 mm and their length is equal to the fin's length.

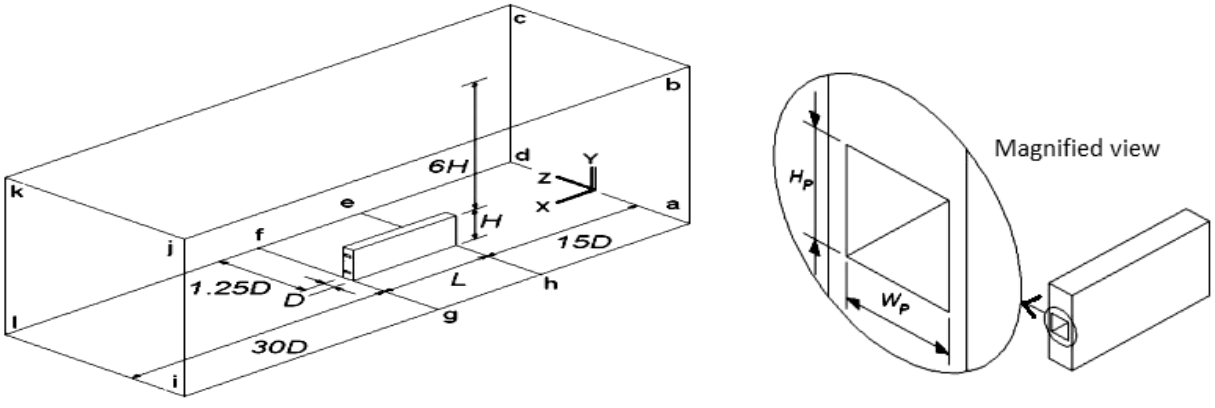

(a) (b)

Fig. 1. (a) Computational domain with the perforated fin (b) magnified view of perforation.

The fin's length is used as the characteristic length for the Reynolds number. The investigations are made for Reynolds number Re= $(\rho vL)/\mu$ in the range of 2×10^4– 3.9×10^4. This range of Reynolds number covers velocity range of 13m/s – 25m/s. These velocities are chosen such that the flow inside the perforations should also be turbulent. Due to uniform air

flow parallel to the fins and symmetry, computations are made for one fin instead of array of fins. Fig. 1(a) shows the computational domain which is similar to the domain used by Velayati et al., 2005 and Shaeri et al., 2009.

4. Numerical method

4.1. Physical model

Physical model and governing equations for the three dimensional steady state incompressible fluid flow and turbulent modeling RNG k-ε are the same as used by Velayati and Yaghoubi, 2005. For calculation of temperature field in the fin's surfaces and perforation's walls, conjugate problem of Fourier's steady state heat conduction equation with convection in the fluid are solved simultaneously. The domain used in the present study is illustrated in Fig. 1(a). The plane abcd is inlet boundary, where steady flow condition is considered for all variables using $u_{in} = u_{\infty}$, and $T_{in} = T_{\infty}$. Free stream temperature is assumed to be 25 ^{0}C and the base plane efgh, has a constant heat flux of 4500 w/m^2. The rest of the planes i.e. adeh and fgil are assumed to be adiabatic. The plane ijkl is considered as exit boundary. For present computation, the effect of radiation heat transfer is neglected. It consists of an entrance region, an exit plane and the upper free stream surface that are planes abcd, ijkl and bckj, respectively.

These planes should be sufficiently far from the fin surfaces so that the results become independent of the boundary positions. For this reason some tests were performed for obtaining an appropriate distance from the fin surfaces that can be found in Velayati and Yaghoubi (2005) and Yaghoubi et al. (2002). In the present study, the length of computational domain is chosen 15D upstream, 30D downstream, 7H in Y direction and 3.5D in Z direction. Fig. 2 (a) and 2 (b) show the perforated fins having two perforations. The solution must be independent of grids. Several grid configurations are studied to ensure that the solutions are grid independent and the test is shown in Fig. 3. From the figure it is observed that 75000 mesh elements are sufficient for the numerical simulation.

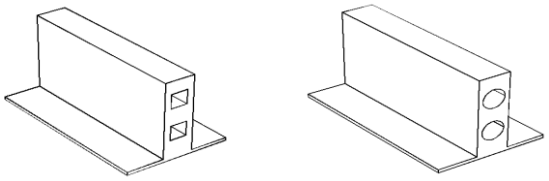

(a) (b)

Fig. 2 (a) Square perforated and (b) circular perforated fins having 2 perforations.

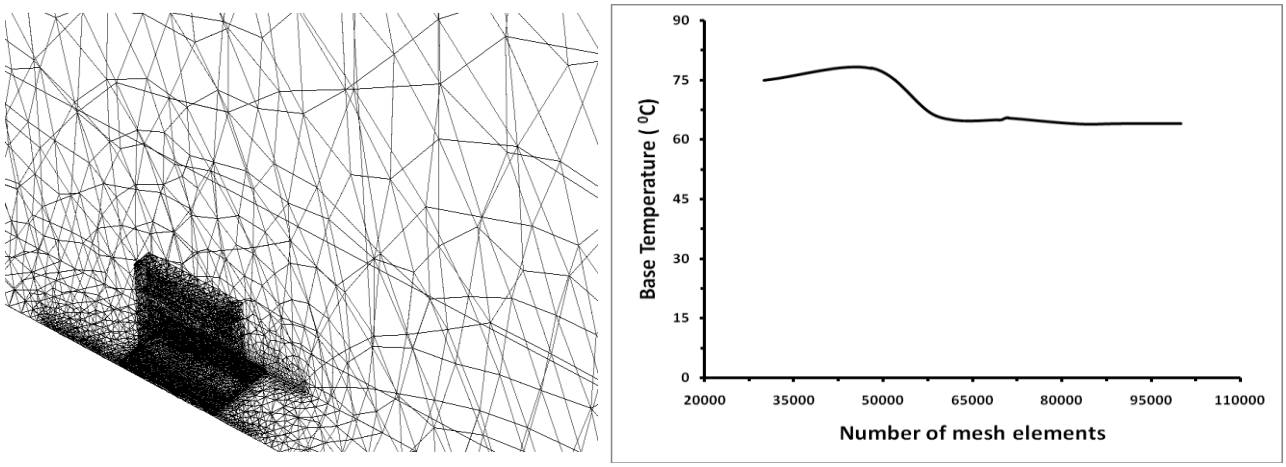

(a) (b)

Fig. 3. (a) Unstructured finer mesh generation at fin surface (b) Grid sensitivity test for the numerical simulation.

4.2. Validation of the numerical simulation

To validate the simulation, numerical results for three dimensional solid fins are compared with the published experimental results of Jonsson and Moshfegh, 2001. Temperature in the inlet of wind tunnel was 20^{0}C. In their experiment as shown in Fig. 4(a), fins had length, height and thickness equal to 52.8, 10 and 1.5 mm, respectively, and spaces between fins were 5 mm. Also wind tunnel had width and height of 63 and 10 mm, respectively. The base of the heat sink was heated

uniformly with 10W. Comparison between present numerical and experimental results is shown in Fig. 4 (b). The Reynolds number is based on the hydraulic diameter of wind tunnel according to definition of Jonsson and Moshfegh (2001). The numerical predictions of heat transfer using the developed code agree well with the experimental results.

The thermal resistance can be calculated by the following equation where h is convective co-efficient and A is heat transfer surface area:

$$R_{th} = \frac{1}{h \cdot A} \left[\frac{\mathrm{K}}{\mathrm{W}}\right] \quad (1)$$

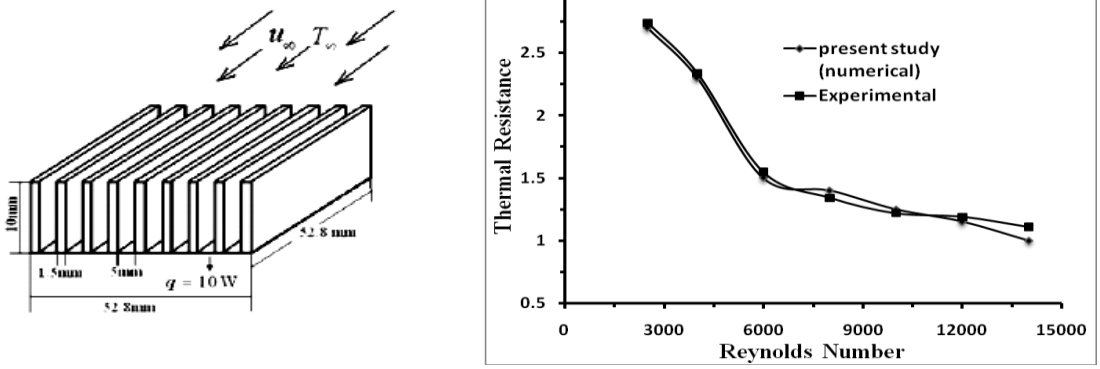

(a) (b)

Fig. 4. (a) Geometric configurations used for the validation of numerical simulation. (b) Comparison between the published experimental and present numerical results.

5. Results and Discussion:

The present analysis of flow field and convection heat transfer for conjugate problem is carried out for $Re_L = 2\times10^4$ to 3.9×10^4, Pr = 0.71. Thermal field in the solid domain is determined by solving conduction equation. The drag force that acts on the faces of perforated fins differs with that of acting on the surfaces of solid fin. The drag force has two components, one is related to surface shear stress as the friction drag and another is due to a pressure differential in the flow direction resulting from wake formation as form or pressure drag.

From Fig. 5(a), it can be noted that the solid fins yields the highest Nusselt number among all the fins. Due to perforations, some portions of the flow passes through the channels and thus the air velocity reduces. Square perforated fins show slightly higher Nusselt Number than that of the circular perforated fins. Fig. 5 (b) illustrates the variation of the thermal resistance with the Reynolds number for different geometries. It is found that when the inlet air temperature and the heat flux are kept constant, the thermal resistance decreases with increasing the Reynolds number. This is because the heat transfer rate increases as the air flow rate increases. Circular perforated fins have slightly higher thermal resistances than that of square perforated fins.

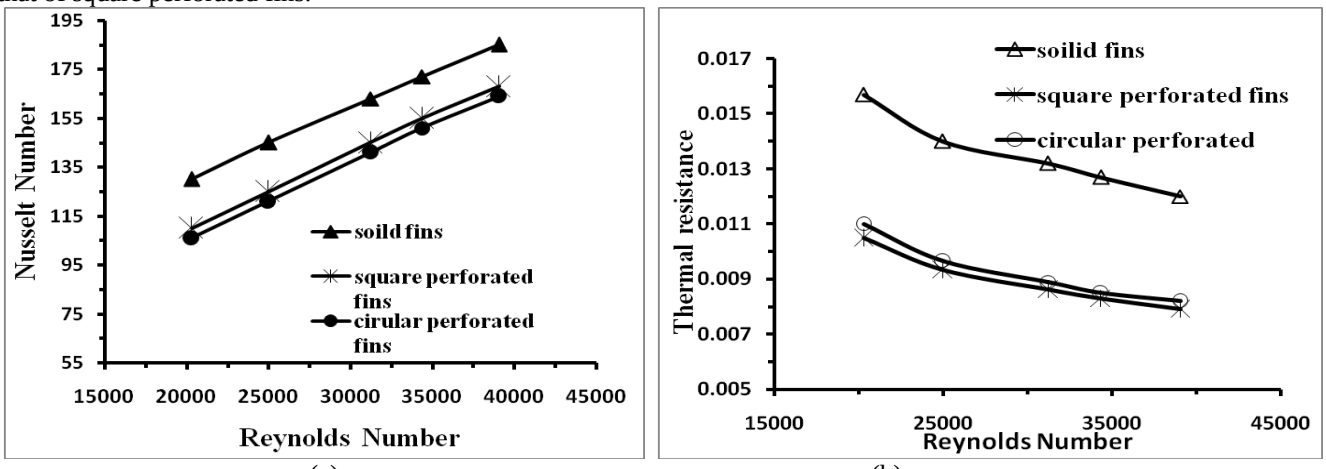

(a) (b)

Fig. 5. (a) Nusselt number variation at different Reynolds number (b) Effects of thermal Resistance for different types of fin configurations.

The parameter fin effectiveness is used to determine fin performance (Incropera and DeWitt, 1996). Fin effectiveness is the ratio of heat transfer from fin to heat transfer from fin base without fin as:

$$\varepsilon_f = \frac{q}{\overline{h_b} A_b (T_b - T_\infty)} \tag{2}$$

Where, where $\hbar_b$ is the average convective heat transfer co-efficient, A_b is the base area, T_b is base temperature, T_s is fin surface temperature and q is heat transfer rate and can be obtained by the following equation,

$$q = \sum h_i \Delta A_i (T_S - T_\infty) \tag{3}$$

Fig. 6 (a) presents heat transfer effectivity for different types of heat sinks. Here fins having 2 and 3 perforations are considered to understand the fin performance clearly. Likewise, the effectivity decreases with the increase of Reynolds number. From the figure 6(a), one can find that perforated fins have higher heat transfer performance and can exchange more heat between primary surface and the ambient air. It is observable that solid fins have the largest average Nusselt number in comparison with perforated fins but perforated fins have larger heat transfer area compared with solid fin and by increase of perforations, heat transfer area becomes larger. From the figure it is also predicted that fins having square and circular perforations have almost same effectivity.

Fig. 6 (b) shows the variation of pressure drag co-efficient for different geometrical configurations. Due to the higher surface force and higher surface roughness, the flow characteristics through the perforated fins is quite high and complex as compare to the solid fins. It can be clearly seen from the figure that the pressure drag co-efficient continues to decrease with the increase of Reynolds number. Throughout the range of velocities, soid fins have the highest pressure drag co-efficient as these fins have maximum frontal surface area. Square perforated fins have higher pressure drag co-efficient than circular perforated fins. So, square perforated fins require more power to circulate the coolant than the circular perforated fins. Pressure drag co-efficient can be obtained by the following equation where ΔP is the pressure difference between the inlet and the frontal surface of fins-

$$c_p = \frac{\Delta p}{1/2 \cdot \rho \cdot v^2} \tag{4}$$

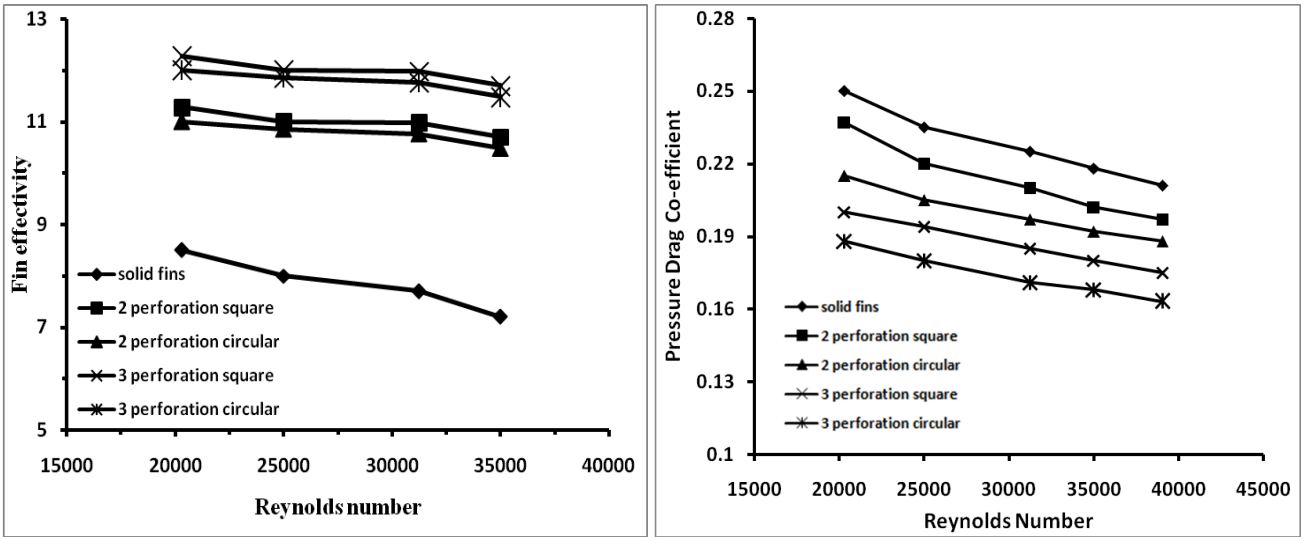

(b)

Fig. 6. (a) Variation of fin effectivity, (b) Variation of pressure drag co-efficient for different types of fin configurations.

5. Conclusions

Thermal performance of perforated and solid fins is numerically investigated in this paper. Generally optimization of fins is focused on to maximize heat dissipation rate and to minimize pressure drop for a given mass or volume of the heat sink. Perforated fins have higher contact surface with the fluid in comparison with the solid fins. Thus the perforated fins have higher effectivity than the solid fins. Again, it is found that though circular and square perforated fins have almost the same amount of heat removal rate but circular perforated fins have significantly less pressure drop than that of square perforated fins. Hence, fin optimization for practical applications can be achieved by the new types of perforated fins.

Acknowledgements

The authors would like to express their appreciation to the Heat Transfer Lab of Bangladesh University of Engineering & Technology (BUET) for providing technical support for this study.

References

[1] Dorignac, E., Vullierme, J.J., Broussely, M., Foulon, C., Mokkadem, M., "Experimental heat transfer on the windward surface of a perforated flat plate," Int. J. Therm. Sci. 44 (2005), 885–893.
[2] El-Sayed, S.A., Mohamed, Sh.M., Abdel-latif, A.A., Abouda, Ah.E., "Experimental study of heat transfer and fluid flow in longitudinal rectangular-fin array located in different orientations in fluid flow," Exp. Therm. Fluid Sci. 29 (2004), 113–128.
[3] Fujii, M., Seshimo, Y., Yamanaka, G., "Heat transfer and pressure drop of perforated surface heat exchanger with passage enlargement and contraction," Int. J. Heat Mass Transfer 31 (1988), 135–142.
[4] Incropera, F.P., DeWitt, D.P., "Introduction to Heat Transfer," third ed.. JohnWiley & Sons, Inc. (1996).
[5] Jonsson, H., Moshfegh, B., "Modeling of the thermal and hydraulic performance of plate fin, strip fin, and pin fin heat sinks—influence of flow by pass," IEEE Transactions on Components and Packaging Technologies 24 (2001), 142–149.
[6] Jonsson H. and B. Moshfegh, "Influence of fin spacing, fin thickness, and inlet velocity on the performance of plate fin heat sinks under varying bypass conditions using CFD," Int. J. Heat Exchangers (IJHEX), vol. 1, no. 2, pp. 177–196, 2000.
[7] Liou, T.M., Chen, S.H., "Turbulent heat and fluid flow in a passage distributed by detached perforated ribs of different heights," Int. J. Heat Mass Transfer 41, 1795–1806 (1998).
[8] Meinders, E.R., Van der meer, T.H., Hanjalic, K., "Local convection heat transfer from an array of wall-mounted cubes" Int. J. Heat Mass Transfer 41 (2), 335–346 (1998).
[9] Molki, M., Hashemi-Esfahanian, A., "Turbulent convective mass transfer downstream of a perforated baffle blockage," Int. J. Heat Fluid Flow 13 (1992), 116–123.
[10] Nilles, M.J., Calkins, M.E., Dingus, M.L., Hendricks, J.B., "Heat transfer and flow friction in perforated plate heat exchangers," Exp. Therm. Fluid Sci. 10, 238–247 (1995).
[11] Shaeri M.R., M. Yaghoubi, "Numerical analysis of turbulent convection heat transfer from an array of perforated fins," International Journal of Heat and Fluid Flow 30 (2009) 218–228.
[12] Sahin, B., Demir, A., "Performance analysis of a heat exchanger having perforated square fins," Appl. Therm. Eng. 28 (2008), 621–632.
[13] Sparrow E. M. and C. H. Liu, "Heat-transfer, pressure-drop and performance relationships for in-line, staggered, and continuous plate heat exchangers," Int. J. Heat Mass Transf., vol. 22, pp. 1613–1625, 1979.
[14] Sparrow, E.M., Carranco Ortiz, M., 1982. Heat transfer coefficients for the upstream face of a perforated plate positioned normal to an oncoming flow. Int. J. Heat Mass Transfer 25 (1), 127–135
[15] Velayati, E., Yaghoubi, M., "Numerical study of convective heat transfer from an array of parallel bluff plates," Int. Journal of Heat Fluid Flow 26, 80–91 (2005).

Available online at www.sciencedirect.com

SciVerse ScienceDirect

Procedia Engineering 00 (2012) 000–000

Procedia Engineering

www.elsevier.com/locate/procedia

5th BSME International Conference on Thermal Engineering

Radiation Effects on MHD Free Convection Flow along Vertical Flat Plate in Presence of Joule Heating and Heat Generation

Mohammad Mokaddes Ali[a], A.A. Mamun[b], Md. Abdul Maleque[c], Nur Hosain Md. Ariful Azim[d]

[a]Department of Mathematics , Mawlana Bhashani Science and Technology University, Tangail-1902, Bangladesh
[b]Institute of Natural Science, United International University, Dhaka-1209, Bangladesh
[c]Department of Mathematics, Bangladesh University of Engineering and Technology, Dhaka-1000, Bangladesh
[d]School of Business Studies, Southeast University, Dhaka-1213, Bangladesh

Abstract

In this paper, the effect of radiation on magnetohydrodynamic (MHD) free convection flow along a vertical flat plate in presence of Joule heating and heat generation have been investigated. The governing equations associated with the conduction based boundary conditions are transformed into dimensionless form employing the appropriate transformations and then solved numerically using the implicit finite difference method with Keller box scheme. The numerical solutions are obtained in terms of velocity profiles, temperature distributions, skin friction coefficient and heat transfer rate and then presented graphically and discussed. A complete parametric analysis is done on these numerical results to show the effects of the magnetic parameter, radiation parameter, Joule heating parameter and heat generation parameter. It is found that radiation, Joule heating and heat generation play significant role on MHD natural convection flow during heat transfer. To illustrate the accuracy of the results, the present results for the local skin friction and surface temperature distribution excluding the effects of magnetic field parameter, radiation parameter, Joule heating parameter and heat generation parameter are compared with the results of Merkin and Pop designed for the fixed value of Prandtl number and an excellent agreement were found.

Keywords: Radiation; MHD; Joule heating; Heat generation; Vertical flat plate; Finite difference method

* Corresponding author. Tel.: +8801743939681; fax: +88-0921-55400.
E-mail address: mmokaddesali@yahoo.com

Nomenclature

C_{fx}	Local skin friction coefficient (-)	Nu_x	Local Nusselt number(-)
C_p	Specific heat at constant pressure (Jkg^{-1}K^{-1})	q_w	Heat flux (Wm^{-2})
f	Dimensionless stream function (-)	$\bar{u}$, $\bar{v}$	Dimensional velocity components (ms^{-1})
g	Acceleration due to gravity (ms^{-2})	u , v	Dimensionless velocity components (-)
Gr	Grashof number (-)	$\bar{x}$, $\bar{y}$	Dimensional Cartesian co-ordinates (m)
h	Dimensionless temperature(-)	x , y	Dimensionless Cartesian coordinates(-)
k_f , k_s	Fluid and solid thermal conductivities(Wm^{-1}K^{-1})		

Greek symbols

β	Coefficient of thermal expansion(K^{-1})	σ	Electrical conductivity (-)
η	Dimensionless similarity variable(-)	τ_w	Shearing stress(-)
μ , ν	Dynamic and kinematic viscosities(kgm^{-1}s^{-1})	ψ	Stream function (m^{2}s^{-1})
ρ	Density of the fluid (kgm^{-3})		

1. Introduction

Heat transfer in presence of magnetic field has received much attention by many researchers due to its potential used in science, engineering and industrial applications such as nuclear power plants, cooling of transmission lines and electric transformer etc. Accordingly, effect of radiation on MHD is of considerable interest because of its wider applications in space technology and others. Many researchers studied the effect of radiation on magnetohydrodynamic free convection flows under diverse surface boundary conditions using different mathematical technique. The problem of natural convection-radiation interaction on boundary layer flow with Rosscland diffusion approximation along a vertical thin cylinder has been investigated by Hossain and Alim [1]. Hossain and Takhar [2] employed finite difference approximation to analyze the effects of conduction-radiation interaction on natural convection boundary layer flow of a viscous incompressible fluid along an isothermal horizontal plate. Abdel-naby *et al.* [3] studied the radiation effects on MHD unsteady free convection flow over a vertical plate with variable surface temperature. Hossain [4] analyzed the effect of viscous and Joule heating effects on MHD free convection flow with variable plate temperature. The heat generation effect on MHD natural convection flow along a vertical flat plate was studied by Mamun *et al.* [5] employing finite difference techniques. Palani and Kim [6] applied implicit finite difference scheme of Crank-Nicolson method to analyze the importance of Joule heating and viscous dissipation effects on MHD flow along inclined plate subject to variable surface temperature.

In the above studies some have considered only the effects of radiation or the effect of Joule heating and heat generation on free convection flow including or excluding magnetohydrodynamic effect for various geometries. However, as no work has been conducted combinedly along a vertical plate, so we attempted to find out the effect of radiation on MHD free convection flow along a vertical flat plate in presence of Joule heating and heat generation in this analysis and then a detailed derivations of the governing equations and solution procedure are described in the following sections.

2. Governing equations of the flow

Let us consider a steady free convection boundary layer flow of an incompressible and electrically conducting fluid along a vertical flat plate. Let l and b are the length and thickness of the plate, respectively. T_b is the temperature at the outer surface of the plate and T_∞ is the temperature of the ambient fluid where $T_b < T_\infty$. A uniform magnetic field of strength H_0 is acted along the $\bar{y}$ -axis. The $\bar{x}$ -axis is taken along the vertical flat plate in upward direction and the $\bar{y}$ -axis is normal to the plate. The flow configuration of physical model and coordinates system as:

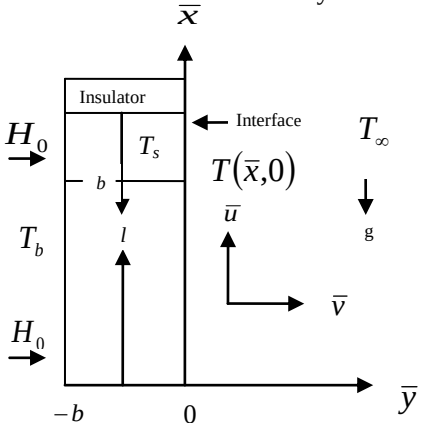

Fig: 1. Physical model and coordinate system.

The equations governing the flow under these assumptions with the Bousinesq approximation can be expressed as follows:

$$\frac{\partial \bar{u}}{\partial \bar{x}} + \frac{\partial \bar{v}}{\partial \bar{y}} = 0 \tag{1}$$

$$\bar{u}\frac{\partial \bar{u}}{\partial \bar{x}} + \bar{v}\frac{\partial \bar{u}}{\partial \bar{y}} = \nu \frac{\partial^2 \bar{u}}{\partial \bar{y}^2} + g\beta(T_f - T_\infty) - \frac{\sigma H_0^2 \bar{u}}{\rho} \tag{2}$$

$$\bar{u}\frac{\partial T}{\partial \bar{x}} + \bar{v}\frac{\partial T}{\partial \bar{y}} = \frac{k_f}{\rho C_p}\frac{\partial^2 T}{\partial \bar{y}^2} - 4\Gamma(T_f - T_b) + \frac{\sigma H_0^2 \bar{u}^2}{\rho C_p} + \frac{Q_0}{\rho C_p}(T_f - T_\infty) \tag{3}$$

where $\Gamma = \int_0^\infty K_{\lambda b}\left(\partial e_{b\lambda}/\partial T_f\right)d\lambda$, $K_{\lambda b} = K_\lambda(T_b)$ is the mean absorption coefficient, $e_{b\lambda}$ is Plank's function and T_f is the temperature of the fluid in the boundary layer. The following boundary conditions based on conduction are considered to solve the governing equations:

$$\bar{u} = \bar{v} = 0,\ T_f = T(\bar{x}, 0),\ \frac{\partial T_f}{\partial \bar{y}} = \frac{k_s}{b k_f}\left(T_f - T_b\right) \ \ at\ \ \bar{y} = 0,\ \bar{x} > 0 \text{ and } \bar{u} \to 0,\ T_f \to T_\infty \ \ at\ \ \bar{y} \to \infty,\ \bar{x} > 0 \tag{4}$$

The governing equations and the boundary conditions (1)-(4) are made non-dimensional, using the following non-dimensional variables:

$$x = \frac{\bar{x}}{l},\ y = \frac{\bar{y}}{l}Gr^{1/4},\ u = \frac{\bar{u}\,l}{\nu}\,Gr^{-1/2},\ v = \frac{\bar{v}\,l}{\nu}\,Gr^{-1/4},\ \theta = \frac{T_f - T_\infty}{T_b - T_\infty},\ Gr = \frac{g\beta l^3 (T_b - T_\infty)}{\nu^2}$$

where θ is the dimensionless temperature. The non dimensional forms of the governing equations are:

$$\frac{\partial u}{\partial x} + \frac{\partial v}{\partial y} = 0 \tag{5}$$

$$u\frac{\partial u}{\partial x} + v\frac{\partial u}{\partial y} + Mu = \frac{\partial^2 u}{\partial y^2} + \theta \tag{6}$$

$$u\frac{\partial \theta}{\partial x} + v\frac{\partial \theta}{\partial y} = \frac{1}{\Pr}\frac{\partial^2 \theta}{\partial y^2} - R\ (\theta - 1) + J u^2 + Q\theta \tag{7}$$

and the corresponding boundary condition (4) can be written as in the following dimensionless form:

$$u = v = 0,\ \theta - 1 = p\frac{\partial \theta}{\partial y} \ \ at \ \ y = 0,\ x > 0 \text{ and } u \to 0,\ \theta \to 0 \ \ at\ y \to \infty,\ x > 0 \tag{8}$$

here $M = \left(\sigma H_0{}^2 l^2/\mu\right)Gr^{-1/2}$ is the magnetic parameter, $R = \left(4\Gamma l^2/\nu\right)Gr^{-1/2}$ is the radiation parameter, $Pr = \mu C_p/K_f$ is the Prandtl number, $Q = Q_0\, l^2 Gr^{-1/2}/\mu C_p$ is the heat generation parameter, $J = \sigma H_0^2\, \nu Gr^{1/2}/\rho C_p\,(T_b - T_\infty)$ is the Joule heating parameter and $p = \left(k_f/k_s\right)(b/l)Gr^{1/4}$ in the boundary condition is a conjugate conduction parameter. The value of the conjugate conduction parameter *p* depends on (b/l), $\left(k_f/k_s\right)$ and Gr but each of which depends on the types of considered fluid and the solid. In the present analysis we have taken *p* = 1. The momentum and the energy equations (6) and (7) are transformed into the following nonlinear partial differential equations using similarity transformations

$\psi = x^{4/5}(1+x)^{-1/20} f(x,\eta),\ \ \eta = yx^{-1/5}(1+x)^{-1/20},\ \ \theta = x^{1/5}(1+x)^{-1/5} h(x,\eta)$ are

$$f''' + \frac{16+15x}{20(1+x)} ff'' - \frac{6+5x}{10(1+x)} f'^2 - Mx^{2/5}(1+x)^{1/10} f' + h = x\left(f'\frac{\partial f'}{\partial x} - f''\frac{\partial f}{\partial x}\right), \tag{9}$$

$$\frac{1}{\Pr}h'' + \frac{16+15x}{20(1+x)} fh' - \frac{1}{5(1+x)} f h - R x^{2/5}(1+x)^{1/10} h + R x^{1/5}(1+x)^{3/10} + J x^{7/5}(1+x)^{1/10} f'^2 + Q x^{2/5}(1+x)^{1/10} h = x\left(f'\frac{\partial h}{\partial x} - h'\frac{\partial f}{\partial x}\right), \tag{10}$$

Here the primes denote partial derivative with respect to η. The boundary conditions (8) take the following form:

$$\left.\begin{array}{l} f(x,0) = f'(x,0) = 0,\ \ h'(x,0) = -(1+x)^{1/4} + x^{1/5}(1+x)^{1/20} h(x,0) \ \ \ at\ \ y = 0 \\ f'(x,\infty) \to 0,\ \ \ h(x,\infty) \to 0 \ \ \ \ at\ \ y \to \infty \end{array}\right\} \tag{11}$$

Comparison of the results

The comparison of the skin friction coefficients and the surface temperature between the present work and the work of

Merkin and Pop [8] are shown in the following table. We observed in this table, the present analysis is an excellent agreement with the published work of Merkin and Pop [8].

Table 1.Comparison of the present numerical results of the skin friction (C_{fx}) and surface temperature ($\theta(x, 0)$) with Prandtl number Pr = 0.733, M = 0.00, R = 0.00, J = 0.01 and Q = 0.00.

	Merkin and Pop [8]		Present work	
$x^{\frac{1}{5}} = \xi$	C_{fx}	$\theta(x, 0)$	C_{fx}	$\theta(x, 0)$
0.7	0.430	0.651	0.424	0.651
0.8	0.530	0.686	0.529	0.687
0.9	0.635	0.715	0.635	0.716
1.0	0.745	0.741	0.744	0.741
1.1	0.859	0.762	0.860	0.763
1.2	0.972	0.781	0.975	0.781

3. Results and discussion

The numerical results are calculated from the solutions of the governing equations (9) and (10) subject to the boundary conditions represented in the equation (11).The numerical values of the velocity, temperature, local skin friction coefficient and rate of heat transfer are obtained for different values of magnetic parameter M, radiation parameter R, Joule heating parameter J and heat generation parameter Q for a Prandtl number of 0.73. Detailed numerical results for the velocity, temperature, local skin friction coefficients and rate of heat transfer associated with the different values of related parameters are presented graphically in Fig. 2-9, respectively.

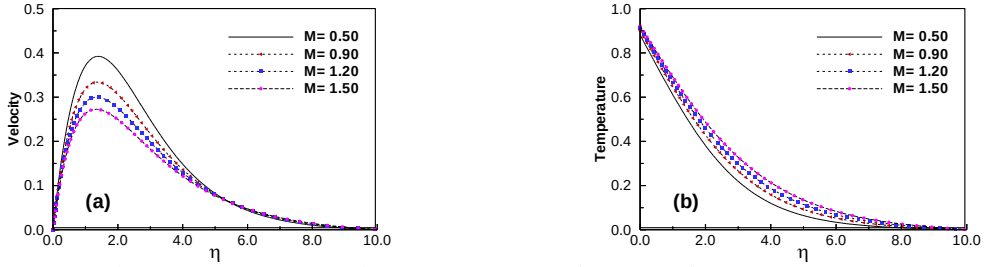

Fig. 2: (a) Variation of velocity and (b) variation of temperature against η for varying of M with R = 0.001, J = 0.01 and Q = 0.01.

The effects of different values of magnetic parameter M on the velocity profiles and temperature distribution are illustrated in Fig. 2(a) and Fig. 2(b), respectively. The applied magnetic field produces Lorentz force due to the interaction with the flowing fluid particles. This force opposes the motion of the fluid, as a result the velocity of the fluid decreases with the increasing of M observed in Fig.2 (a). It reveals that the shape of the velocity profile increases near the interface and then begins to decrease thereafter. The temperature increases within the boundary layer for the increasing values of magnetic field parameter due to interaction of fluid flow and magnetic field which is illustrated in Fig.2 (b).

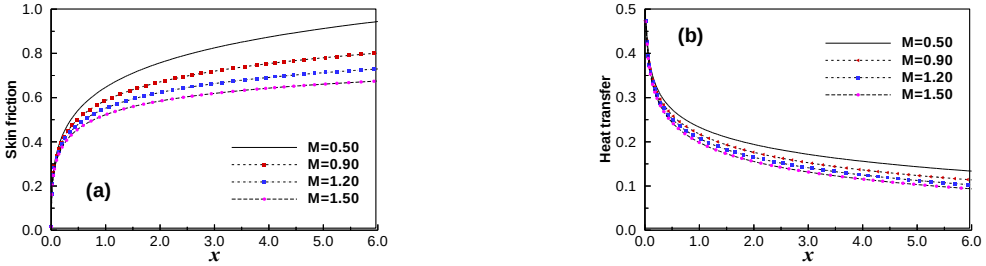

Fig. 3: (a) Variation of skin friction and (b) variation of heat transfer against x for varying of M with R = 0.001, J = 0.01 and Q = 0.01.

Fig.3 illustrates the skin friction coefficient and the rate of heat transfer for the variation of magnetic parameter M while R = 0.001, J = 0.01 and Q = 0.01. Since the velocity of the fluid decreases for increasing values of magnetic parameter as mentioned earlier, accordingly, the skin friction on the plate decreases as observed in Fig.3 (a). Moreover, the temperature within the boundary layer increases (Fig. 2(b)) for the increasing M, which result, the heat transfer rate from the plate to fluid decreases as shown in Fig. 3 (b).

Fig.4 (a) and Fig. 4 (b) depict the velocity and temperature distributions, respectively for some selected values of the radiation parameter R together with a certain value of M, J and Q. Fluid absorbed heat while radiation imitates from the heated plate. As a result the motion and the temperature of the fluid increase within the flow region. It is also observed that the velocity profiles shift upward and the position of peak velocity moves outward from the plate for the increasing R (4(a)).

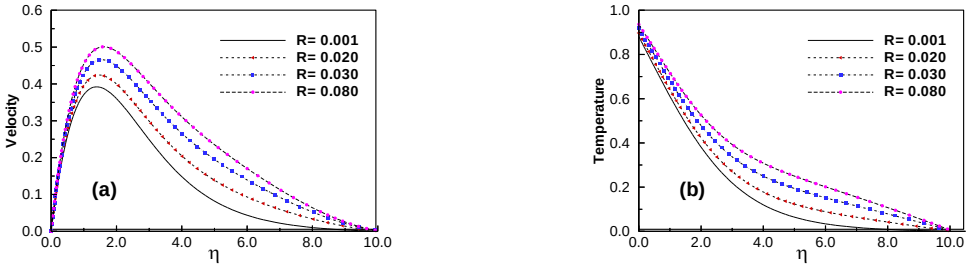

Fig. 4: (a) Variation of velocity and (b) variation of temperature against η for varying of R with M = 0.50, J = 0.01 and Q = 0.01.

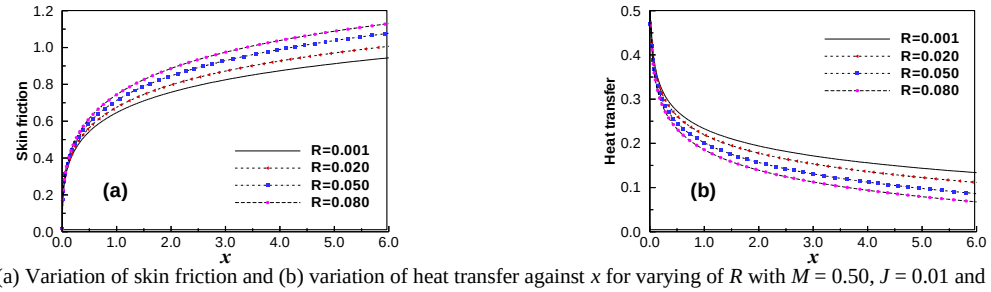

Fig. 5: (a) Variation of skin friction and (b) variation of heat transfer against x for varying of R with M = 0.50, J = 0.01 and Q = 0.01.

The skin friction coefficient and the rate of heat transfer against x for various values of radiation parameter R are illustrated in Fig.5 (a) and Fig.5 (b), respectively. The increased values of the radiation parameter accelerate the fluid motion (Fig.4 (a)) within the boundary layer. As a result, the friction between the surface of the plate and the fluid increases as observed in Fig.5 (a).The skin friction increase significantly for a particular value of radiation parameter R with the increasing value of x. Increasing temperature in the flow region decreases temperature difference between the outer surface of the plate and the flow field. Consequently, the rate of heat transfer decreases for increasing value of radiation parameter as shown in Fig.5(b).

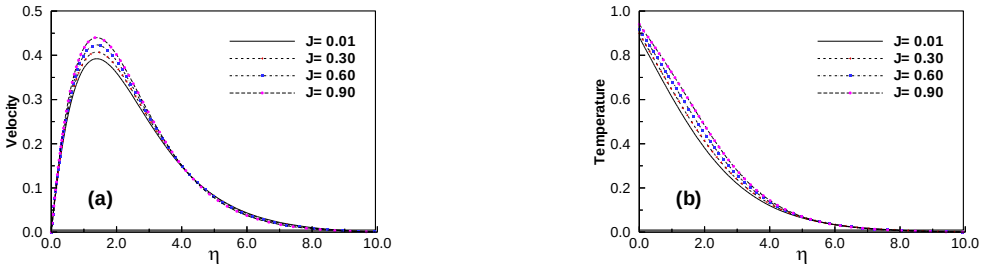

Fig. 6: (a) Variation of velocity and (b) variation of temperature against η for varying of J with M = 0.50, R = 0.001 and Q = 0.01.

The above figures (6(a) and 6(b)) represent the effect of Joule heating parameter J on velocity and temperature field while the controlling parameters are M = 0.50, R = 0.001 and Q = 0.01. As Joule heating parameter produce temperature in the conductor, therefore the velocity and temperature of the fluid increase associated with the increasing values of J.

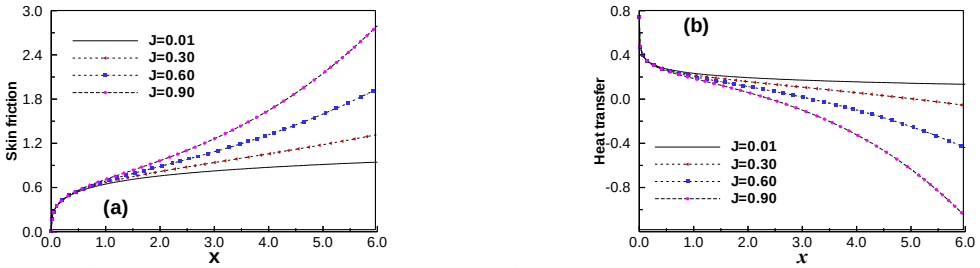

Fig. 7: (a) Variation of skin friction and (b) variation of heat transfer against x for varying of J with M = 0.50, R = 0.001 and Q = 0.01.

Fig. 7(a) and Fig. 7(b) illustrate the local skin friction coefficient and heat transfer rate for different values of J with increasing x and fixed value of controlling parameters. Since the velocity of the fluid increase with the increasing of J that has been shows in Fig. 6(a), accordingly, the corresponding skin friction coefficient increases. The increased temperature due to increasing of Joule heating parameter increases the interfacial temperature, for that reason the heat transfer rate from the plate to fluid decreases which is shown in Fig. 7 (b).

The velocity of the fluid increases by the increasing value of Q, because of the effects of Q generates heat in the flow region

as a result, the temperature of the fluid increase within the thermal boundary layer. These phenomenon are presented in the Fig. 8 (a) and 8 (b), respectively. On the other hand, heat generation parameter effects positively (increase) in the skin friction and negatively (decrease) in the heat transfer rate which are shown in the Fig.9 (a) and 9(b), respectively. These effects actually occur due to the increased rate of velocity by Q, that leads to increase of skin friction along the surface of the vertical flat plate and the presence of heat generator creates a hot fluid layer adjacent to the surface due to the heat generation mechanism, accordingly, the heat transfer rate decrease from the surface to the fluid.

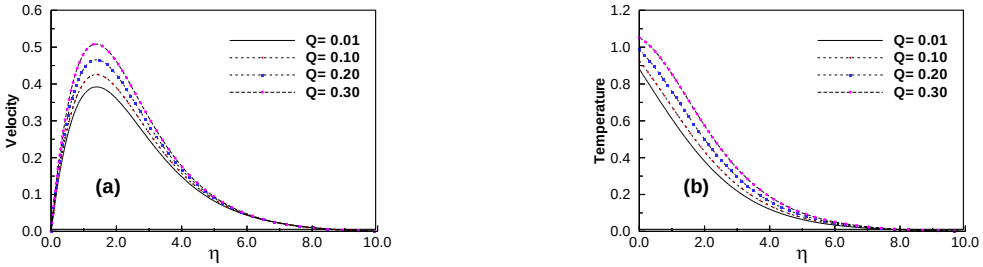

Fig. 8: (a) Variation of velocity and (b) variation of temperature against η for varying of Q with M = 0.50, R = 0.001 and J = 0.01.

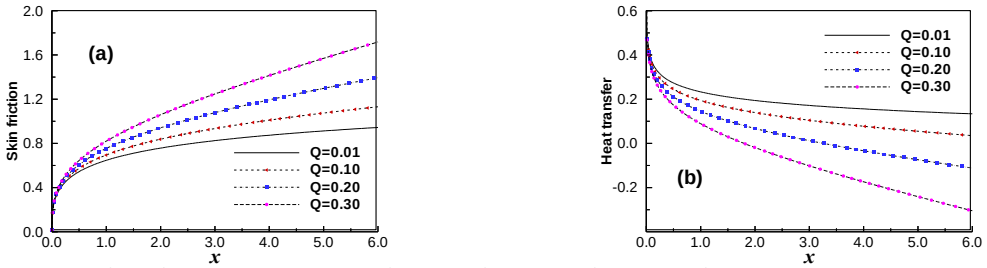

Fig. 9: (a) Variation of skin friction and (b) variation of heat transfer against x for varying of Q with M = 0.50, R = 0.001 and J = 0.01.

4. Conclusion

In this analysis the effect of radiation and heat generation on magnetohydrodynamic (MHD) natural convection flow along a vertical flat plate in presence of Joule heating has been analyzed for some selected values of pertinent parameters including magnetic parameter, radiation parameter, Joule heating parameter and heat generation parameter. From the present investigation, it may be concluded that the velocity of the fluid and the skin friction at the interface decrease with the increasing magnetic parameter while they increase with the increasing radiation parameter, Joule heating parameter and heat generation parameter .The temperature of the fluid increases with the increasing magnetic parameter, radiation parameter, Joule heating parameter and heat generation parameter but opposite results arise for heat transfer rate.

References

[1] Hossain M. A. and Alim M. A., 1997. Natural convection-radiation interaction on boundary layer flow along a thin vertical cylinder, Journal of Heat and Mass Transfer 32, p. 515-520.

[2] Hossain M. A., Takhar H. S., 1999. Thermal radiation effects on natural convection flow over an isothermal horizontal plate, Heat and Mass Transfer 35, p. 321-326.

[3] Abd El-Naby M. A., Elsayed M. E. Elbarbary and Nader Y. Abdelazem, 2003. Finite difference solution of radiation effects on MHD unsteady free convection flow over vertical plate with variable surface temperature, Journal of Applied Mathematics 2003, 2, p.65-86.

[4] Hossain M. A., 1992. Viscous and Joule heating effects on MHD free convection flow with variable surface temperature, International Journal of Heat and Mass Transfer 35, p.3485-3487.

[5] Mamun A. A, Chowdhury Z. R, Azim M. A. and Molla M. M., 2008. MHD-conjugate heat transfer analysis for a vertical flat plate in presence of viscous dissipation and heat generation, International Journal Communications in Heat and Mass Transfer 35, p. 1275-1280.

[6] Palani G. And Kwang Young Kim, 2011. Joule heating and viscous dissipation effects on MHD flow past a semi-infinite inclined plate with variable surface temperature, Journal of Engineering Thermophysics 20, p. 501-517.

[7] Pozzi, A. and Lupo, M., 1988. The coupling of conduction with laminar natural convection along a flat plate, International Journal of Heat Mass Transfer 31, p. 1807-1814.

[8] Merkin, J. H. and Pop, I., 1996. Conjugate free convection on a vertical surface, International Journal of heat and Mass transfer 39, p. 1527-1534.

[9] Keller, H. B., 1978. Numerical methods in the boundary layer theory, Ann. Rev. of Fluid Mech. 10, p.417-433.

[10] Cebeci, T. and Bradshow, P., 1984. Physical and Computational Aspects of Convective Heat Transfer, Springer, New York.

Available online at www.sciencedirect.com

SciVerse ScienceDirect

Procedia Engineering 00 (2012) 000–000

Procedia Engineering

www.elsevier.com/locate/procedia

5th BSME International Conference on Thermal Engineering

Analysis of heat transfer and fluid flow in a triangular enclosure in presence of an adiabatic fin

Sreebash C. Paul[a,*], Suvash C. Saha[b], Y. T. Gu[b]

[a]*Department of Arts and Sciences, Ahsanullah University of Science and Technology, 141-142 Love Road, Tejgaon I/A, Dhaka 1208, Bangladesh.*
[b]*School of Chemistry, Physics & Mechanical Engineering, Queensland University of Technology, 2 George St., GPO Box 2434, Brisbane QLD 4001, Australia.*

Abstract

Natural convection thermal boundary layer adjacent to the heated inclined wall of a right angled triangle with an adiabatic fin attached to that surface is investigated by numerical simulations. The finite volume based unsteady numerical model is adopted for the simulation. It is revealed from the numerical results that the development of the boundary layer along the inclined surface is characterized by three distinct stages, i.e. a start-up stage, a transitional stage and a steady stage. These three stages can be clearly identified from the numerical simulations. Moreover, in presence of adiabatic fin, the thermal boundary layer adjacent to the inclined wall breaks initially. However, it is reattached with the downstream boundary layer next to the fin. More attention has been given to the boundary layer development near the fin area.

Keywords: Heat Transfer, Triangular enclosure, Fin, Boundary layer

Nomenclature

A	Aspect ratio of the cavity	U, V	Dimensional velocity components
g	Acceleration due to gravity	u,v	Non-dimensional velocity components
H	Dimensional height of the cavity	X, Y	Dimensional coordinates
L	Dimensional base length of the cavity	x,y	Non-dimensional coordinates
Nu	Nusselt number	*Greek symbols*	
P	Dimensional pressure	β	thermal expansion coefficient
p	Non-dimensional pressure	ΔT	temperature difference between hot and cold wall
Pr	Prandtl number	κ	thermal diffusivity
Ra	Rayleigh number	ρ	Density
T	Dimensional fluid temperature	ν	kinematic viscosity
T_c	Dimensional cold temperature	θ	Non-dimensional temperature
T_h	Dimensional hot temperature	τ	Non-dimensional time

1. Introduction

Heat transfer due to natural convection in triangular enclosures is of fundamental interest in the fluid mechanics research community and has application to buildings, solar collectors, and greenhouses. Controlling heat transfer by improving or

* Corresponding author. Tel.: +880-2-8870418, Ext. 1802; fax: +880-2-8870417.
E-mail address: sreebash@yahoo.com

depressing natural convection flows within an enclosure is of considerable importance in industrial applications. The use of fins on the wall of an enclosure is an efficient way to alter heat transfer through the cavity.

A study on heat transfer by free convection in right triangular enclosures was performed by Akinsete and Coleman, 1982. The base, the inclined wall and the vertical wall of the enclosure was assumed to be cooled, heated and adiabatic respectively. In their investigation it was found an increase in heat transfer near the apex of the cooled and heated wall. To investigate this issue, Moukalled and Acharya, 2000, 2001 investigated natural convection in a trapezoidal enclosure by mounting baffles from the base and the inclined wall, and they observed a significant decrease in heat transfer.

Xu et al., 2008, 2009 and 2010 performed experimental well as numerical investigation on natural convection in a differentially heated rectangular cavity with or without fin on a sidewall for high Rayleigh number. They observed strong oscillations in the thermal flow above the fin caused by a Rayleigh-Benard-type instability in the flow. Oscillations in the boundary layer triggered the boundary layer into transition to turbulence, which in turn enhances the total heat transfer through the fined sidewall.

Varol et al., 2007 investigated the effect of thin fin on natural convection in triangular enclosures. The enclosure was filled with porous media and an adiabatic solid vertical thin fin was placed on the bottom wall. It is observed that the thin fin can be a passive control parameter for flow field, temperature distribution and heat transfer. They reported that the addition of fin enhances heat transfer and the value of the mean Nusselt number decreases by increasing dimensionless fin height. Ridouane and Campo, 2007 also reduced the heat transfer by attaching baffles to the inclined walls of an isosceles triangular shaped enclosure.

The effect of thermally conducted fin on natural convection in triangular enclosure filled with porous media is again investigated by Varol et al., 2008. They showed that thermal conductivity of the fin attached horizontally to the vertical wall does not have any significant effect on natural convection, however, presence of fin does changes the flow fields and temperature distributions. It was also observed that the heat transfer decreases with the increasing fin length as well as distance of the fin position.

Recently, Anderson et al., 2009 used an adiabatic baffle mounted vertically downward from the apex of an attic shaped enclosure. One of the inclined walls was considered as heated while the other inclined wall and base were assumed as cold. In their study, it was found that the use of a single adiabatic baffle mounted vertically downward from the apex would alter the flow such that the convective heat loses were suppressed. It was also observed that the convective heat transfer was reduced as the length of the baffle was increased. Most recently, Anderson et al., 2010 investigated experimentally by using thick polystyrene baffle; firstly mounting from the apex of the enclosure downwards and secondly from the centre of the base upwards. From their study, it was also found that increasing baffle length mounted, either from the apex down or the base up, changes the flow pattern which in turn suppress the heat transfer by the natural convection.

In this study, convective thermal boundary layer adjacent to the heated inclined wall of a right angled triangle with an adiabatic fin mounted from that wall is investigated by numerical simulations. The governing N-S and the energy equations are solved numerically for different Rayleigh number, *Ra*, in the range of 10^5–10^8 keeping aspect ratio, $A = 1.0$, and Prandtl number, Pr = 0.71, fixed. The development of the boundary layer along the inclined heated wall is investigated. The effect of *Ra* on the heat transfer is also investigated. More attention has been given to the boundary layer development near the fin area.

2. Problem Formulations

The physical system is sketched in Figure 1, which is an air filled right angled triangular enclosure. H is the height of the enclosure and L is the length of the base. T_c and T_h are the cold and hot temperature applied to the base and inclined wall respectively.

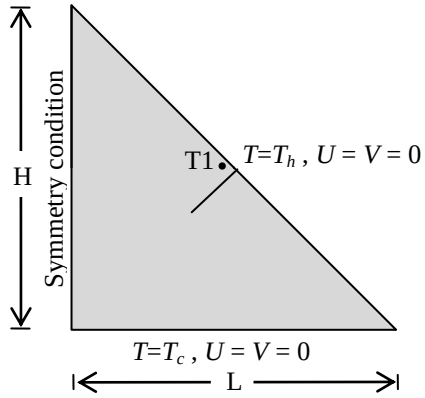

Figure 1: A schematic of the geometry and boundary conditions.

The development of natural convection inside a triangular enclosure is governed by the following non-dimensional Navier–Stokes and energy equations with the Boussinesq approximation:

$$\frac{\partial u}{\partial x}+\frac{\partial v}{\partial y}=0 \tag{1}$$

$$\frac{\partial u}{\partial \tau}+u\frac{\partial u}{\partial x}+v\frac{\partial u}{\partial y}=-\frac{\partial p}{\partial x}+\Pr\left(\frac{\partial^2 u}{\partial x^2}+\frac{\partial^2 u}{\partial y^2}\right) \tag{2}$$

$$\frac{\partial v}{\partial \tau}+u\frac{\partial v}{\partial x}+v\frac{\partial v}{\partial y}=-\frac{\partial p}{\partial x}+\Pr\left(\frac{\partial^2 v}{\partial x^2}+\frac{\partial^2 v}{\partial y^2}\right)+\Pr Ra\theta \tag{3}$$

$$\frac{\partial \theta}{\partial \tau}+u\frac{\partial \theta}{\partial x}+v\frac{\partial \theta}{\partial y}=\left(\frac{\partial^2 \theta}{\partial x^2}+\frac{\partial^2 \theta}{\partial y^2}\right) \tag{4}$$

where x, y, u, v, θ, p and τ are non-dimensional horizontal and vertical axes, horizontal and vertical velocity components, temperature, pressure and time respectively. The above non-dimensional variables are obtained by normalizing their dimensional values with the following expressions.

$$x=\frac{X}{H},\ y=\frac{Y}{H},\ u=\frac{U}{\kappa/H},\ v=\frac{V}{\kappa/H},\ \tau=\frac{t}{H^2/\kappa},\ p=\frac{P}{\rho\kappa^2/H^2},\ \theta=\frac{T-T_c}{T_h-T_c} \tag{5}$$

Here, the three dimensionless parameters which govern the natural convection flow are the Rayleigh number (*Ra*), the Prandtl number (*Pr*) and the aspect ratio (*A*), defined as

$$Ra=\frac{g\beta(T_h-T_c)H^3}{\nu\kappa},\ \Pr=\frac{\nu}{\kappa},\ A=\frac{H}{L} \tag{6}$$

where ν, ρ, β, κ are the kinematic viscosity, density of the fluid, coefficient of thermal expansion and thermal diffusivity respectively, and g is the acceleration due to gravity.

The dimensionless boundary conditions are as follows:

$$u=v=0,\ \theta=0 \qquad \textit{along the horizontal wall} \tag{7}$$

$$u=v=0,\ \theta=1 \qquad \textit{along the inclined wall} \tag{8}$$

$$\frac{\partial u}{\partial x}=\frac{\partial v}{\partial x}=\frac{\partial \theta}{\partial x}=0 \qquad \textit{along the vertical wall} \tag{9}$$

The Nusselt number, *Nu*, which is a physical quantity to measure heat transfer, is

$$Nu=\frac{qH}{k\Delta T} \tag{10}$$

where q, k are the total convective heat flux and thermal conductivity respectively, and ΔT is the temperature difference between hot and cold wall.

3. Numerical Scheme

Equations (1)-(4) are solved along with the initial and boundary conditions using the SIMPLE scheme. The Finite Volume method has been chosen to discretize the governing equations, with the QUICK scheme approximating the advection term. The diffusion terms are discretized using central differencing with second order accuracy. A second order implicit time-marching scheme has also been used for the unsteady term. The detailed numerical procedure can be found in Saha, 2010.

To capture the thermal boundary layer adjacent to the heated inclined wall and the flow field around the fin, finer meshes are distributed near the inclined wall and around the fin compared to other regions. A total of 12367 grid nodes and time step of $1.59\text{x}10^{-7}$ are considered for all computations. We have performed grid dependency test by halving the grid size and doubling the time steps. The reported errors were in the acceptable ranges (<2%). The detailed tests and results are not presented here for brevity.

4. Results and Discussions

In Figure 2, contours of the temperature are presented at different times for $Ra = 10^8$. The figure shows that initially the boundary layer develops adjacent to the hot inclined walls of the enclosure. However, as time increases, the top of the enclosure fills gradually with hot fluid and becomes stratified, where the top portion fluid is hotter than the bottom portion.

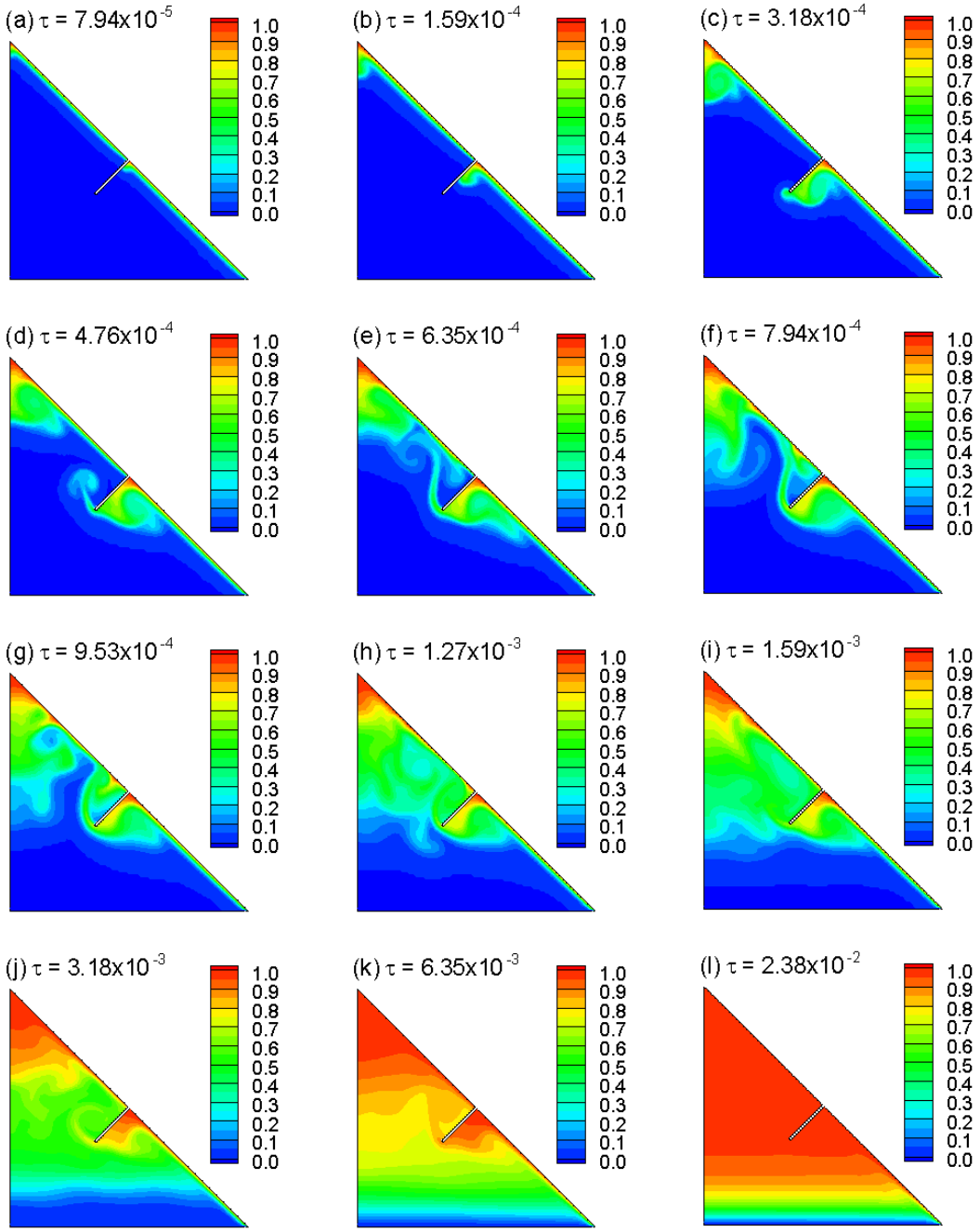

Figure 2: Temperature contours at different times for $Ra = 10^8$.

The fin mounted from the middle on the inclined wall blocks the upstream thermal boundary layer flow and causes the heated fluid to accumulate underneath the fin. As a result, a lower intrusion is formed, as seen in Figure 2(a). As time passes, the lower intrusion front moves along and toward the head of the fin due to the continuous accumulation of the heated fluid as seen in Figure 2(a-c). As soon as the lower intrusion front arrives at the end of the fin, it starts to rise vertically due to buoyant force. Figures 2(d-l) show the subsequent development of the thermal flow above the fin. It also demonstrates that, as the starting plume moves upwards, the plume becomes increasingly unstable and strikes the

downstream thermal boundary layer next to the fin as observed in Figure 2(e). The boundary layer then breaks. However, it is reattached as time passes as seen in Figure 2(j).

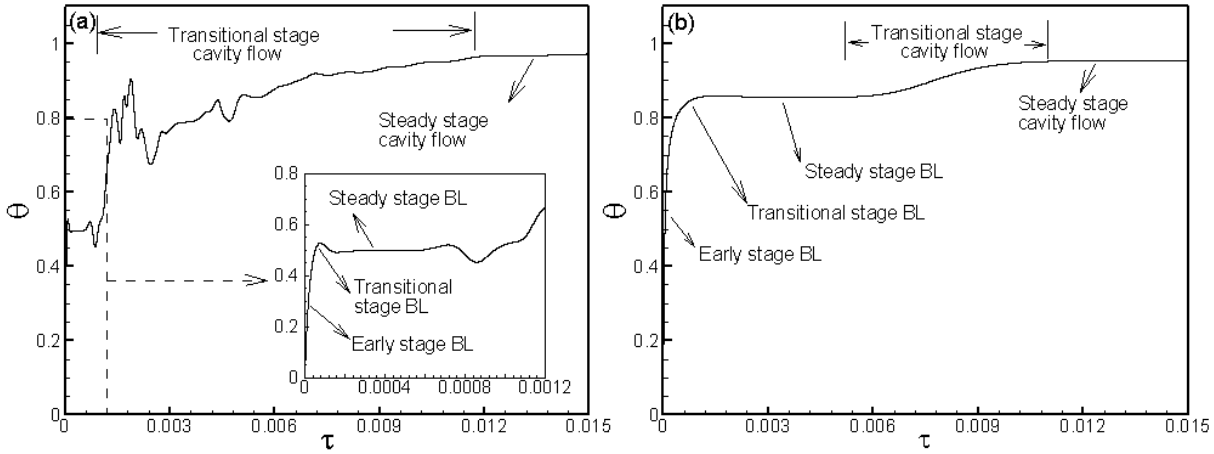

Figure 3: Time series of temperatures in the downstream boundary layer at T1(0.46394, 0.52667) for (a) Ra =10^8 and (b) Ra = 10^6.

The time series of temperature recorded at T1(0.46394, 0.52667) above the fin are shown in Figure 3 for Ra = 10^8 and 10^6. The figure shows that initially the temperature on this point is 0 which is the initial temperature of the enclosure. It is found from this figure that the air flow is dominated by two distinct stages of development, i.e. a boundary-layer development stage and the thermal stratification of the cavity. The thermal boundary layer along the inclined surface is characterized by three distinct stages, i.e. a start-up early stage, a transitional stage and a steady stage which has been shown in both Figure 3(a) and (b). Then the stratification stage starts with a transitional stage followed by a steady stage of the entire enclosure. The early stage of the boundary layer development is dominated by conduction. The stage ceases when the conduction balances convection. The transitional stage is dominated by overshoot and undershoot. At the steady stage the conduction completely balances with convection. The thermal boundary layer, which develops adjacent to the inclined wall reaches the apex of the enclosure and starts to heat the top portion as a form of thermal stratification. This process continues until the whole cavity becomes steady state.

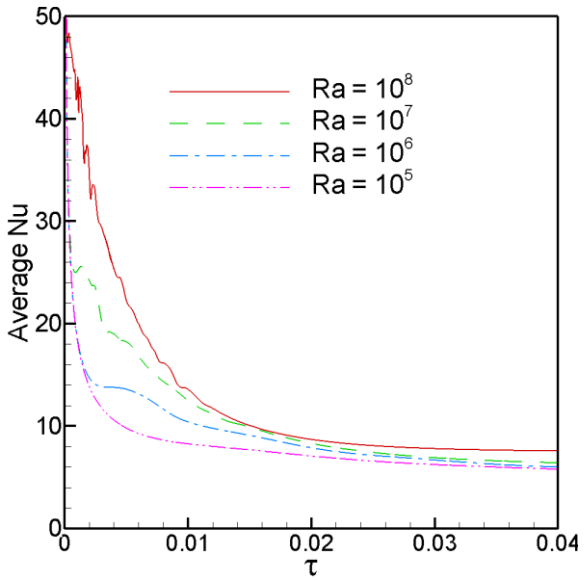

Figure 4: Time series of average Nu on the inclined surface of the enclosure for different Ra.

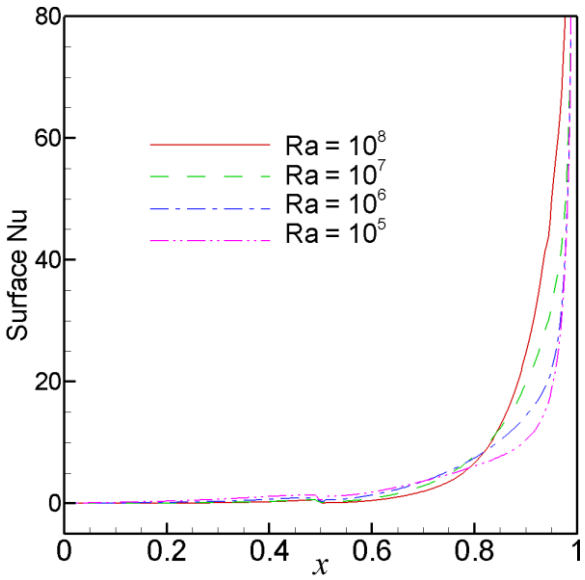

Figure 5: Surface Nu on the inclined surface of the enclosure for different Ra.

Figure 4 shows the time series of average *Nu* which have been calculated from the hot inclined wall of the enclosure for different *Ra*. The figure shows the dependency of *Nu* on *Ra*. It is seen that initially the *Nu* is very high because of the conduction effect. As the time increases, it decreases gradually and become steady state when the whole enclosure becomes

stratified. The three stages of boundary layer development can also be identified from here. For Ra = 10^8, the Nusselt number oscillates during the boundary layer development stage due to strong buoyancy effect. However, as time progress the flow becomes stratified and the oscillation disappears.

Surface *Nu* on the inclined heated wall of the enclosure for different *Ra* is presented in Figure 5. The *Nu* is almost zero on the inclined wall above the fin. This is because, due to thermal stratification the top portion of the enclosure is almost heated up (interior temperature is equal to the surface temperature). Therefore, there is no heat transfer should be expected through that surface. However, bellow the fin the heat transfer increases gradually towards the bottom tip of the enclosure. Since the bottom tip connect the bottom cold surface and inclined heated surface, the heat transfer tends to infinity at the tip due to singularity. It is also noticed that higher values of *Nu* are obtained for higher values of *Ra* because the natural convection becomes dominant to convection due to higher *Ra*.

5. Conclusion

Natural convection thermal boundary layer adjacent to the heated inclined wall of a right angled triangle with adiabatic fin mounted from that heated wall is investigated. Different *Ra* in the range of 10^5–10^8 with fixed $A = 1.0$ and Pr = 0.71 are considered in this study. The natural convective flow development is dominated by two distinct stages, i.e. a boundary-layer development stage and the thermal stratification of the cavity. It is revealed from the numerical simulations that the thermal boundary layer along the inclined surface is characterized by three distinct stages, i.e. a start-up early stage, a transitional stage and a steady stage. In presence of fin, the thermal boundary layer adjacent to the inclined wall breaks initially; then reattached with the downstream boundary layer next to the fin. Surface *Nu* increases gradually towards the tip of the heated inclined and cold bottom wall and gets its highest value at the tip due the highest temperature difference at this location. *Nu* are obtained higher for higher values of *Ra* as the natural convection becomes dominant to convection due to higher *Ra*.

References

[1] Akinsete VA and Coleman TA. Heat transfer by steady laminar free convection in triangular enclosures. Int. J. Heat Mass Transfer 1982:25(7): 991–998.
[2] Moukalled F and Acharya S. Natural convection in trapezoidal cavities with baffles mounted on the upper inclined surfaces. Numerical Heat Transfer, Part A: Applications 2000:37 (6): 545–565.
[3] Moukalled F and Acharya S. Natural convection in a trapezoidal enclosure with offset baffles. J. Thermophys. Heat Transfer 2001: 15(2): 212–218.
[4] Xu F, Patterson JC and Lei C. An experimental study of the unsteady thermal flow around a thin fin on a sidewall of a differentially heated cavity. International Journal of Heat and Fluid Flow 2008:29: 1139–1153.
[5] Xu F, Patterson JC and Lei C. Temperature oscillations in a differentially heated cavity with and without a fin on the sidewall, International Communications in Heat and Mass Transfer 2010:37: 350–359.
[6] Xu F, Patterson JC and Lei C. Transition to a periodic flow induced by a thin fin on the sidewall of a differentially heated cavity. International Journal of Heat and Mass Transfer 2009:52: 620–628.
[7] Varol Y, Oztop HF and Varol A. Effects of thin fin on natural convection in porous triangular enclosures. International Journal of Thermal Sciences 2007:46:1033–1045.
[8] Ridouane EH and Campo A, Effects of attaching baffles onto the inclined walls of attic frames for purposes of energy conservation. Heat Transfer Eng. 2007:28(2):103–111.
[9] Varol Y, Oztop HF and Pop I. Natural convection in porous media-filled triangular enclosure with a conducting thin fin on the hot vertical wall. Proc. IMechE 2008:222. Part C: J. Mechanical Engineering Science.
[10] Anderson T, Duke M and Carson J. Convection suppression in a triangular-shaped enclosure. Computational Thermal Sciences. 2009: 1:309–321.
[11] Anderson TN, Duke M and Carson JK. Suppression of natural convection heat transfer coefficients in an attic shaped enclosure. International Communications in Heat and Mass Transfer 2010: 37:984–986.
[12] Saha SC, Patterson JC and Lei C. Natural convection in attics subject to instantaneous and ramp cooling boundary conditions. Energy and Buildings 2010:42:1192–1204.

Available online at www.sciencedirect.com

SciVerse ScienceDirect

Procedia Engineering 00 (2012) 000–000

Procedia Engineering

www.elsevier.com/locate/procedia

5th BSME International Conference on Thermal Engineering

Mathematical model for a heat pump dryer for aromatic plant

Mohammed Ayub Hossain[a,*], Klaus Gottschalk[b], Mohammad Shoeb Hassan[c,*]

[a&c]*FMPE Division, Bangladesh Agricultural Research Institute, Gazipur-1701, Bangladesh*
[b]*Leibniz-Institut für Agrartechnik, Potsdam-Bornim, Max-Eyth-Allee 100, 14469 Potsdam, Germany*

Abstract

A mathematical model was developed to evaluate the performance of heat pump dryer for drying of aromatic plants. The model consists of three sub-models; namely, drying model, heat pump model, and performance model. Drying model was developed based on mass balance, heat balance, heat transfer and drying rate equations. Heat pump sub-model consists of some theoretical and empirical equations for estimating the parameters of evaporator, compressor, condenser and expansion valve. The performance sub-model was the equations for prediction of drying efficiency, COP (coefficient of performance), MER (moisture evaporating rate) and SMER (specific moisture evaporating rate). The model was validated with the experimental data. The experiments was conducted in a fixed bed drying of valerian roots (*Valeriana officinalis* L.) in cooperation with a agricultural company (Agrargenossenschaft Nöbdenitz e.G., Thüringen) in Thüringen, Germany. Data logger was used to record the temperature, relative humidity, humidity ratio and enthalpy of air at different positions of the dryer equipped with different types of sensors. The average drying air temperature was 36.84°C and relative humidity was about 20%. About 89 hours were required to reduce the moisture content of valerian roots from 89 to 9% (wb). The simulated results (temperature, relative humidity and moisture content) agreed well with the experimental results. The average COP, MER and SMER and drying efficiency were 5.45, 140.03 kg/h, 0.038 kg/kWh, and 78.23%, respectively. This model may be used for design data for heat pump dryer for drying of aromatic plants as well as other heat sensitive crops.

Keywords: Aromatic plant; heat pump dryer; heat and mass transfer; simulation; valerian root.

Nomenclature

C_p	specific heat (kJ/kgK)
C_{pv}	specific heat of water vapour (kJ/ kgK)
C_{rp}	specific heat of refrigerant at constant pressure (kJ/ kgK)
C_{rv}	specific heat of refrigerant at constant volume (kJ/ kgK)
D	diameter of tube (m)
f_r	friction factor of refrigerator
G_a	mass flow rate of air (kg/s)
H	enthalpy of refrigerant (kJ/kg)
H_a	enthalpy of air (kJ/kg)
h_c	convective heat transfer coefficient (W/m^2K)
h_{fg}	latent heat of vaporization of water vapour (W/m^2K)
h_r	rdiative heat transfer coefficient (W/m^2K)
k	thermal conductivity (kW/mK)
k_0	coefficient of drying rate (h^{-1})

* Corresponding author. Tel.: +88 2 925 2407 fax: +88 2 925 1415.
E-mail address: mahossain.fmpe@gmail.com

L	length (m)
L_p	latent heat of vaporization (kJ/kg)
M	moisture content of product (kg/kg, d.b.)
M_e	equilibrium moisture content (kg/kg, d.b.)
m_r	mass flow rate of refrigerant (kg/s)
n	polytrophic index
P	pressure (Pa)
Q	heat transfer rate (kW)
r	exponent of Page equation
t	temperature (°C/K)
u	air velocity (m/s)
W	power (kW)
w	humidity (kg/kg)
z	bed thickness (m)
Greek symbols	
α	heat transfer coefficient (kW/m^2K)
∇	change
η_d	drying efficiency of dryer
θ	drying time (s)
ρ	density (kg/m^3)
Subscripts	
a	air
c	condenser
com	compressor
d	dryer
e	external
i	internal
t	tube
r	refrigerant

1. Introduction

Drying is the removal of moisture from a product to its desired or safe moisture content. Heat is normally supplied to the product by heated air by natural means or artificially and the vapour pressure or moisture concentration gradient thus created causes the movement of moisture from inside of the product to the surface. During drying the temperature of the drying air must be kept below the recommended values depending on the intended use of the product. Excessive high temperature drying causes both physical and chemical changes ultimately deteriorate the quality of the product (Bala, 1997). There are some heat sensitive materials such as medicinal and aromatic plants, those should be dry very carefully, otherwise the medicinal and aromatic qualities will be deteriorated which are the ultimate goal of the product. To maintain the quality, these heat sensitive crops should be dried at low temperature. The problems of low temperature drying are, it takes long time and during this drying period products may deteriorate caused by microorganisms specially fungus.

Heat pump dryers have the potential to operate more efficiently, and at lower temperatures than conventional dryers. Rossi et al. (1992) made a comparison of vegetable drying by the heat pump dryer and a conventional dryer using an electrical heater and found that an energy saving of 40% and the processing time reduced by 40.7%**.** Mellmann and Fürll (2008) reported that energy costs accounted for 30 to 55% of production costs. Ziegler et al. (2009) conducted experimental study for drying of medicinal plants and spices using batch dryer coupled with heat pump. They conducted different modes of operation such as first day, heat pump drying with closed cycle system then subsequently conventional drying. They reported that in early stage of drying, primary energy consumption can be reduced by 40-55% using heat pump with internal heat recovery. Studies of heat pump dryers by computer simulation have received attention in recent years. Many theories and designs have been put forward to describe heat and mass transfer taking place in the heat pump dryer system. A simplified mathematical model of a heat pump assisted crop dryer need to be developed. The developed heat pump dryer model will be used to investigate the performance and verify its accuracy with respect to the experimental results. Prasertsan et al. (1996) developed mathematical models for heat pump dryer characteristics of four configurations, two open and two closed systems. They reported that ambient conditions and dryer efficiency played an important role in the system behaviour. Closed cycle was found more efficient than fully open cycle configuration. Phani et al. (2002a) developed simulation model for heat pump assisted drying of crops. Therefore, this study was undertaken to develop a simulation

model for heat pump drying of selected aromatic plant.

2. Mathematical Models

The mathematical model of a heat pump dryer consists of three sub-models; namely, drying model, heat pump model, and performance model. Heat and mass balance of both refrigerant and air circuits are used for development of mathematical models. The schematic view of a heat pump dryer is shown in Fig. 1.

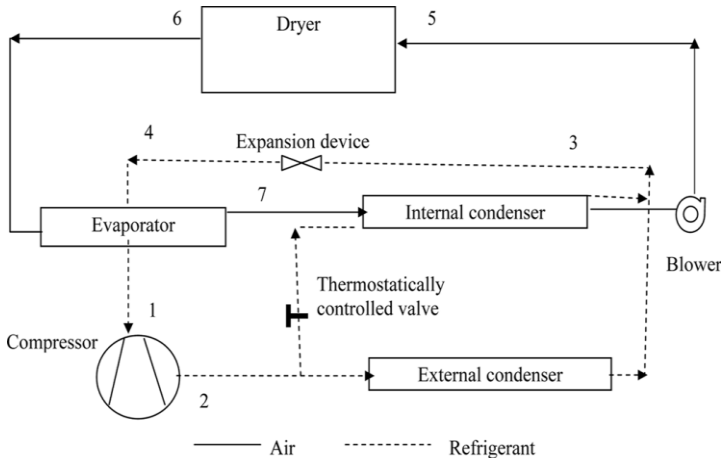

Fig. 1. Schematic view of a heat pump dryer.

2.1 Drying model

The physically-based drying model generally consists of several partial differential equations- mass balance equation, heat balance equation, heat transfer equation and drying rate equation, (Bala, 1997). This model is developed by a set of partial differential equations to describe the heat and mass transfer between drying air and product and also within a single layer of product during a small time increment. The following assumptions are made for simplification of the model.

- The air duct and drying chamber are thermally insulated
- Ambient conditions and specific heat capacity of air are constant
- The inlet air properties of a layer are the same for the outlet air of the previous layer
- Pressure of air in the system and mass flow rate of circulating dry air are constants
- Thermal equilibrium exists between the drying air and product
- The condition of air entering the evaporator is the same as that leaving the dryer and air entering the dryer is same as that leaving the condenser.

Consider an elemental layer dz of the bed (z, z + dz) of unit cross-sectional area with airflow G_a from z to z + dz (Fig. 2). There are four unknowns: changes of product moisture content, humidity, product temperature and air temperature (Hossain et al., 2010). Therefore, four differential equations are required to solve these unknowns.

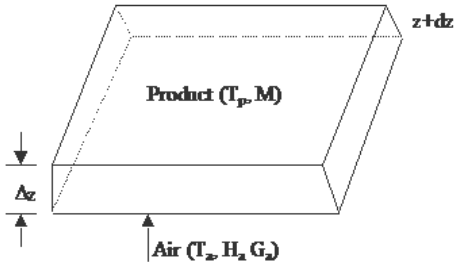

Fig. 2. Element of product (valerian roots) bed.

2.1.1 Mass balance equation

The flow of moisture into the element (z) at time dθ is $G_a w_a(z)d\theta$ and out of the element (z+dz) is $G_a w_a(z+dz)d\theta$. The moisture lost from the product in the element of bed dz at time θ is $-\rho_p M(\theta)dz$ and at time (θ + dθ) is $-\rho_p M(t + dt)dz$. The mass balance equation is therefore given by:

Moisture lost by product = moisture gained by air.

$$-\rho_p M(\theta+d\theta)dz-(-\rho_p M(\theta)dz)=G_a w_a(z+dz)d\theta-G_a w_a(z)d\theta \quad (1)$$

Using Taylor series expansion for w_a and M and ignoring all terms of dz^2 and $d\theta^2$ and higher, Equation (1) reduces to

$$G_a\left(\frac{\partial w_a}{\partial z}\right)dzd\theta=-\rho_p\left(\frac{\partial M}{\partial t}\right)dzd\theta \quad (2)$$

Therefore, the change of humidity in the finite difference form, the Equation (2) becomes as

$$\Delta w_a=-\left(\frac{\rho_p}{G_a}\right)\left(\frac{\Delta M}{\Delta\theta}\right)\Delta z \quad (3)$$

2.1.2 Heat balance equation

Heat balance equation of the drying element (layer) is the change in enthalpy of air equal to change in enthalpy of product. Therefore, change of enthalpy of air of element (z, z+dz) at time dθ is:

$$G_a[C_{pa}+C_{pw}w_a(z+dz)t_a(z+dz)+L_a w_a(z+dz)]d\theta-G_a[C_{pa}+C_{pw}w_a(z)t_a(z)+L_a w_a(z)]d\theta \quad (4)$$

Again, change of enthalpy of product at time (θ+dθ) and θ is:

$$-\rho_p[C_{pp}+C_{pl}M(\theta+d\theta)t_p(\theta+d\theta]dz+\rho_p[C_{pp}+C_{pl}M(\theta)t_p(\theta)]dz \quad (5)$$

Applying the Taylor series expansion and neglecting second order and higher terms, expressions (4) and (5) are equated to and change of air temperature in the finite difference form as:

$$\Delta t_a=\frac{-\frac{\rho_p}{G_a}\Delta t_p[C_{pp}+C_{pl}(M+\Delta M)](\frac{\Delta z}{\Delta\theta})+\frac{\rho_p}{G_a}\Delta M(C_{pw}t_a+L_a-C_{pl}t_p)(\frac{\Delta z}{\Delta\theta})}{C_{pa}+C_{pw}w_a-\frac{C_{pw}\rho_p}{G_a}\Delta z(\frac{\Delta M}{\Delta\theta})} \quad (6)$$

2.1.3 Heat transfer rate equation

Heat transfer between air and product = change in sensible heat of product + change in enthalpy in air just after drying and just prior to drying (evaporation). Therefore, the expression can be written mathematically as:

$$h_{cv}(t_a-t_p)dzd\theta=\rho_p[C_{pp}t_p(\theta)+C_{pl}Mt_p(\theta)+(C_{pw}+L_p)M(\theta)dzd\theta-C_{pl}M(\theta)t_p)]dz \quad (7)$$

Applying the Taylor series expansion and neglecting the second and higher order terms Equation (7) becomes in the finite difference form and after simplification, the change of product temperature becomes

$$\Delta t_p=\frac{2(t_a-t_p)+\Delta t_a+\frac{2\rho_a}{h_{cv}}(C_{pw}+L_p-C_{pl}t_p)\frac{\Delta M}{\Delta\theta}}{1+\frac{\rho_p}{h_{cv}\Delta\theta}(C_{pp}+C_{pl}M)} \quad (8)$$

2.1.4 Drying rate equation

The rate of change of moisture content of a thin layer product inside the dryer can be expressed by an appropriate thin layer drying equation. No thin layer drying equation was available in the literature for drying of valerian (*Valeriana officinalis* L.) roots. Asparagus (*Asparagus racemosus* Wild.) root is similar in nature and widely used as medicinal purposes. The Page equation was found suitable to predict moisture content of asparagus root in thin layer (Bala et al., 2010). The Page equation is as follows.

$$\frac{M - M_e}{M_o - M_e} = \exp(-k_p t_p^r) \tag{9}$$

The Page equation in differential form is

$$\frac{dM}{dt} = -k_p r \left(\frac{M - M_e}{M_0 - M_e} \right) \theta^{r-1} \tag{10}$$

Taking the mean value of M and (M+ΔM) the Equation (10) in the finite difference form can be expressed as (Hossain et al., 2005).

$$\Delta M = -k_p n.\Delta\theta (M - M_e)(X + \Delta\theta)^{r-1} \tag{11}$$

Where, $X = \left[\frac{-\ln\left(\frac{M - M_e}{M_0 - M_e} \right)}{k_p} \right]^{\frac{1}{r}}$

The values of k and r may the obtained in terms of drying air temperature from the work of (Bala et al., 2010).

2.2 Heat pump model

The heat pump is a complex device with continuous changing air and refrigerant properties during operation. To make the model simpler, the following assumptions are made.

- The refrigerant at outlet of evaporator and condenser are saturated vapour and saturated liquid, respectively
- The compression and the expansion of the refrigerant are isentropic and isenthalpic processes, respectively
- The tubes connecting the heat pump components are insulated and the pressure drop in the pipe system is negligible
- The wall of the component housing is adiabatic
- Heat pump is operated at steady-state.

2.2.1 Evaporator model

The rate of moisture condensed or removal at the evaporator surface can be computed using the following equation.

For ideal condition:

$$m_{ew} = m_a (w_{do} - w_{es}) \tag{12}$$

In an evaporating coil, all the airs are not cooled due to not coming in contact with the cooling coil. The value of bf (bypass factor) for an efficient process at the evaporator should be in the range of 0.10-0.15 (Phani et al., 2002b).

$$m_{ew} = m_a (1 - bf)(w_{do} - w_{es}) \tag{13}$$

Now, the energy transfer between the refrigerant air at the evaporator is given by the following equation.

$$Q_e = m_r (H_1 - H_4) = m_a C_{pa} (t_{ei} - t_{eo}) \tag{14}$$

Where, H_1=saturated vapour enthalpy (H_v) and H_3=liquid enthalpy (H_l). Therefore H_1 and H_3 can be obtained from the

following empirical equations (Singh and Heldman, 2009).

$$H_1 = H_v = a_8 + a_9 T_{re} + a_{10} T_{re}^2 + a_{11} T_{re}^3 + a_{12} \quad (15)$$

$$H_3 = H_l = a_4 + a_5 T_{rc} + a_6 T_{rc}^2 + a_7 T_{rc}^3 \quad (16)$$

The forced convection heat transfer coefficient on the air side of a flat-finned tube coil is calculated by the correlation proposed by Rich (1973).

2.2.2 Compressor model

A mathematical model of a reciprocating compressor is used to predict the change in enthalpy of refrigerant during compression and energy consumption. The main parameters of compressor are volumetric efficiency (η_v), refrigerant mass flow rate (m_r) and compression power (W_{com}). These can be calculated using the following equations.

$$\eta_v = 1 + n - n\left(\frac{P_2}{P_1}\right)^{\frac{1}{n}} \quad (17)$$

$$W_{com} = m_r (H_2 - H_1) \quad (18)$$

$$H_2 = H_1 + \nabla H \quad (19)$$

∇H can be obtained from the following equation (Singh and Heldman, 2009).

$$\nabla H = \frac{P_1 v_{rl}}{3600}\left(\frac{n}{n-1}\right)\left\{\left(\frac{P_2}{P_1}\right)^{(n-\frac{1}{n})} - 1\right\} \quad (20)$$

Here, n is the ratio of specific heat of refrigerant at constant pressure (C_{rp}) and specific heat at constant volume (C_{rv}) i.e. $n = \frac{C_{rp}}{C_{rv}}$.

2.2.3 Condenser model

The condenser model is used to predict the energy transfer and mass flow rate of refrigerant in the condenser coil. Generally, two condensers are used as heat exchanger-internal and external (Fig. 1). The rejected heat by the external condenser can be computed using following equation.

$$Q_{ce} = m_r (H_2 - H_3) \quad (21)$$

The heating load of internal condenser may be calculated using the following equation. The condenser model is used to calculate the energy transfer and mass flow rate of refrigerant in the condenser coil.

$$Q_{ci} = m_a (C_{pa} + w_{di} C_{pv})(t_{co} - t_{eo}) \quad (22)$$

Heating load in the external condenser (Q_{ce}) may be computed from the following equation

$$Q_c = Q_{ci} + Q_{ce} \quad (23)$$

Heat transfer coefficients of the refrigerant side of the condenser for single phase are calculated as (ASHRAE, 1997).

2.2.4 Expansion valve model

In this model, capillary tube is used as the expansion device for pressure reduction. The expansion process is assumed

to be isenthalpic, i.e.

$$H_4 = H_3 \tag{24}$$

The frictional pressure drop and friction factor of each part is calculated and the required length of capillary tube is determined using the following equations (ASHRAE, 1997).

$$\nabla P_r = \frac{\rho_r f_r \nabla L u_r^2}{2D} \tag{25}$$

2.3 Performance model

The drying and dehumidification performance of the heat pump dryer are evaluated by the drying efficiency of the dryer (η_d), coefficient of performance of the heat pump (COP), moisture extraction rate (MER) and specific moisture extraction rate (SMER). These may be computed using the following equations (Pal and Khan, 2008).

$$\eta_d = \frac{t_{di} - t_{do}}{t_{di} - t_w} \tag{26}$$

$$COP = \frac{Q_{con}}{W_{com}} = \frac{H_2 - H_3}{H_2 - H_1} \tag{27}$$

$$MER = \frac{m_w}{\theta} \tag{28}$$

$$SMER = \frac{m_w}{W_{Com} + E_b} \tag{29}$$

2.4 Solution procedure

The drying chamber was vertically divided into a number of sections (trays) ($L=j.\Delta x$) along the direction of air flow in the dryer. The drying time was also splitted into a number of intervals ($\theta = i.\Delta\theta$). Using k and r values, the changes of moisture content of valerian roots for time interval, ΔM was calculated from equation (11). The change in air humidity was computed using equation (3). The drying air temperature and product temperature was computed using equation (6) and equation (8) respectively. This process would be repeated section by section until the end of the section was reached. This process would be then repeated for each time increment.

The saturated vapour enthalpy and liquid enthalpy was obtained from equations (15) and (16), respectively. The energy transfer between refrigerant and air was determined using equation (14). The value of H_2 was determined using equation (19). Q_{ce} and Q_{ci} was computed from equations (21) and (22), respectively. Then Q_c was determined using equation (23). Then the pressure drop was computed from equation (25). Now, the dryer efficiency (η_d), COP, MER and SMER were calculated using equations (26), (27), (28), and (29), respectively. The whole solution process was solved using the Qbasic computer program.

2.5 Experimental procedure

The experiments was conducted to fixed bed drying of valerian roots (*Valeriana officinalis* L.) in cooperation with a large agricultural company (Agrargenossenschaft Nöbdenitz e.G., Thüringen) in Thüringen, Germany. Before starting an experimental run, the whole apparatus was operated for several hours. The fresh and washed valerian roots were loaded in the drying chamber at a thickness of about 250 mm. Loading and unloading was done by a crane. Data logger (Model: ALMENO, Ahlborn Mess-und Regelungstechnik GmbH, Germany) was used to record the temperature, relative humidity, humidity ratio and enthalpy of air at different positions of the dryer using equipped with different types of sensors. The data was recorded at one minute interval. Different types of sensors were set at inlet and outlet points of drying chamber, evaporator, condenser and auxiliary heater. The air conditions of ambient air were also recorded simultaneously. The initial and final moisture content of valerian roots were determined by gravimetric method.

3. Results and Discussion

Simulated and measured air temperature in dryer during drying of valerian roots is shown Fig. 3. The total drying time was about 89 hours. The average, maximum and minimum ambient temperature was 4.05, 12.19 and -4.67°C, respectively. Average dryer inlet temperature was 34.80°C. The maximum drying inlet temperature (39.92°C) was below the optimum drying air temperature (40°C) for valerian roots. So, there was no possibility for quality deterioration of valerian roots during drying. Sometimes, the measured temperature fluctuations were observed. These might be due to that at that time the door of the drying chamber was remained open and temperature felled down. The average simulated temperature (34.92°C) was very close to the average measured temperature (34.80°C). There was no significant difference between measured and simulated temperatures ($p \leq 0.00023$) by t-test. So, the simulated temperature in the dryer agreed well with the measured temperature.

Simulated and measured outlet temperatures of evaporator and condenser during drying of valerian roots are given in Fig. 4. The average measured (40.89^{o}C) and simulated (40.10^{o}C) condenser temperature was found very close to each other and there was no significant difference between them by t-test ($p \leq 0.000364$). But the measured condenser temperature was found to fluctuate with the drying time. This may be due to that the door of condenser opened several times for adjusting. Similar result was observed for evaporator ($p \leq 0.10065$) outlet measured and simulated temperatures.

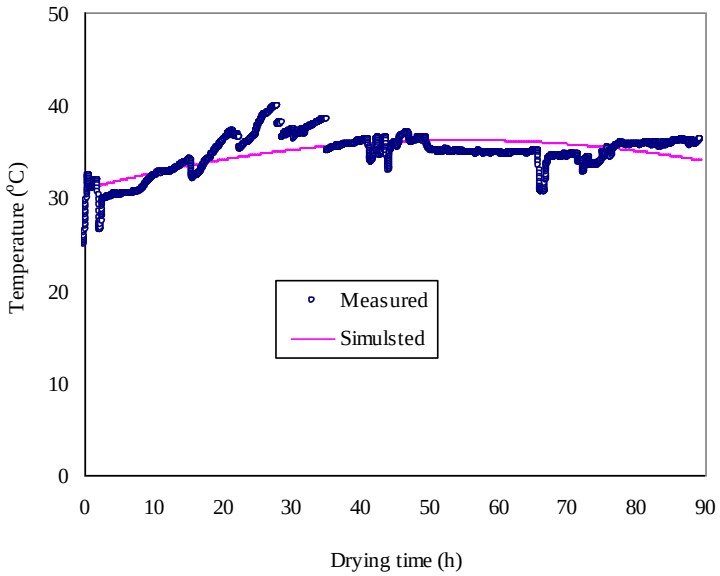

Fig. 3. Simulated and measured air temperature in dryer during drying of valerian roots.

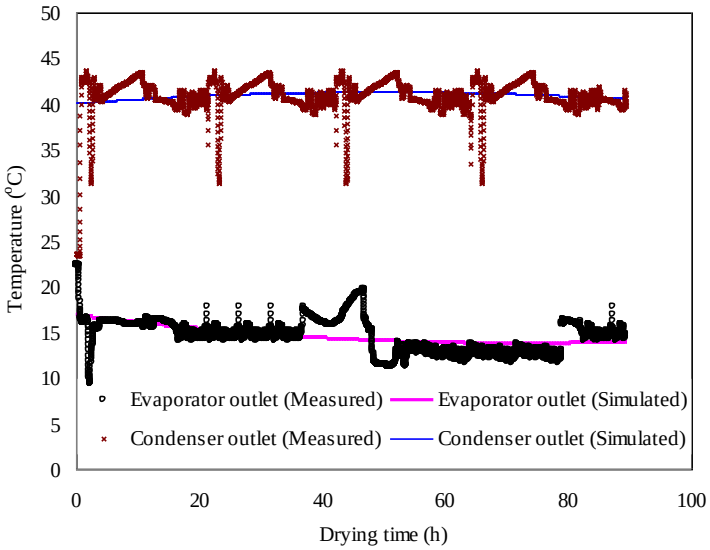

Fig. 4. Simulated and measured outlet temperature of evaporator and condenser during drying of valerian roots.

Simulated and measured inlet and outlet relative humidity in the dryer during drying of valerian roots are shown in Fig. 5. The difference of dryer inlet and outlet measured and simulated relative humidity ($p \leq 0.0256$) was found statistically insignificant. The outlet measured relative humidity ($p \leq 0.0219$) was found to fluctuate during drying period. This may be due to that inversion of valerian roots were carried out several times for better and uniform drying. But reasonable good agreement was found for measured and simulated relative humidity for both inlet and outlet air.

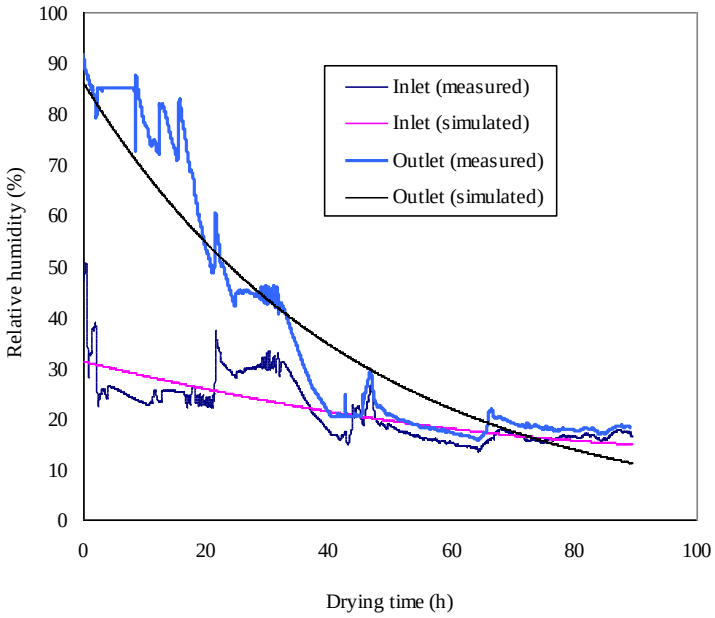

Fig. 5. Simulated and measured inlet and outlet relative humidity in the dryer during drying of valerian roots.

Simulated enthalpies of air in the compressor, condenser, evaporator, and dryer during drying of valerian roots are shown in Fig. 6. Average enthalpy of air in the compressor was found the highest (63.07 kJ/kg) followed by evaporator (46.91 kJ/kg) and dryer (28.26 kJ/kg). The average lowest enthalpy (23.55 kJ/kg) was found in the condenser. All the simulated enthalpy lines followed the similar pattern during drying period.

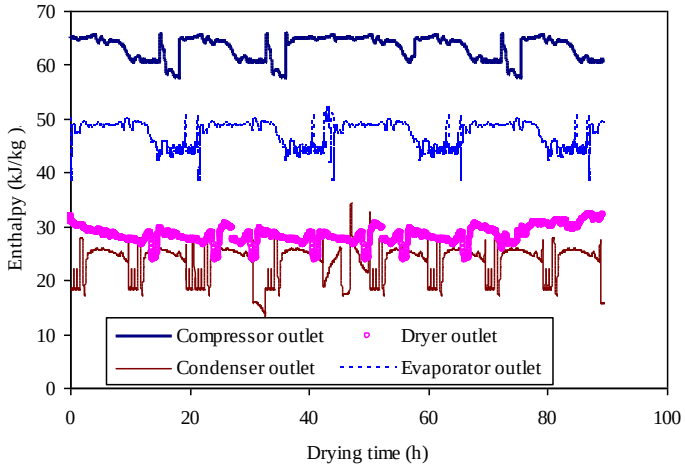

Fig. 6. Simulated enthalpy of air in the compressor, condenser, evaporator, and dryer during drying of valerian roots.

Variation of measured and simulated moisture content of valerian roots with drying time is shown in Fig. 7. Drying curves followed the exponential trend. There were some fluctuations in moisture content due to the fluctuations of drying air temperatures. The initial moisture content of valerian roots was 6.00 kg/kg dry basis (86%, wet basis) and dried to 0.10 kg/kg dry basis (9%, wet basis). There was no significant difference between measured and simulated moisture contents by

t-test ($p \leq 0.01222$). Therefore, the simulation agreed well with the measured moisture content of valerian roots during drying.

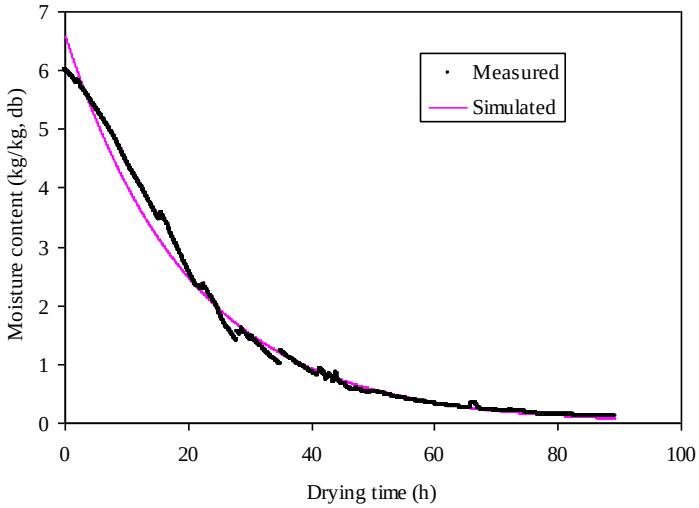

Fig. 7. Measured and simulated moisture content of valerian roots during drying.

The average MER (moisture evaporating rate) and SMER (specific moisture evaporating rate), COP (coefficient of performance), and drying efficiency are given in Table 1. The average MER and SMER were found to be 140.03 kg/h and 0.038 kg/kWh, respectively. The average COP was 5.45. It is noted that the COP of industrial dryer should not below 5. The drying efficiency was found to be 78.23%.

Table 1. Performance parameters of heat pump dryer during drying of valerian roots

Performance parameters	Average value
MER (kg/h)	140.03
SMER (kg/kWh)	0.038
COP	5.45
Drying efficiency (%)	78.23

4. Conclusion

The average drying air temperature was 36.84°C and relative humidity was about 20%. About 89 hours were required to reduce the moisture content of valerian roots from 89 to 9% (wb). The simulated results (temperature, relative humidity and moisture content) agreed well with the experimental results. The average COP, MER, SMER and drying efficiency were 5.45, 140.03 kg/h, 0.038 kg/kWh, and 78.23%, respectively. This model may be used for design data for heat pump dryer for drying of aromatic plants as well as other heat sensitive crops.

Acknowledgement

This research was carried out with the financial assistance of Alexander von Humboldt Foundation, Germany and physical support provided by Leibniz Institut für Agrartechnik Potsdam-Bornim, Germany. The authors are very thankful to them.

References

[1] Bala B K. Drying and Storage of Cereal Grains. New Delhi: Oxford and IBH Publishing Co. Pvt. Ltd.;1997.

[2] Rossi S J, Neves L C, Kieckbusch T G. Thermodynamic and energetic evaluation of heat pump applied to the drying of vegetable. Proceedings 8th International Drying Symposium (IDS92), Montreal, Canada, August 2-5, 1992; pp. 1475-1484.

[3] Mellmann J, Fürll C. Trocknungsanlagen für Arznei- und Gewürzpflanzen – spezifischer Energieverbrauch und Optimierungspotenzial (Drying facilities for medicinal and aromatic plants–specific energy consumption and potential for optimisation). Zeitschrift für Arznei- und Gewürzpflanzen 2008;13(3):127-133.

[4] Ziegler Th, Niebling F, Teodorov T, Mellmann J. Wärmepumpentrocknung von Arznei- und Gewürzpflanzen –

Möglichkeiten zur Steigerung der Energieeffizienz/ Heat pump drying of medicinal and spice plants – possibilities of energy efficiency enhancement. Zeitschrift für Arznei- und Gewürzpflanzen 2009; 14(4):160-166.

[5] Prasertsan;, S, Saen-Saby P, Ngamsritrakul, P, Prateepchaikul G. Heat pump dryer Part 1: Simulation of the models. International Journal of Energy Research 1996; 20: 1067-1079.

[6] Phani K A, Greg J S, Sokhansanj S. Performance study of a heat pump dryer system for specialty crops- Part 1: Development of a simulation model. International Journal of Energy Research 2002a; 26: 1001-1019.

[7] Hossain M A, Gottschaslk K, Amer, B M A. Mathematical modeling for drying of tomato in hybrid dryer. The Arabian Journal for Science and Engineering 2010; 35(2B): 239-262.

[8] Bala B K, Hoque M A, Hossain M A, Uddin M B. Drying characteristics of asparagus roots (*Asparagus racemosus* Wild.). Drying Technology 2010; 28: 533-541.

[9] Hossain M A, Woods J L, Bala B K. Simulation of solar drying of chilli in solar tunnel drier. International Journal of Sustainable Energy 2005; 24(3): 143-153.

[10] Phani K A, Sokhansanj S, Schoenau G J S. Performance study of a re-circulating cabinet dryer using a household dehumidifier. Drying Technology 2002b; 20(8): 1673-1689.

[11] Singh R P, Heldman D R. Introduction to Food Engineering. Fourth Edition. Academic Press, An imprint of Elsevier; 2009.

[12] Rich D G. The effect of fin spacing on the heat transfer and friction performance of multi-row, smooth plate fin-and-tube heat exchangers. ASHRAE Transactions 1973; 79(1): 137-145.

[13] ASHRAE. ASHRAE Handbook: Fundamentals. American Society of Heating, Refrigerating and Air- Conditioning Engineers. Inc. 1791 Tullie Circle, N. E., Atlanta, GA 30329; 1997.

[14] Pal U S, Khan M K. Calculation steps for the design of different components of heat pump dryers under constant drying rate condition. Drying Technology 2008; 26(7): 864-872.

Available online at www.sciencedirect.com

SciVerse ScienceDirect

Procedia Engineering 00 (2012) 000–000

Procedia Engineering

www.elsevier.com/locate/procedia

5th BSME International Conference on Thermal Engineering

Large Eddy Simulation of the Flow-Field Around a Full- Scale Heavy-Duty Truck

Prasanjit Das[a,*], Makoto Tsubokura[a], Tomofuyu Matsuuki[b], Nobuyuki Oshima[a], Kozo Kitoh[c]

[a]*Graduate School of Engineering, Hokkaido University, Sapporo, Hokkaido, 060-8628, Japan*
[b]*Isuzu Advanced Engineering Center Ltd., Japan*
[c]*Kozo Kitoh Technology Inc., Shibuya-ku, Tokyo, 150-0012, Japan*

Abstract

In this paper, Large Eddy Simulations (LES) of flow field around two different full-scale heavy-duty truck with air deflector and without an air deflector model are presented. The full-scale truck model is considered which contains a number of details such as bumpers, underbody, tractor chassis, wheels and axles. The numerical simulations have been conducted with two virtual wind tunnels at different yaw angle at 0°, 5° and 10°. The models are placed at different yawing angles in the virtual wind tunnels with a blockage ratio of about 10%, which is same as the experimental wind tunnel. To compare the corrected experimental results with the ideal case, other simulations are also conducted with a larger cross section at the blockage ratio of about 1%. A detailed survey of both instantaneous and time-averaged flow is presented. The steady state simulations with tetrahedral meshes predict the drag coefficient (C_d) accurately within 3.3%, 4.5% and 3.3% of with air deflector model and 1.3%, 4.1% and 7% of without an air deflector model to corresponding experimental values at 0^o, 5^o and 10^o yaw cases, respectively. It is observed that aerodynamic coefficients such as drag coefficient (C_d), side force coefficient (C_s) and lift force coefficient (C_l) depend on yaw angles and as well as vehicle geometry.

Keywords: Heavy-duty truck, aerodynamic coefficients, flow structure, LES

Nomenclature

$\bar{u}$	spatially filtered velocity	$C_{D_{uw}}$	measured drag coefficient
$\bar{P}$	spatially filtered pressure	ν	kinematic viscosity (m^2/s)
p	pressure (Pa)	K	empirical factor
$\bar{S}_{ij}$	spatially filtered strain tensor	S	vehicle frontal area (m^2)
C_s	model coefficient	C	wind tunnel test-section area (m^2)
f_d	damping function		
q_c	corrected dynamic pressure (N/m^2)	*Subcripts*	
q	measured dynamic pressure (N/m^2)	i, j	coordinates in i-th and j-th direction
C_D	corrected drag coefficient	*SGS*	subgrid- scale

Current affiliation:* Corresponding author
Chittagong University of Engineering and Technology (CUET)
Tel.031-714920-2/fax: +880-31-714910
E-mail address: prasanjit@cuet.ac.bd, prasanjitd11@yahoo.com

1. Introduction

Large heavy-duty trucks are major commercial transporting vehicle for goods all over the world. From the aerodynamic point of view, large trucks are bluff bodies in a high speed flow subjected to enormous drag forces. It is estimated that a typical heavy truck vehicle with an average drag coefficient (C_d) of 0.6 and driving at 70 miles per hour spends 65% of its fuel overcoming aerodynamic drag [1-4]. For this reason, drag remains the focal point of vehicle aerodynamics because reducing aerodynamic drag contributes significantly to fuel economy and emissions reduction. Generally, it is found that drag coefficient of truck might be reduced by 50% by a variety of means [2]. Reduced the fuel consumption for heavy truck vehicle can be achieved by a number of devices and strategies. Boat-tails, air deflector and pneumatic suction/blowing equipment are examples of such devices [5]. It is crucially important to have a sound understanding of the flow-field around a truck and in its wake in order to develop and test such drag reduction devices.

The accuracy of drag coefficients reported by various groups of researchers was achieved only through a costly and tedious process of preparing a full-scale model and then conducting test on it. Although actual full-scale automotive vehicles can be tested, the realism of such simulations is limited by the finite size of the test section, the complexities of the moving ground rigs, and the inadequacy of testing under ever changing wind conditions. Moreover, the results for scale model tests are subjected to numerous doubts associated with the effect of the Reynolds number, the fidelity of the model, the absence of the engine cooling and passenger compartment flows, the lack of under hood and under body details, the effect of flow-intrusive probes [5-6].

To surmount some of the difficulties associated with wind tunnel testing and on-road measurement, wind tunnel experts and researchers have invented computerized simulation techniques. With the advent of powerful computational resources and efficient algorithms, computational fluid dynamics (CFD) is being used increasingly to provide detailed insight into the flow structure around vehicles. However, CFD still faces the challenge of predicting truck drag coefficients with accuracy and repeatability. This challenge has its root in the highly turbulent flow-field around the truck, especially in its wake was reported by Ashok et al., [7]. Recent advances in high-performance computing techniques have reduced the cost and time of CFD analysis considerably.

The purpose of the present study is investigated the effects of yaw angle and add-on device air deflector on aerodynamic coefficients (drag coefficient and side force coefficient and lift force coefficient) and as well as flow-field around a full-scale heavy-duty truck in a closed wall wind tunnel. The effects are investigated for two different truck models (with and without an air deflector) at yaw angles of 0°, 5° and 10° respectively. To validate the Large Eddy Simulation (LES), turbulence model is used and compared its results with those for the actual vehicle in the DNW-German Dutch wind tunnel. To simulate the unconstrained free-stream conditions, a larger virtual rectangular wind tunnel is simulated with a blockage ratio of about 1%.

1.1. Numerical methods

An incompressible Newtonian fluid has been assumed, and continuity and momentum equations are spatially filtered to obtain the governing equations of LES:

$$\frac{\partial \overline{u}_i}{\partial x_i} = 0 \tag{1}$$

$$\frac{\partial \overline{u}_i}{\partial t} + \frac{\partial}{\partial x_j}\overline{u}_i\overline{u}_j = -\frac{\partial \overline{P}}{\partial x_i} + 2\frac{\partial}{\partial x_j}\left(\nu + \nu_{SGS}\right)\overline{S}_{ij} \tag{2}$$

The bar over the physical quantity indicates the spatial filtering operation for LES. The filtered strain rate tensor $\overline{S}_{ij}$ and pressure $\overline{P}$ in Eq. (2) are expressed as

$$\overline{S}_{ij} = \frac{1}{2}\left(\frac{\partial \overline{u}_j}{\partial x_i} + \frac{\partial \overline{u}_i}{\partial x_j}\right) \tag{3}$$

$$\overline{P} = \overline{p}/\rho + \left(\overline{u_i u_j} - \overline{u}_i\overline{u}_j\right)/3 \tag{4}$$

In Eq. (2), the last term on the right represents the effect of subgrid-scale (SGS) turbulence, which is modelled under the eddy viscosity assumption. The conventional Smagorinsky model [8] has been used, and the eddy viscosity coefficient is modeled as

$$\nu_{SGS} = \left(C_s f_d \Delta\right)^2 \sqrt{2\bar{S}_{ij}\bar{S}_{ij}} \tag{5}$$

where Δ is the length scale of the SGS turbulence expressed as the cube root of each numerical mesh, and model coefficient C_s is set to 0.15, which is generally suitable for external flows. The damping of the turbulent effect near a wall boundary is explained by the Van-Driest type damping function as follows:

$$f_d = 1 - \exp\left(\frac{-l^+}{25}\right) \tag{6}$$

where l^+ is the distance from the wall in wall coordinates.

The governing equations were discretized by using the vertex-centered unstructured finite volume method. The second-order central differencing scheme was applied for the spatial derivatives and blending of 5% first-order upwind scheme for the convection term was employed for numerical stability. The third-order upwind scheme was adopted for the spatial derivative far away from vehicle, where coarser grid was allocated. For time marching, the third-order Adams-Moulton semi-implicit scheme was used. Pressure-velocity coupling was preserved by using the Simplified Marker and Cell (SMAC) algorithm. The pressure Poission equation was solved by the incomplete Cholesky conjugate gradient (ICCG) method.

1.2. Target vehicle model and computational mesh

Fig 1 shows the configuration of the two different full-scale heavy-duty trucks having been developed by Isuzu Motors Limited, with its length, width, and height of 12.0, 2.5, and 3.7 meters, respectively. The geometrical shape was reproduced in detail including the engine room under the cabin together with the radiator and other small parts around the engine, the side mirrors, and the powertrain components under the body as well. The surface of the vehicle is reproduced by about 1.5 million triangle meshes. To reproduce the fine structure, the surface resolution is from 5 to 10 mm around the side mirror, and relatively fine elements are allocated around the cabin. The engine and power train are reproduced by the moderate elements with the resolution of 20 to 50 mm. Larger elements are allocated to reproduce cargo panel. The fluid space is decomposed by tetrahedral elements. To maintain finer resolution around the vehicle, hierarchical allocation is carried out, as shown in Fig 2.

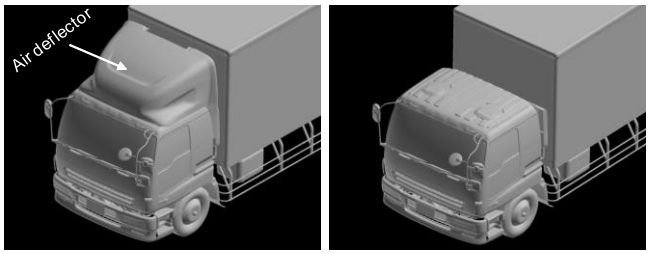

Fig. 1. Heavy-duty truck model (left: air deflector model, right: no air deflector model).

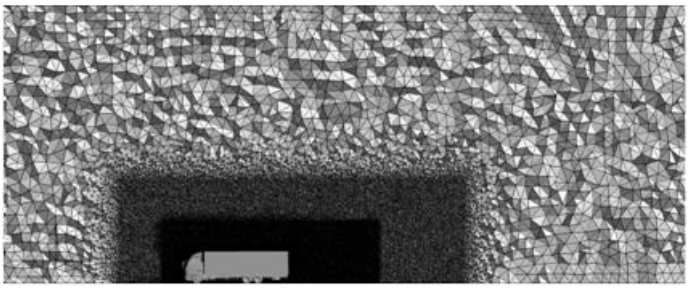

Fig. 3. Cross-sectional view of the tetra-hedral mesh.

1.3. Computational domain and boundary condition

In the computational analysis, two different virtual wind tunnels were considered. They are baseline virtual wind tunnel for which the blockage effect is to be found. The baseline virtual wind tunnel with its test section of 9.5 by 9.5 meters is shown in Fig 3(a); blockage ratio about of 10% corresponds to the DNW-German Dutch wind tunnel. In the real road condition, blockage effect does not exist. To simulate such a condition, we created a numerical domain with its test section of 32.4 by 25 meters in order to neglect blockage ratio. Hence, we termed this condition an ideal condition, which has the blockage ratio around 1%, as shown in Fig 3(b).

In both cases, a uniform velocity distribution U_0 is defined at the inlet (about 21 m/s and 25 m/s in the baseline wind tunnel and ideal cases, respectively) about 40 m upstream of the vehicle. All velocity components are gradient-free for the steamwise direction at the outlet. Solid wall condition is adopted on the surface of the vehicle and floor on which the vehicle was mounted. It is impossible to resolve the entire boundary layer at a reasonable computational cost, especially in the vicinity of the solid wall where large velocity gradient appears. The log-law profile is assumed on the velocity and surface friction on the wall is estimated and directly imposed as Neumann boundary condition. As a result of the assumed log-law profile, the first nearest grid point is allocated so as to maintain the distance from the wall less than about 200 in wall unit (y+), which are located within the logarithmic layer of the boundary layer.

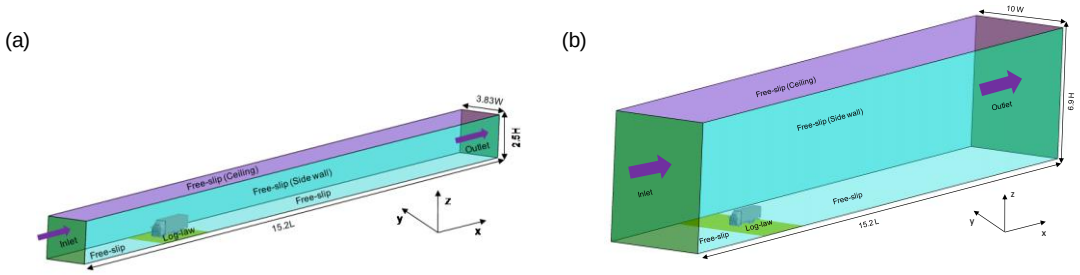

Fig. 3. Computational domain (a) baseline condition (blockage ratio: 10%) and (b) ideal condition (blockage ratio: 1%).

2. Results and Discussion

In the following sections the flow structure around the truck body and in its wake are described. Static pressure, velocity, and vorticity distributions at various locations around the vehicle are presented and discussed. Also, it is reported the aerodynamics coefficients (drag, side force and lift force coefficients) measured in the CFD simulations and compared them with corresponding experimental measurements.

2.1. Front-end and rear-end flow

Fig 4 shows time-averaged static pressure and velocity magnitude distribution around the vehicle at an arbitrary time instant. In air deflector model, flow around the frontal area of the vehicle is relatively more steady than no air deflector model. The airflow above the cabin of a truck without an air deflector is perturbed by the strong separation at the front the trailer, and the separated flow is substantially affected by the yaw condition. The flow around the front area of the vehicle is relatively steady while that to the rear is quite unsteady and large vortex shedding is evident.

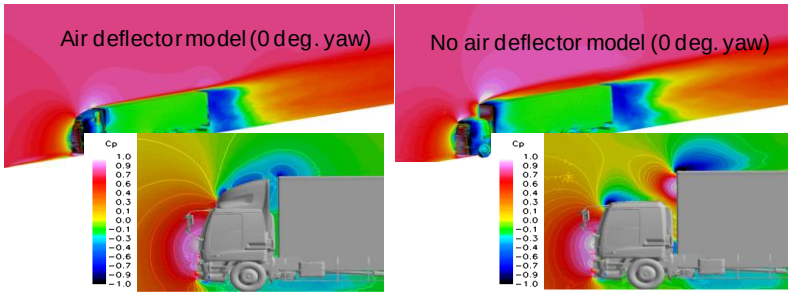

Fig. 4. Contours of velocity magnitude on the symmetry plane and contours of static pressure on the vehicle body (upper figure) and contours of static pressure along the symmetry plane (below figure).

The effective drag reduction due to the air deflector was 16.5% in the DNW-German Dutch wind tunnel experiment and 15% in the simulation.

Fig 5 and Fig 6 respectively show the streamwise velocity and static pressure coefficient distributions around the vehicle at an arbitrary time instant. A highly turbulent wake is clearly evident to the rear of the vehicle. Note that the side wakes were not perfectly symmetrical. This was because the mirrors on the two sides of the cabin had different shapes. As the yaw angle was increased, the separation on the right (windward) side was gradually mitigated, and the flow became fully attached at a 10° yaw angle. In contrast, the separation on the left (leeward) side was enhanced as the yaw angle was increased, and a strong negative pressure zone formed is shown in Fig 6. This greatly contributed to the increase in the drag force with the yaw.

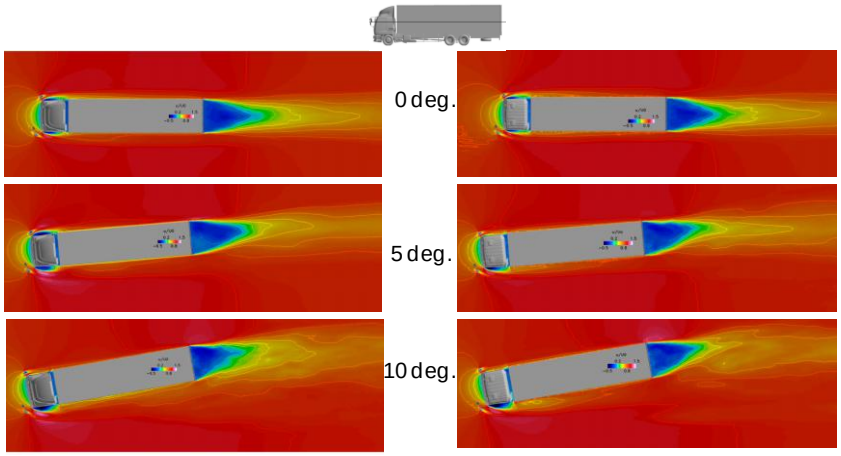

Fig. 5. Streamwise velocity u/U_0 distributions around vehicle (left: air deflector model, right: no air deflector model).

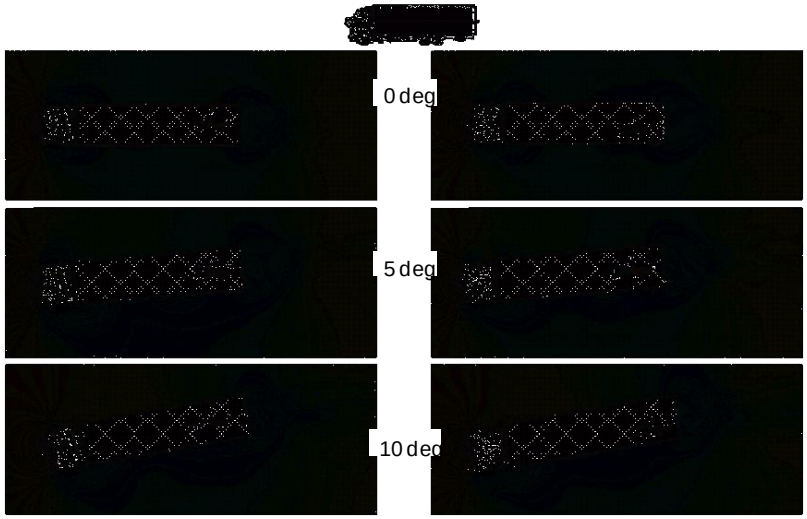

Fig. 6. Static pressure coefficient C_p distributions around vehicle (left: air deflector model, right: no air deflector model).

A vorticity iso-surface is presented in Fig 7. It clearly evident a number of prominent vorticity streaks are induced by topological features of the cab. The sharp corners of the cab cause flow separation and stream of vorticity trailing each corner. The complicated streaks are seen to be raised from the side mirror. The vorticity in the separation region behind the wheel cover as well as from complicated under body are also seen to create a long vorticity trail.

Fig 8 also shows that sharp corner of the front cab is a constant source of vorticity and therefore, it is an important role to increase the overall drag. Likewise, underbody components are also the strong sources of vorticity.

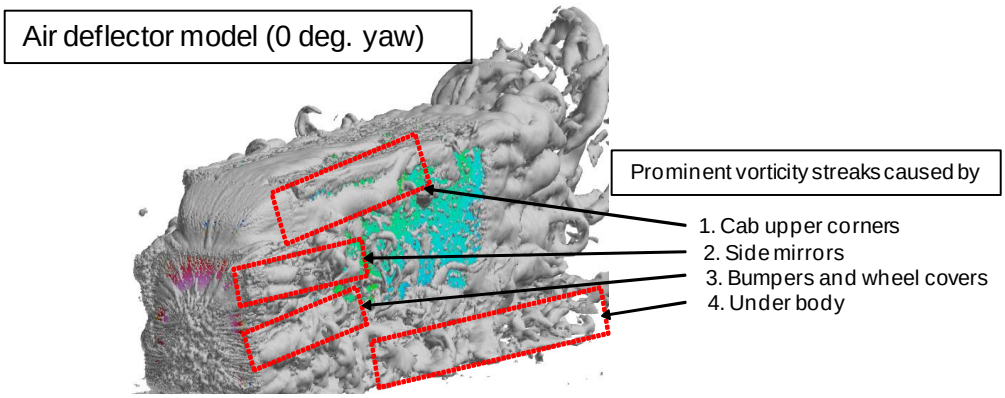

Fig. 7. An instantaneous vorticity magnitude iso-surface.

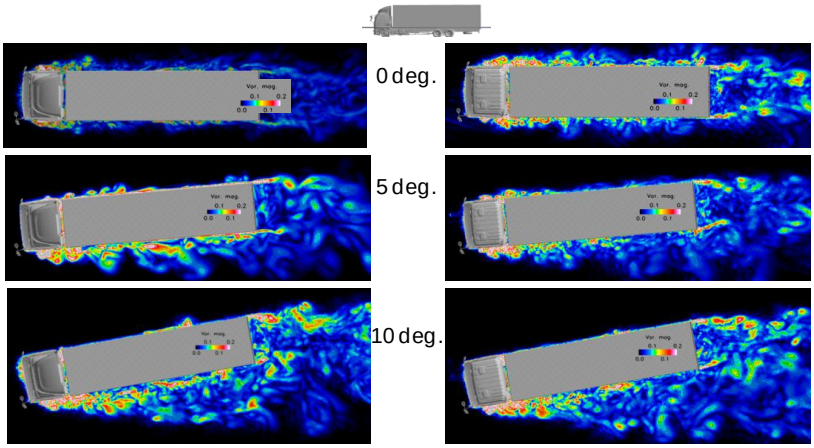

Fig. 8. Instantaneous vorticity contours around the vehicle (left: air deflector model, right: no air deflector model).

2.2 Flow-structure in the wake

The mean flow field in the truck's wake is depicted in Fig 9. A strong recirculation zone is clearly evident. Fig 10 shows the instantaneous vorticity contours at the vertical horizontal plane. They convected into the rear wake region from beneath the vehicle and contributed to the turbulence in the wake. For the air deflector model, when the yaw angle is 0°, the wake height gradually diminished in the flow-wise direction. When the yaw angle is 5° or 10°, the wake increased vertically as well as in the flow-wise direction. This partially contributed to the increase in the drag force. For no air deflector model, the flow greatly is separated at the front of the trailer, and the wake convected downstream and expanded along the vertical plane under both yaw and no yaw conditions.

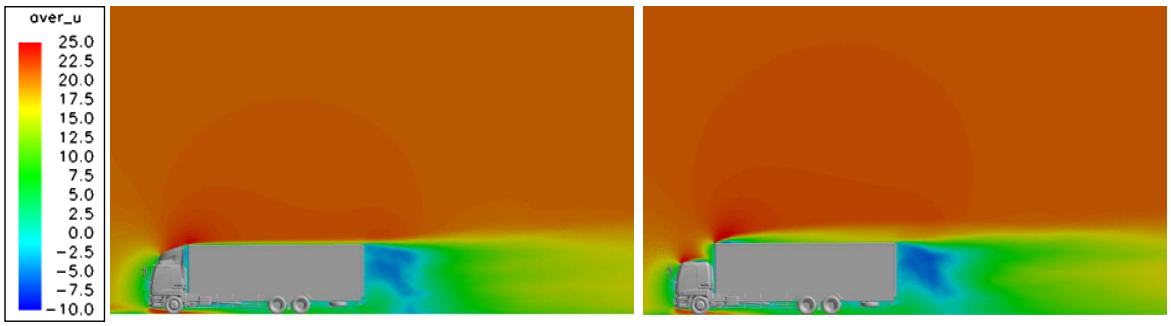

Fig. 9. Contours of velocity magnitude in the along the symmetry plane at 0 deg. yaw (left: with air deflector model, right: without air deflector model).

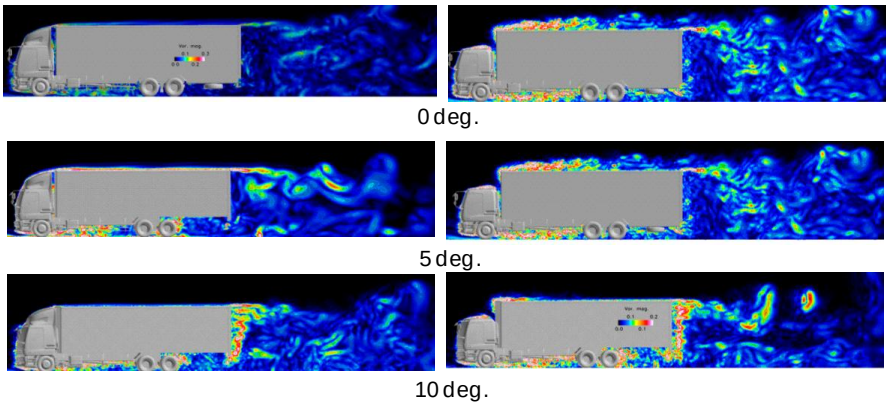

Fig. 10. Instantaneous vorticity contours in the wake (left: air deflector model, right: no air deflector model.

Instantaneous views of the wake flow structures are observed from Fig 7, 10 and 11. The shear layer created immediately behind the trailer's rear edges is clearly seen in Fig 7.

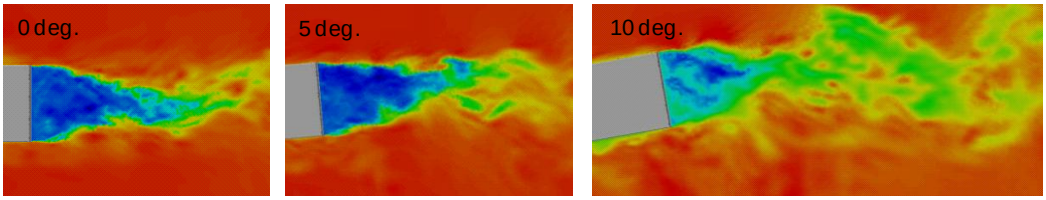

Fig. 11. Instantaneous velocity contours in the wake for air deflector model (top view).

The time-averaged total pressure contours around the model are visualized in Fig 12. For 10° yaw angle, there is a clear wake structure behind the model in the wake closure region and on the leeward side. For the baseline wind tunnel, the wake is distorted by the presence of the closed tunnel wall and extended in the longitudinal and vertical directions. For the ideal wind tunnel, the wake is freely formed and is not affected by the presence of the wall. For 10° yaw angle, a separation wake is formed on the leeward side and a wake from the near wake region was severely distorted by the wall. This is the reason for the increased drag at non-zero yaw.

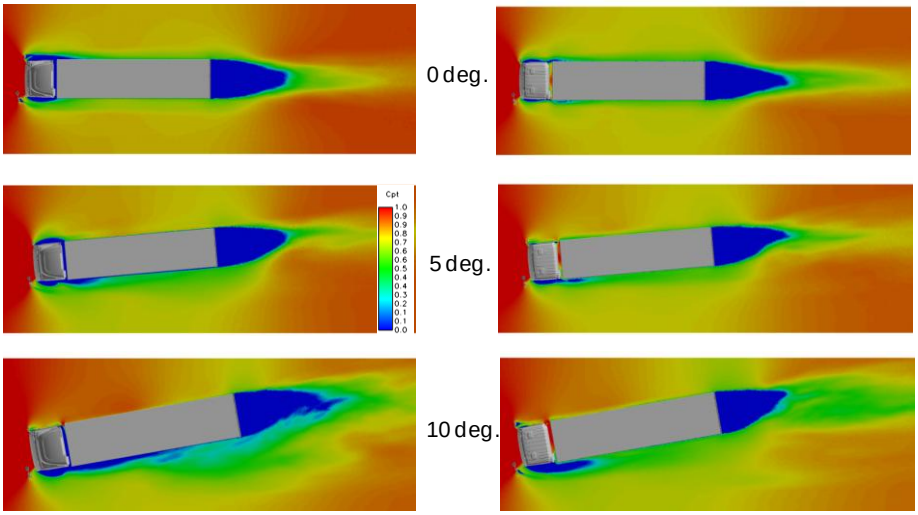

Fig. 12. Visualization of wake total pressure distribution (left: with air deflector model, right: without air deflector model).

2.3 Aerodynamic coefficients

The overall drag coefficient is calculated by integrating pressure and viscous stresses acting on all surfaces of the truck. In the present study the drag coefficients predicted with LES simulations are compared with corresponding experimental measurements to judge the accuracy of LES simulations. The full scale heavy duty truck was used in the experiments. All experiments were conducted in the DNW-German Dutch wind tunnel which has a cross-section area of 9.5m×9.5m and blockage ratio about 10%. Drag coefficient measurements were carried out for yaw angles of 0°, 5° and 10°. The experimental values were corrected by Maskell's equation in to get the blockage free drag coefficients [9-12]. The simplified Maskell's correction method based on momentum theory for use in testing thin flat plates normal to the freestream as follows:

$$\frac{q_c}{q} = \left[1 + k.C_{Duw}.\left(\frac{S}{C}\right)\right] \tag{7}$$

$$C_{Dw} = \frac{C_{Duw}}{\left(\frac{q_c}{q}\right)} \tag{8}$$

Three yaw angles (0°, 5° and 10°) with respect to the incoming flow were considered, and the results for the two models were compared. Note that the ideal data (i.e., the corrected experimental values) based on the experimental measurements were obtained by applying the blockage correction Eq. (8).

In the real road condition, blockage effect does not exist. To simulate such a condition, a numerical domain is created with its test section of 32 m×25 m in order to negligible blockage ratio. Hence, this situation is termed as an ideal condition, which has the blockage ratio of around 1%. The drag coefficient of both models are shown in Fig 13 and the errors in the simulated drag coefficient with respect to the experimental data for the model with the air deflector are summarized in Table 1. Notice that no indexes are attached to the vertical axis of Figs 13, 14 and 15. The numbers are purposefully eliminated since the aerodynamic coefficient values are not available in this point of confidentiality reason.

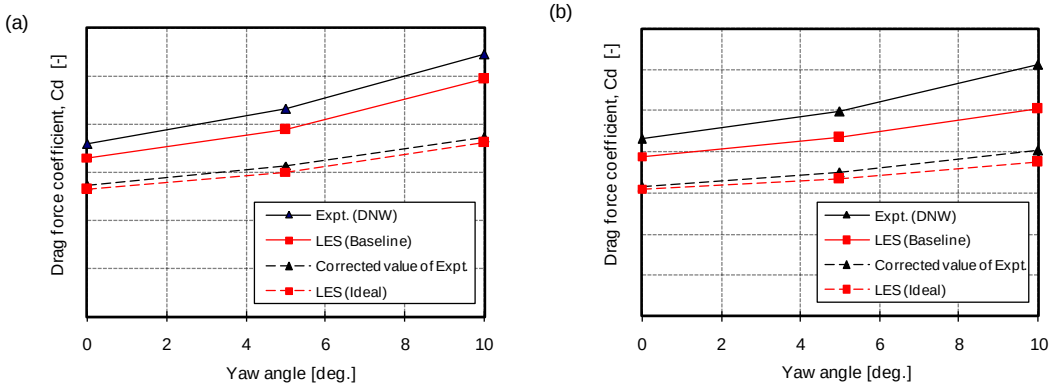

Fig. 13. Drag coefficient (C_d) (left: with air deflector model, right: without air deflector model).

Because we used more or less the same spatial resolution around the vehicle for all cases, the numerical discrepancies in the results are reasonably the same. The error less than -5% for the air deflector model and it varied from -1.3 % to 7% for the no air deflector depending on the yaw angle.

Table 1. Drag coefficient deviation from ideal LES from corrected data

Yaw angle [deg.]	0	5	10
With air deflector model	-3.3	-4.5	-3.3
Without air deflector model	- 1.3	-4.1	-7.1

The deviations in the simulated side force coefficient from the corrected experimental data for both models are summarized in Table 2. It was less than -5% for a 10° yaw angle but more than -11% for a 5° yaw angle. One reasonable explanation for this is that the correction equation used for the derived "ideal" drag result was also used for the side force correction result without considering the yaw angle effect.

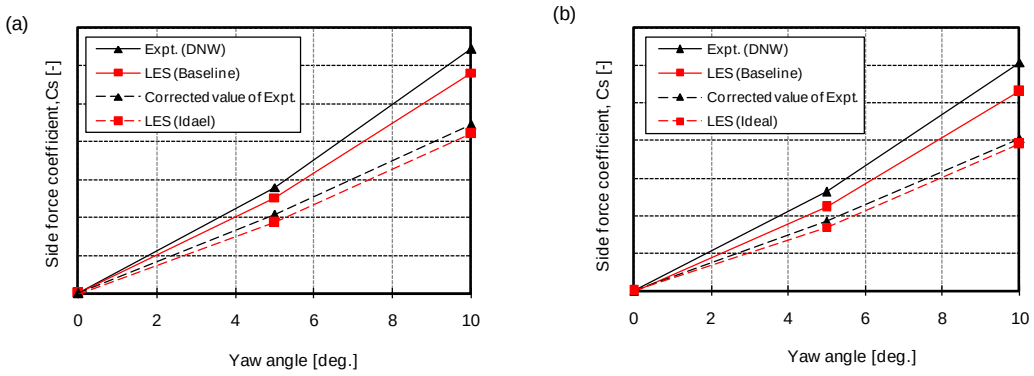

Fig. 14.Side force coefficient (C_s) (left: with air deflector model, right: without air deflector model).

Table 2. Side force coefficient deviation from ideal LES from corrected data

Yaw angle [deg.]	0	5	10
With air deflector model	negligible	-11.6	-4.8
Without air deflector model	negligible	-9.3	-3.7

The gap between the corrected experimental data and the simulated data is attributed to the difference between the virtual and DNW-German Dutch wind tunnels in the configurations of the ducts before and after the test section. As illustrated in Fig 3, we used a rectangular CFD domain in the simulations.

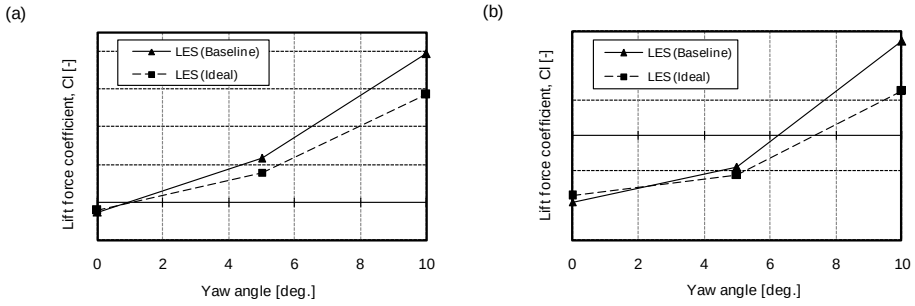

Fig. 15.Lift force coefficient (C_l) (left: with air deflector model, right: without air deflector model).

The simulated lift coefficients for both models are shown in Fig 16. The lift coefficient monotonically increased with the yaw angle and switched from a negative to a positive yaw angle between 5 and 10°, as shown in figure. Figs 14, 15 and 16 indicate the dependence of the drag, side force and lift force coefficients on the yaw angle and as well vehicle geometry, together with the DNW-Germen Dutch wind tunnel data for the drag and side forces. The magnitude of drag, side force and lift forces monotonically increase as the yawing angles increases.

3. Conclusions

Computational fluid dynamics flow simulations has been performed using large eddy simulation (LES) to assess the flow structure around the vehicle and the effects of yaw angle on vehicle aerodynamic coefficients. Several prominent features are observed in the front-end flow. A number of vorticity streaks are formed on the sides of the cab arising from upper

corners of the cab, side mirrors and the rear ends of the wheel covers. The vorticity streaks strongly influence the flow on the sides of the trailer.

The numerical simulation reflects observations that the wind tunnel test approach is more accurate in evaluating the vehicle aerodynamic drag, and the CFD approach is less constraining in terms of the operating conditions of the virtual wind tunnel. Drag coefficient is predicted most accurately within 5% of air deflector model and within 7% of no air deflector model by using a tetra-hydral mesh. Also simulated side force and lift force coefficients are achieved satisfactory agreement with experimental data. The computational work is expected to be applicable as a reference data to any heavy-duty truck geometry where flow is dominant by turbulent.

Acknowledgement

This work was supported by the Industrial Technology Research Grant Program in 2007 from the New Energy and Industrial Technology Development Organization (NEDO) of Japan. This study was conducted in a collaborative research project with Isuzu Advanced Engineering Center Ltd., and the geometry data and experimental data received are greatly appreciated.

References

[1] McCallen, R., Couch, R., Hsu, J., Browand, F., Hammache, M., Leonard, A., Salari, K., Rutledge, W., Ross, J., Storms, B., Heineck, J. T., Driver, D., Bell, J., Zilliac, G., 1999. " Progress in reducing aerodynamic drag for higher efficiency of heavy duty trucks (class 7-8)," SAE Paper 1999-01-2238 (1999).

[2] McCallen, R., Couch, R., Hsu, J., Browand, F., Hammache, M., Leonard, A., Salari, K., Rutledge, W., Ross, J., Storms, B., Heineck, J. T., Driver, D., Bell, J., Steve, W., Zilliac, G., 2000. " Aerodynamic drag of heavy (class 7-8): Simulation and benchmarking," SAE Paper 2000-01-2209 (2000).

[3] Modi, V.J., Hill, S.St., Yokomizo, T., 1995. "Drag reduction of trucks through boundary-layer control," Journal of Wind Engineering and Industrial Aerodynamics. 54/55, 583-594, 1995.

[4] Englar, R.J., 2001. "Advanced aerodynamic devices to improve the performance, economics, handling and safety of heavy vehicles," SAE Paper 2001-01-2072 (2001).

[5] Hucho, W, H., 1998. "Aerodynamics of road vehicles," Fourth Edition, SAE International, 1998.

[6] Das, P., 2011. "Effects of blockage on vehicle aerodynamics in closed-wall wind tunnel-A CFD study," Master's thesis No. EG-M101, Division of Mechanical and Space Engineering, Graduate school of Engineering, Hokkaido university, Japan, September 2001.

[7] Khondge, Ashok, D., Sovani, Sandeep, D., Lokhande, Bipin, S., Jain, Sunil, K., Long, Michael, P., 2004. "Simulation of the flow- field around a generic tractor-trailer truck," SAE Paper 20004-01-114 (2004).

[8] Smagorinsky, J., 1963. "General circulation experiments with primitive equations, I. The basic experiment," Monthly Weather Rev., vol.91, Num.3, pp 99-164, 1963.

[9] Maskell, E, C., 1963. "A theory of the blockage effects on bluff bodies and stalled wings in a closed wind tunnel," ARC R&M 3400, Nov. 1963.

[10] Cooper, K, R., 2006. "Closed-test-section wind tunnel blockage corrections for road vehicles," SAE International. SP- 1176, 2006.

[11] Das, P., Tsubokura, M., Matsuuki, T., Oshima, N., Kitoh, K., 2011. "Computational study of blockage effects on vehicle aerodynamic drag in closed-wall wind tunnel," Proceedings of the International Conference on Mechanical Engineering 2011 (ICME2011) 18-20 December 2011, Dhaka, Bangladesh, paper ICME11-FL-019.

[12] Mercker, E., BMW AG, Germany and Dr. Koro Kitoh, Kozo Kitoh Technology Inc, 2011: Private communication.

Available online at www.sciencedirect.com

SciVerse ScienceDirect

Procedia Engineering 00 (2012) 000–000

Procedia Engineering

www.elsevier.com/locate/procedia

5th BSME International Conference on Thermal Engineering

Unsteady MHD forced convective heat and mass transfer flow along a wedge with variable electric conductivity and thermophoresis

ATM. M. Rahman[1,*], M. S. Alam[2], M. A. Alim[3] and M. K. Chowdhury[4]

[1]Department of Computer Science and Engineering, Dhaka International University, Dhaka-1205, Bangladesh

[2]Department of Mathematics, Jagannath University, Dhaka-1100, Bangladesh

[3, 4]Department of Mathematics, Bangladesh University of Engineering and Technology, Dhaka-1000, Bangladesh

Abstract

In this paper the effects of thermophoresis on an unsteady magnetohydrodynamic (MHD) forced convective heat and mass transfer flow of viscous, incompressible and electrically conducting fluid over a wedge with variable electric conductivity have been investigated. The potential flow velocity has been taken as a function of the distance x and time t. The governing time dependent non-linear partial differential equations are transferred into locally similar ordinary differential equations and solve numerically by applying Nachtsheim-Swigert shooting iteration technique along with sixth order Runge-Kutta integration scheme. Steady solutions are compared with previously published works which show excellent agreement. The local similarity solutions for unsteady case are presented graphically for the velocity, temperature and concentration profiles in the boundary layer. The results show that skin friction coefficient, Nusselt number and Sherwood number are higher for the fluids of constant electric conductivity than those of the variable electric conductivity.

Keywords: Unsteady wedge flow; variable electric conductivity; thermophoreshis.

1. Introduction

Thermophoresis is a mechanism of particle deposition, besides other ones like inertial impaction, sedimentation, Brownian diffusion etc. Thermophoresis phenomenon has many engineering applications in removing small particles from gas streams, in determining exhaust gas particle trajectories from combustion devices, and in studying the particulate material deposition on turbine blades. Duwairi and Damesh [1] investigated the effects of thermophoresis particle deposition on mixed convection from vertical surfaces embedded in saturated porous medium. Rahman et al. [2] analyzed the local similarity solutions for unsteady two dimensional forced convective heat and mass transfer flow along a wedge with thermophoresis. Very recently, Adrian Postelnicu [3] studied the thermophersis partical deposition in natural convection over inclined surfaces in porous media

The study of magnetohydrodynamic flow of an electrically conducting fluid past an arbitrary shape surface has attracted the interest of many researchers in view of its important applications in many engineering problems. Recently, the problem of magnetohydrodynamic flow over surface has become more important due to the possibility of applications in areas like nuclear fusion chemical engineering, medicine and high-speed noiseless printing. Alam et al [4] studied two-dimensional steady MHD convective heat and mass transfer flow over an inclined flat plate with various flow conditions in the presence of thermophoresis.

* Corresponding author. Tel.: +880-1720557279; fax: +880-2-9871556.
E-mail address: atmmrahman2005@gmail.com

2. Governing Equations of the Flow

Let us consider an unsteady two-dimensional MHD forced convective heat and mass transfer flow of a viscous incompressible electrically conducting fluid along a heated impermeable wedge in the presence of thermophoresis. The angle of the wedge is given by $\Omega = \beta\pi$. The flow is assumed to be in the *x*-direction which is taken along direction of the wedge and the *y*-axis normal to it. The geometry of the problem has been shown in Fig.1.

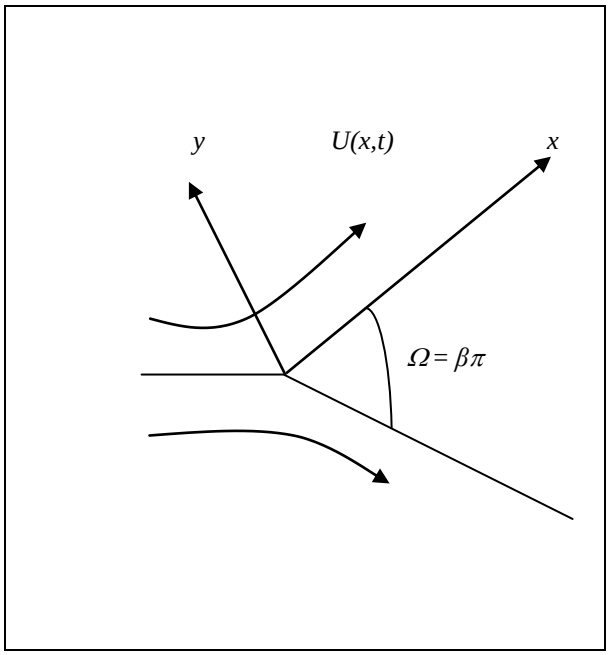

Fig.1: Flow configuration and co-ordinate system.

Then under the usual Boussinesq's and boundary layer approximations, the governing equations describing the conservation of mass, momentum, energy and concentration respectively can be written as follows (see also Rahman et.al. [2, 5, 6])

$$\frac{\partial u}{\partial x}+\frac{\partial v}{\partial y}=0, \tag{1}$$

$$\frac{\partial u}{\partial t}+u\frac{\partial u}{\partial x}+v\frac{\partial u}{\partial y}=\frac{\partial U}{\partial t}+U\frac{\partial U}{\partial x}+\upsilon\frac{\partial^2 u}{\partial y^2}-\frac{\sigma(B(x,t))^2}{\rho}(u-U), \tag{2}$$

$$\frac{\partial T}{\partial t}+u\frac{\partial T}{\partial x}+v\frac{\partial T}{\partial y}=\frac{\lambda_g}{\rho c_p}\frac{\partial^2 T}{\partial y^2}, \tag{3}$$

$$\frac{\partial C}{\partial t}+u\frac{\partial C}{\partial x}+v\frac{\partial C}{\partial y}=D\frac{\partial^2 C}{\partial y^2}-\frac{\partial}{\partial y}(V_T C), \tag{4}$$

where V_T is the thermophoretic velocity which is defined as follows

$$V_T=-\frac{\kappa\upsilon}{T}\frac{\partial T}{\partial y}. \tag{5}$$

For the flow under unsteady, it is relevant to assume that the applied magnetic field strength *B(x,t)* has the form

$$B(x,t)=B_0\sqrt{\delta/x}, \qquad B_0 \text{ is constant} \tag{6}$$

and the electrical conductivity is assumed to have the form as $\sigma = \sigma_0(u-U)$ where σ_0 is a constant.
Therefore using equation (6) into equation (2) , the momentum equation can be written as

$$\frac{\partial u}{\partial t} + u\frac{\partial u}{\partial x} + v\frac{\partial u}{\partial y} = \frac{\partial U}{\partial t} + U\frac{\partial U}{\partial x} + \upsilon\frac{\partial^2 u}{\partial y^2} - \frac{\sigma_0 B_0^2 \delta}{\rho x}(u-U)^2, \tag{7}$$

2.1. Boundary conditions

The applicable boundary conditions for the present model are as follows:

$u = 0, v = 0, T = T_w, C = C_w$,*at* $y = 0$, (8a)

$u = U(x,t), T = T_\infty, C = C_\infty$ *as* $y \to \infty$, (8b)

where *U(x,t)* is the potential flow velocity for the wedge flow which is taken as follows (see also Sattar [7] and Rahman et al. [2, 5, 6]):

$$U(x,t) = \frac{\upsilon x^m}{\delta^{m+1}}, \tag{9}$$

where *m* is an arbitrary constant and is related to the wedge angle and δ is the time dependent length scale which is taken to be as (see also Sattar [7] and Rahman et al. [2, 5, 6]) :$\delta = \delta(t)$. (10)

3. Dimensionless governing equation

To proceed we introduce the following non-dimensional variables:

$$\eta = y\sqrt{\frac{(m+1)}{2}}\sqrt{\frac{x^{m-1}}{\delta^{m+1}}}, \quad \psi = \sqrt{\frac{2}{m+1}}\,\frac{\upsilon x^{(m+1)/2}}{\delta^{(m+1)/2}} f(\eta), \; \theta(\eta) = \frac{T-T_\infty}{T_w - T_\infty}, \phi(\eta) = \frac{C-C_\infty}{C_w - C_\infty} \tag{11}$$

where η is the similarity variable , ψ is the stream function that satisfies the continuity equation (1) and is defined by $u = \partial\psi/\partial y$ and $v = -\partial\psi/\partial x$.
Now using equations (10)-(11) into equations (3), (4) and (7) we obtain the following non linear ordinary differential equations:

$$f''' + ff'' + \beta(1 - f'^2) - \frac{\delta^m}{\upsilon x^{m-1}}\frac{d\delta}{dt}(2 - 2f' - \eta f'') - \frac{2}{m+1}M(f'-1)^2 = 0, \tag{12}$$

$$\theta'' + \Pr f\theta' + \frac{\delta^m}{\upsilon x^{m-1}}\frac{d\delta}{dt}\Pr\eta\theta' = 0, \tag{13}$$

$$\phi'' + Scf\phi' + \frac{\delta^m}{\upsilon x^{m-1}}\frac{d\delta}{dt}Sc\eta\phi' + \frac{\kappa\, Sc}{N_t + \theta}[(N_c + \phi)\theta'' + \theta'\phi' - (\frac{N_c + \phi}{N_t + \theta})\theta'^2] = 0, \tag{14}$$

where $\beta = 2m/(m+1)$ is the wedge angle parameter that corresponds to $\Omega = \beta\pi$ for a total angle Ω of the wedge, $\Pr = \upsilon\rho c_p/\lambda_g$ is the Prandtl number, $Sc = \upsilon/D$ is the Schmidt number, $N_t = T_\infty/(T_w - T_\infty)$ is the thermophoresis parameter, $N_c = C_\infty/(C_w - C_\infty)$ is the concentration ratio and $M = \sigma_0 B_0^2\delta/\rho$ is the local magnetic field parameter.

The corresponding boundary conditions (8) becomes

$f = 0, f' = 0, \theta = 1, \phi = 1$ at $\eta = 0$, (15a)

$f' = 1, \theta = 0, \phi = 0$ as $\eta \to \infty$. (15a)

Now in order to make the equations (12)-(14) locally similar, let $\frac{\delta^m}{\upsilon x^{m-1}}\frac{d\delta}{dt} = \lambda,$ (16)

where λ is taken to be a constant and thus can be treated as a dimensionless measure of the unsteadiness.

Hence equations (12)-(14) becomes

$$f''' + ff'' + \beta(1 - f'^2) - \lambda(2 - 2f' - \eta f'') - \frac{2}{m+1} M (f' - 1)^2 = 0, \tag{17}$$

$$\theta'' + \Pr f\theta' + \lambda \Pr \eta\theta' = 0, \tag{18}$$

$$\phi'' + Scf\phi' + \lambda Sc\eta\phi' + \frac{k\ Sc}{N_t + \theta}[(N_c + \phi)\theta'' + \theta'\phi' - (\frac{N_c + \phi}{N_t + \theta})\theta'^2] = 0. \tag{19}$$

Further, we suppose that $\lambda = \frac{c}{x^{m-1}}$, where *c* is a constant so that $c = \frac{\delta^m}{\upsilon}\frac{d\delta}{dt}$. (20)

Thus integrating (20) we obtain that $\delta = [c(m+1)\upsilon t]^{1/m+1}$. (21)

Now taking $c = 2$ and $m = 1$ in equation (21) we obtain $\delta = 2\sqrt{\upsilon t}$ which shows that the parameter δ can be compared with the well established scaling parameter for the unsteady boundary-layer problems (see Schlichting and Gersten [8]).

3.1. Parameters of engineering interest

The parameters of engineering interest for the present problem are the local skin friction coefficient, local Nusselt number and the local Sherwood number which indicate physically wall shear stress, rate of heat transfer and rate of mass transfer, respectively and thermophoretic velocity. These physical quantities can be obtained from the following expressions:

$$1/2\, Cf\sqrt{2-\beta} = \mathrm{Re}^{-1/2} f''(0), \text{ where } \tau_w = \mu(\partial u/\partial y)_{y=0}. \tag{22}$$

$$Nu\sqrt{2-\beta} = -\mathrm{Re}^{1/2}\theta'(0), \text{ where } q_w = -\lambda_g(\partial T/\partial y)_{y=0}. \tag{23}$$

$$Sh\sqrt{2-\beta} = -\mathrm{Re}^{1/2}\phi'(0), \text{ where } M_w = -D(\partial C/\partial y)_{y=0}. \tag{24}$$

$$V_{Tw} = \left(\frac{V_T x}{\upsilon}\right)_{y=0} = -\sqrt{\frac{1}{2-\beta}}\,\mathrm{Re}^{1/2}\,\frac{\kappa}{1+N_t}\theta'(0). \tag{25}$$

Thus from equation (25) we observe that the non-dimensional thermophoretic velocity is proportional to the numerical values of $-\theta'(0)$.

4. Code validation

To check the validity of the present code, we have calculated the values of $f(0), f'(0)$ and $f''(0)$ for the Falkner-Skan boundary layer equation for the case $\beta = 0$, M = 0 and $\lambda = 0$ for different values of η . Table-1 shows the comparison of the data produced by the present code and those of White [9]. The results show a close agreement, hence justify the use of the present code.

Table 1: Comparison of the present numerical results of Falkner-Skan boundary layer equation for the case of $\beta = M = \lambda = 0$

η	$f(\eta)$		$f'(\eta)$		$f''(\eta)$	
	Present work	White[9]	Present work	White[9]	Present work	White[9]
0.0	0.00000000	0.00000	0.00000000	0.00000	0.47027089	0.46960
0.5	0.05872926	0.05864	0.23456114	0.23423	0.46568757	0.46503
1.0	0.23332581	0.23299	0.46127690	0.46063	0.43494906	0.43438
1.5	0.51575598	0.51503	0.66235843	0.66147	0.36218408	0.36180
2.0	0.88800281	0.88680	0.81770859	0.81669	0.25581418	0.25567
3.0	1.79780496	1.79557	0.97006212	0.96905	0.06763291	0.06771
4.0	2.78709815	2.78388	0.99872084	0.99777	0.00684790	0.00687
5.0	3.78738993	3.78323	1.00087632	0.99994	0.00025589	0.00026

5. Results and discussion

From the numerical computations non-dimensional velocity, temperature, concentration profiles and the thermophoretic velocity as well as the local skin friction coefficient, the local Nusselt number and the local Sherwood number are found for different values of the various parameters occurring in the problem. In the simulation of the values of *Pr* are chosen as 0.71, 1.74, 2.97 which correspond physically to helium, water, methyl chloride, respectively. The values of Schmidt number *Sc* is taken for Carbon-Dioxide $(Sc = 0.94)$. The default values of the parameters are chosen as, β = 1.6 (i. e. $\Omega = 288^0$), λ = 0.5, *Pr* = 0.71, *M* = 0.5, *Nc* = 3.00, $\kappa = 0.50$ and N_t = 2.00, unless otherwise stated. The effect of the various parameters on the flow, velocity, temperature and concentration fields are discussed in details in the following subsections

5.1. Effect of thermophoretic parameter

The variation of dimensionless concentration profiles for various values of thermophoresis parameter N_t have been shown in Fig. 2. .From Fig.2 it is readily seen that the concentration within the boundary-layer decreases with the increasing values of the N_t. Physical significance of the values of the thermophoretic parameter used here: when the wall is warm, bearing in mind the definition of thermophoresis parameter, $N_t T_w = (1+N_t)T_\infty$, so that $N_t = 1$ means a wall twice warmer than the ambient fluid, i. e. $T_w = 2T_\infty$, while $N_t = 1000$ describes a very cold wall.

5.2. Effect of thermophoretic coefficient and concentration ratio

The variation of dimensionless concentration profiles for various values of thermophoretic coefficient κ and the concentration ratio N_c are shown in Figs. 3-4, respectively. From these figures, we observed that concentration profiles within the boundary-layer increases with the increasing values of the thermophoretic coefficient κ and the concentration ratio N_c

5.3. *Effect of thermophoretic velocity*

The combined effects of thermophoretic parameter N_t and unsteadiness parameter λ on the dimensionless wall thermophoretic velocity have been shown in Fig. 5. Increasing the thermophoretic parameter N_t leads to lower wall deposition velocities (curves N_t = -16, -4, -2) and larger wall thermophoretic velocities (curves N_t = 2, 4, 16) as seen in Fig. 5. This effect of N_t on V_{TW} is easily explained by inspection of equation (25).

The combined effects of β and λ; *Pr* and λ, on the dimensionless wall thermophoretic velocity ($V_{Tw}\,\mathrm{Re}^{-\frac{1}{2}}$) when $N_t = \pm 2$ are shown in Figs. 6-7, respectively. From these figures we see that thermophoretic velocity increases for increasing values of wedge angle parameter β and Prandtl number *Pr* (when $N_t > 0$) while it decreases (when $N_t < 0$).

In Table-2 we have presented the local skin-friction coefficient, rate of heat transfer and rate of mass transfer for different values of the unsteadiness parameter considering the case of variable fluid electric conductivity (VEC) and constant fluid electric conductivity (CEC).This table shows that when λ decreases from 0 to 2.5 then the local skin friction coefficient decreases by 89.80% (for the case of VEC) and 94.38% (for the case of CEC). It is also see that for both varable electric conductivity (VEC) and constant electric conductivity (CEC) cases the value of $-\theta'(0)$ and $-\phi'(0)$ increase with the increase of λ.

Table 2 : Values of $f''(0)$, $-\theta'(0)$ and $-\phi'(0)$ for various values of λ

λ	$f''(0)$		$-\theta'(0)$		$-\phi'(0)$	
	VEC	CEC	VEC	CEC	VEC	CEC
0.0	1.5128	1.5345	0.5204	0.5213	0.4950	0.4958
0.5	1.2631	1.2884	0.6762	0.6772	0.6395	0.6404
1.0	0.9827	1.0130	0.8064	0.8075	0.7605	0.7615
1.5	0.6639	0.7014	0.9188	0.9201	0.8645	0.8657
2.0	0.2939	0.3425	1.0185	1.0200	0.9565	0.9579
2.5	0.1543	0.1862	1.1077	1.1098	1.0387	1.0407

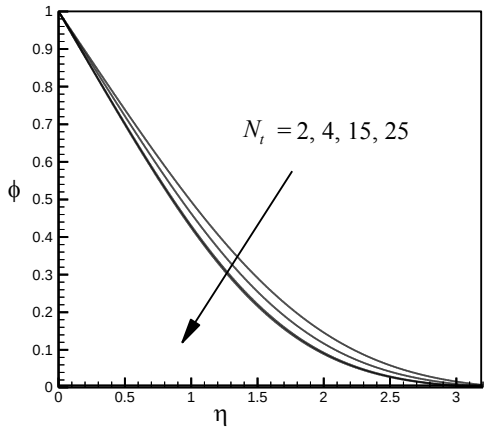

Fig.2: Effects of N_t on concentration for Pr = 0.71, Sc = 0.94, M = 0.50. β = 1.6 (i. e. $\Omega = 288^0$)

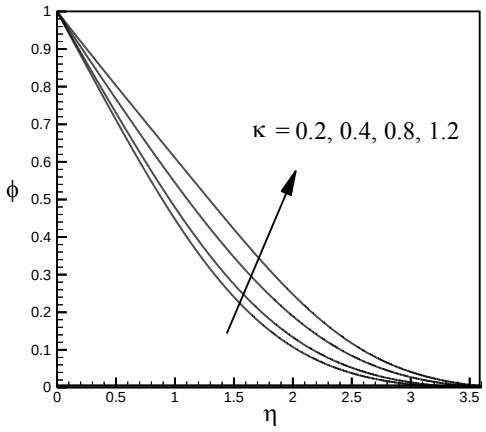

Fig. 3: Effects of k on concentration for Pr = 0.71, Sc = 0.94, M = 0.50. β = 1.6 (i. e. $\Omega = 288^0$)

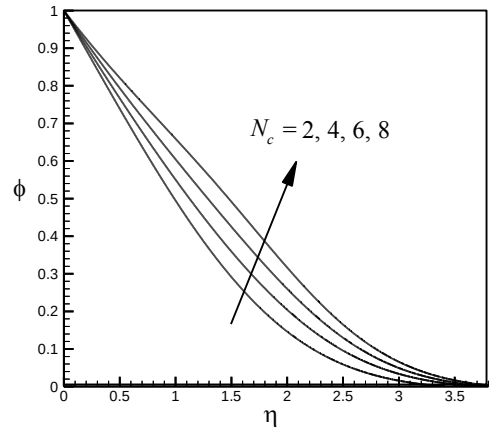

Fig. 4: Effects of Nc on concentration for Pr = 0.71, Sc = 0.94, M = 0.50. β = 1.6 (i. e. $\Omega = 288^0$)

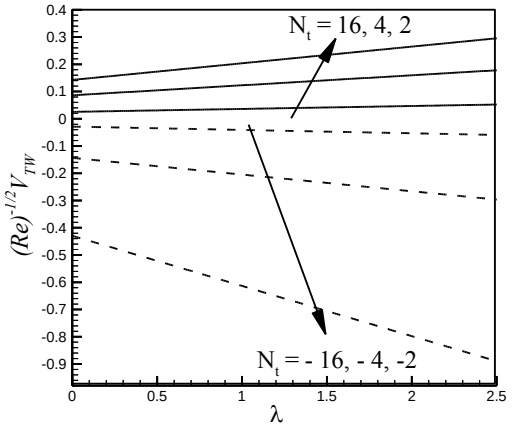

Fig. 5: Effects of λ and (Nt > 0 and Nt < 0) on thermophoretic velocity for, β = 1.6 (i. e. $\Omega = 288^0$), Sc = 0.94, Nc = 3.00, Pr = 0.71, k = 0.50 and M = 0.5.

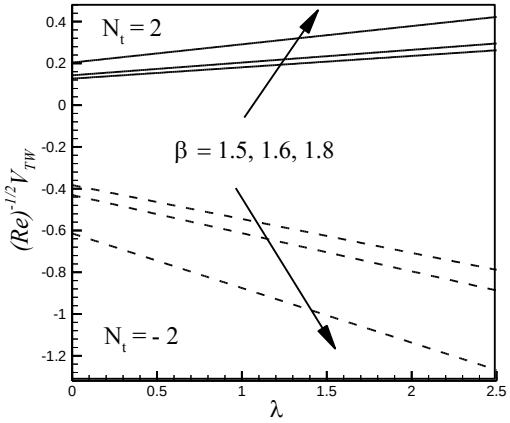

Fig. 6: Effects of λ and β on thermophoretic velocity for Sc = 0.94, Nc = 2.00, Pr = 0.71, k = 0.50, M = 0.5, $N_t = \pm 2.0$

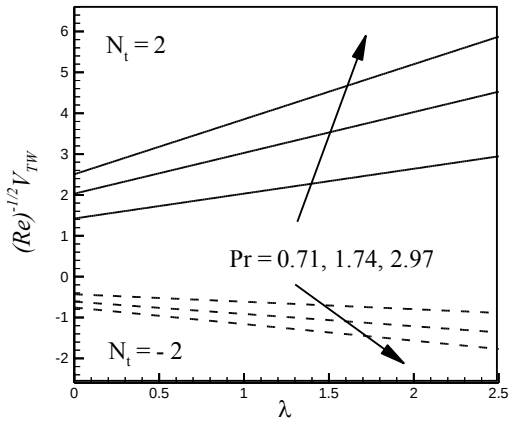

Fig. 7: Effects of λ and Pr on thermophoretic velocity for, β = 1.6 (i. e. $\Omega = 288^0$), Sc = 0.94, Nc = 2.00, k = 0.50, M = 0.5, $N_t = \pm 2.0$.

6. Conclusion

In this paper we have discussed the effects of variable electric conductivity and thermophoresis on an unsteady two-dimensional forced convective heat and mass transfer flow over a heated impermeable wedge. The numerical results have been presented in the form of graphs and tables. From the present numerical investigations the following major conclusions may be drawn:

(i) Concentration within the boundary-layer decreases with the increasing values of the thermophoretic parameter whereas it increases as increases the thermophoretic coefficient as well as the concentration ratio.

(ii) Wall thermophoretic velocity increases for increasing values of wedge angle parameter β and Prandtl number Pr (when $N_t > 0$) while it decreases (when $N_t < 0$).

(iii) The local skin friction coefficient, Nusselt number and Sherwood number are higher for the fluids of constant electric conductivity than those of the variable electric conductivity.

References

[1] Duwairi H. M., Damesh R. A., 2008. "Effects of thermophoresis particle deposition on mixed convection from vertical surfaces embedded in saturated porous medium," Int. J. Numer. Meth. Heat Fluid Flow, 18(2), pp. 202-216.

[2] Rahman AT.M. M., 2012. " Alam M. S., Chowdhury M. K., 2012. " Local similarity solutions for unsteady two dimensional forced convective heat and mass transfer flow along a wedge with thermophoresis," Int. J. Appl. Math and Mech, 8 (8), pp. 96-112.

[3] Postelnicu A., 2012. " Thermophersis partical deposition in natural convection over inclined surfaces in porus media," Int. J. Heat and Mass Transfer, 55, pp. 2087-2094.

[4] Alam M. S., Rahman M. M., Sattar M. A., 2008. " Effects of variable suction and thermophoresis on steady MHD combined free-forced convective heat and mass transfer flow over a semi-infinite permeable inclined flat plate in the presence of thermal radiation," Int. J. Thermal Sci., 47, pp. 758-765.

[5] Rahman ATM. M. , Alam M. S., Chowdhury M. K., 2012. "Effects of variable thermal conductivity and variable prandtl number on unsteady forced convective flow along a permeable wedge with suction/injection in the presence of thermophoresis," Int. J. Energy & Technology, 4(4), pp. 1-10.

[6] Rahman, ATM. M. Alam M. S., Chowdhury M. K, 2012. "Thermophoresis particle deposition on unsteady two-dimensional forced convective heat and mass transfer flow along a wedge with variable viscosity and variable Prandtl number," Int. Communications in Heat and Mass Transfer, 39, pp. 541-550.

[7] Sattar M. A., 2011. " A local similarity transformation for the unsteady two-dimensional hydrodynamic boundary layer equations of a flow past a wedge," Int. J. Appl. Math. and Mech., 7(1), pp. 15-28.

[8] Schlichting H., Gersten K., Boundary Layer Theory, 8th Edition, Springer- Verlag, Berlin/Heidelberg, 2000.

[9] White F. M. Viscous Fluid Flows, third ed. McGraw-Hill, New York. 2006.

Available online at www.sciencedirect.com

SciVerse ScienceDirect

Procedia Engineering 00 (2012) 000–000

Procedia Engineering

www.elsevier.com/locate/procedia

5th BSME International Conference on Thermal Engineering

Numerical simulation of 2D turbulent natural convection of humid air in a cavity filled with solid objects

Draco Iyi, Reaz Hasan* and Roger Penlington
Northumbria University, Newcastle Upon Tyne, NE1 8ST, UK
*Email: reaz.hasan@northumbria.ac.uk

Abstract

Natural convection flow in enclosures containing solid objects is important in the design of a wide range of industrial and engineering applications. Numerical calculations were performed for low turbulence double-diffusion convection for humid air inside a rectangular cavity with an aspect ratio of 2:1(height/width) and partially filled with disconnected solid cylindrical objects occupying 15% of the total cavity volume. The vertical walls are maintained at 1.2 and 21°C and a Rayleigh number of the fluid mixture based on the height of the vertical wall is 1.45 x 10^9. In the computations, turbulent fluxes of momentum, heat and mass were modelled by a low-Re (Launder-Sharma) k-ε eddy diffusivity model. Radiation equation was discretised using the discrete ordinate method. Detailed analysis was performed on the flow and heat transfer and on the turbulence quantities within the cavity. The effect of 2D simplification of inherently 3D radiation modelling was carefully scrutinised and calculations carried out with an equivalent emissivity. Variations of average Nusselt number and buoyancy flux are analysed. Profiles of turbulent kinetic energy and turbulent viscosity are studied in detail to observe the net effect on the intensity of turbulence caused by the interactions of radiation with double-diffusive natural convection heat and mass transfer. Particular emphasis was placed on quantifying the proximity of the solid objects to the active walls. It has been found that turbulence is suppressed as the objects get closer to the walls.

Keywords: Double diffusive heat and mass transfer; natural convection; emissivity;

1. Introduction

Simultaneous heat and mass transfer in enclosures containing solid objects is important for many practical flows such as indoor environments (Chen and Liu 2004; Ji et al., 2007), drying/cooling of agricultural products (Kadem et al,. 2011) and other engineering applications (Laguerre et al., 2005). The basic set up for such flows, which has also attracted attention from both experimental and numerical scientists, is a rectangular cavity whose vertical walls are heated differentially (Tian and Karayiannis, 2000; Didier et al., 2011). Typically, the natural convection heat transfer from the hot to the cold wall is characterised by the formation of a slow moving vortex. This vortical motion is often interpreted as an 'engine' which transfers heat from the heated surface (source) to the cold surface (sink) (Bejan, 1993). The intensity of flow is conveniently expressed by the Rayleigh number, $Ra = g\beta\Delta TH^3/\alpha\nu$, where, H is the height of the cavity, β is coefficient of thermal expansion, ΔT is the temperature difference between the vertical walls and α and ν are the thermal and molecular diffusivities of the fluid respectively. Depending on the Rayleigh number the flow can be categorised as turbulent or laminar.

In the last decade or so the trend in buoyancy driven flow research has shifted to the examination of cavity flow coupled with heat and mass transfer. Most of the studies in this category are concentrated on steady state laminar flow of Rayleigh number ranging from 10^4 to 10^6. Hammou et al., 2004 and McBrain, 1997 investigated temperature and mass concentration gradient induced laminar flow in an enclosure. They used single phase modelling approach for the transport of fluid mixture. It is fairly recently that a number of works have appeared on buoyancy driven flows in enclosures filled with varying numbers of solid objects. Unlike porous medium, these objects are not in contact with each other but are close enough to influence the transfer processes significantly (Das and Reddy, 2006; Laguerre et al., 2009). Most of such works

are limited to steady state two dimensional laminar flow of Rayleigh number ranging from 10^5 to 10^9, although the higher values of Rayleigh number are likely to be turbulent. The flow development is further complicated by the evidence that radiation also plays an important role (Behnia et al., 1990; Iyi et al., 2012) in establishing the flow.

An important aspect of the above type of flow which has not been investigated in detail is the effect on heat and mass transfer due to the wall proximity of blockages. This issue has many practical engineering applications such as natural drying of wood stacks (Kadem et al., 2011), cold storage stacking (Laguerre et al., 2005) or location of venetian blinds in double facade (Ji et al., 2007). The objectives of this paper are hence to look at typical features of the heat and mass transfer for variable proximity of the solid objects. The issue of emissivity for radiation simulation has also been explored.

2. Flow domain

The geometrical configuration used in this investigation is similar to the cavity used in the experimental study conducted by Laguerre et al., 2009. As shown in Figure 1, this is a two-dimensional rectangular cavity with aspect ratio of 2:1 (H/L) and contains objects which occupy about 15% of the total cavity volume. The authors have provided data for temperature profiles along the mid-height (y/H=0.5) and along x=6.6 cm (or δ = 6.6) near the cold wall of the cavity. Vertical velocity and relative humidity profiles measured at the mid-height and mid-width (x/L=0.5) of the cavity were also reported.

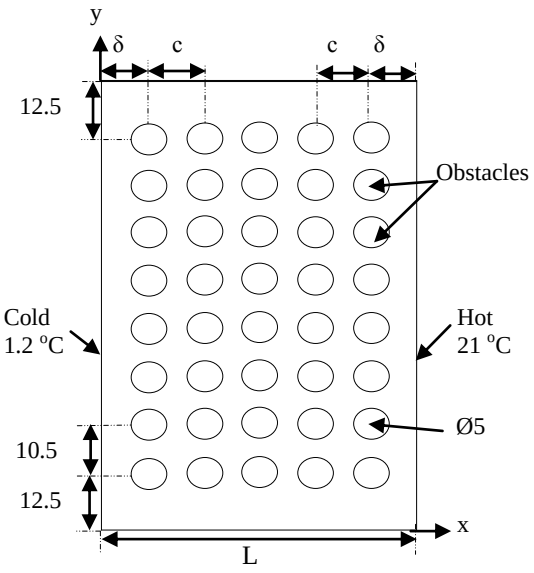

Figure 1. Geometry and the coordinates (dimensions are in cm)

Based on the temperature differentials of the vertical walls the Rayleigh number was found to be 1.45 x 10^9. For this work, the distance of the first column of objects from both the hot and cold walls were varied (δ = 0.033, 0.05, 0.066, 0.08 and 0.116 m). The distances between the other columns, 'c', varies negligibly and hence the effect due to internal re-distribution is ignored.

3. Numerical Method

Calculations were carried out using the commercial CFD package of ANSYS FLUENT (2010) software. The methodology involves the iterative solution of the Navier-Stokes equations along with continuity and energy equation on collocated variables within a structured-unstructured mesh configuration. Humidity has been considered as a separate phase and hence another scalar transport equation for species transport has been incorporated. To model the turbulence stresses, a two-equation low-Re eddy-viscosity turbulence model (Launder-Sharma, 1974) has been chosen. Systematic grid dependency tests were carried out and the final results were obtained with 90,500 cells with a y^+ value of just below 1. For a coarser mesh density of 64,600 the average Nusselt number showed very small variation as can be seen in Table 1. Initial natural convection flow field was established for a Rayleigh number of 10^6 using an incompressible unsteady solver with a time step of 0.002s. This flow field was later used an initial condition for the higher Rayleigh number of 1.45 x 10^9. A typical run on a single Intel core 2Duo E6600 2.4 GHz processor took about 8 hours of computing time.

The boundary conditions considered for the simulations are similar to those given in the experimental paper of Laguerre et

al., (2009). The temperatures of the hot, cold, top and bottom walls were fixed at 21, 1.2, 14.4 and 13.7^{o}C respectively. The constant vapour mass fraction is maintained at the bottom horizontal wall and a constant mass fraction equal to the saturation value at the cold wall was specified. No slip boundary conditions have been imposed for all the solid surfaces. To simulate radiation, Discrete Ordinate Method [FLUENT 2010] has been chosen with humid air treated as absorbing-emitting and non-scattering gray medium and the walls are all assumed as gray diffuse.

4. Results and Discussion

The velocity and turbulence intensity contours shown in Figure 2 (a) and (b) respectively, demonstrate clearly that the main air flow is confined within the boundary layer so that the objects close to the walls interact with the viscous layer. This observation further highlights the importance of using a low-*Re* model. It can also be seen that there are other streams of flows of varying (smaller) magnitude. Such a flow pattern was also verified and reported in the experimental work of Laguerre et al., 2005 and can be seen in Figure 2.

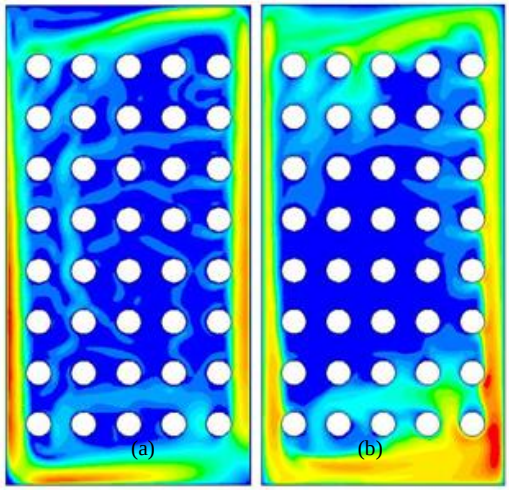

Figure 2. (a) Velocity magnitude and (b) Turbulence intensity for δ = 6.6 cm

Double-diffusive phenomenon is governed by the total density stratification consisting of thermal and concentration contributions. These two stratifications often act in opposite directions with unstable thermal stratification promoting turbulence, while the stable concentration gradient tends to dampen turbulent fluctuations. In this study, thermal stratification is dominant and is likely to promote turbulence. Specification of the flow regime for such transitional Rayleigh number of 1.45 x 10^{9} associated with heat and mass transfer appears to be quite confusing. To resolve this uncertainty surrounding the flow regime characterisation, preliminary numerical investigation was conducted with Launder-Sharma model to show if the domain is predominantly laminar or turbulent. The temperature profile near the cold wall (x = 6.6 cm) is presented in Fig. 3a, and the relative humidity (RH) distribution along the mid-width (x/L = 0.5) is presented in Fig. 3b. Both results, laminar and turbulent are plotted against the experimental data which supports our assumption of incorporating a turbulence model in the calculations.

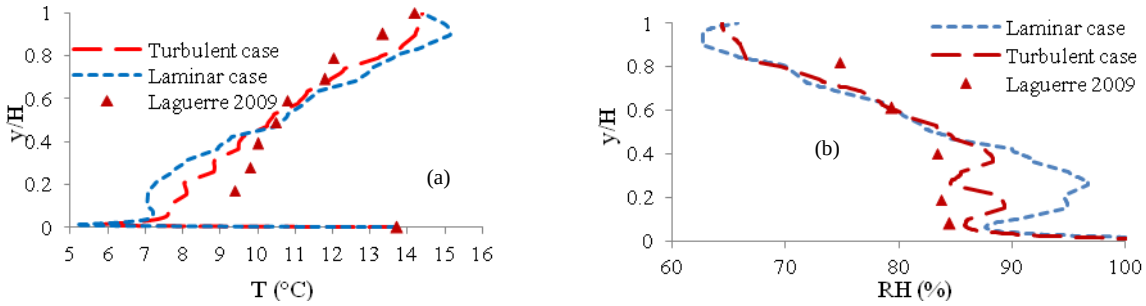

Fig. 3 Comparison with experimental data: laminar vs turbulent prediction (δ = 6.6 cm)

4.1 Choice of equivalent emissivity

The choice of emissivity is very critical when modelling radiation heat transfer and, even for this type of moderate temperature difference, the effect of radiation has been found to be fairly significant (Iyi et al., 2012). The 2D simplification of an inherently 3D radiation heat transfer also raises issues with the accuracy of the data produced by 2D simplification of domain. According to Laguerre et al., 2009 an equivalent emissivity of $\varepsilon = 0.58$ can be shown to mimic the radiation heat transfer between three surfaces having emissivities of 0.9 (somewhat similar to the treatment of radiation shield). However, no numerical evidence is provided in support of the above. We have scrutinized this assumption and a comparison of temperature for a 2D vs. 3D domain is presented in Fig. 4. It can be seen that the predicted temperatures for $\varepsilon = 0.9$ (3D) and $\varepsilon = 0.58$ (2D) are in fairly close agreement justifying the 2D treatment. The $\varepsilon = 0.9$ (2D) is shown for comparison which also highlights the significant influence of radiation for this flow. All of the calculations reported in this paper were obtained with $\varepsilon = 0.58$.

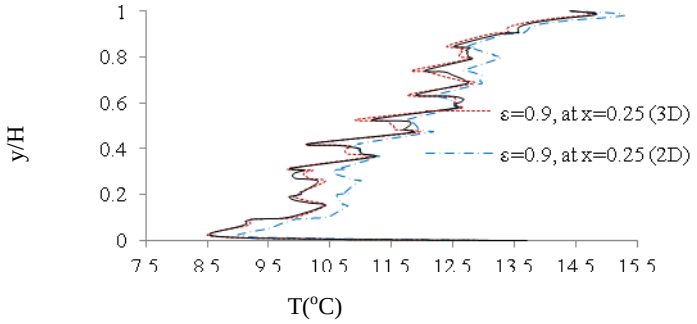

Fig. 4 Emissivity sensitivity for temperature prediction ($\delta = 6.6$ cm)

4.2 Wall heat transfer

Average and local heat transfer data are compared in terms of an average Nusselt number and local Nusselt number computed at each wall. The total Nusselt number which is a combination of heat transfer due to convection and radiation were separately calculated by taking integral averages of heat fluxes using FLUENT post-processing tools. Similarly the local Nusselt numbers were obtained using the local heat flux at each node. Table 1 shows the average Nusselt number for various walls for various values of δ and Fig. 5 shows the local variations.

Table 1: Variation of Average Nusselt Number
(Italicised data for $\delta = 0.066$ are for coarse mesh of 64,600 cells)

δ (m)	Bottom wall	Hot wall	Top wall	Cold wall
0.033	33.8	82	10.4	105.5
0.05	34.1	105.3	7.3	132.1
0.066	30.5(*30.4*)	111.6 (*111.3*)	3.9(*3.8*)	138.2(*137.8*)
0.08	30.4	113.9	2.7	141.5
0.12	29.1	118.5	1.7	146

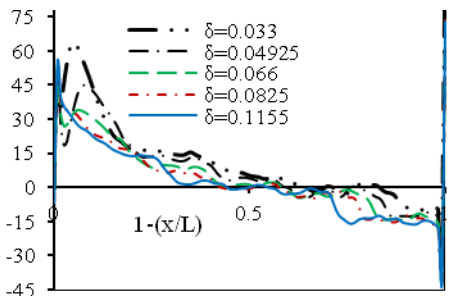

(a) Top wall

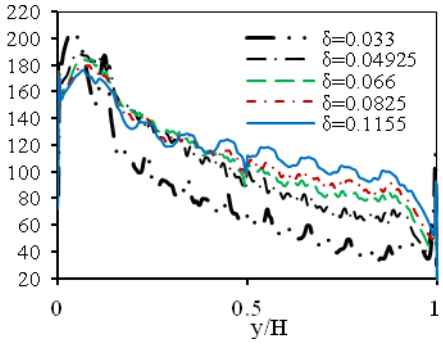

(b) Hot wall

Fig. 5 Variation of Local Nusselt number along the (a) top and (b) hot wall

The table shows that the total heat transfer is significantly low for the smallest δ value. For other values the average Nu demonstrates a small but monotonic increase of the heat transfer. The local variations of Nu along the hot wall display the proximity effect very clearly. It also shows that with larger δ values, the Nu numbers tend to smooth out. The fact that δ=3.3 cm shows markedly small value of heat transfer may be partly related to the fact that turbulence is greatly suppressed due to blockage of the upward and downward flow of fluids along the hot and cold walls respectively. The turbulent viscosity ratio, μ_{ratio} (ratio of turbulent eddy viscosity divided by the molecular viscosity) in Fig. 6, highlights that turbulence is greatly reduced as the objects come closer to the walls and supports the multi-zone configuration of flow as suggested by among others, Griffiths and Chen, 2003.

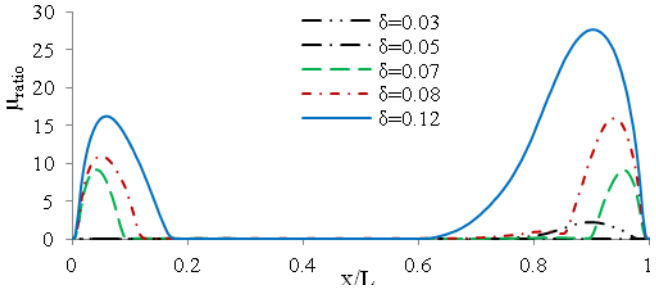

Figure 6. Turbulent viscosity ratio at the mid-height

4.3 Influence of proximity on mass transfer

Detailed analyses were carried out on the vapour mass flow distributions at various locations of the flow domain. Typical plots of mass fraction, m (g/kg) and buoyancy number, N, defined as the ratio of mass to temperature induced buoyancy, are plotted in Figs. 7 and 8. It can be seen that the mass fraction of vapour increases for the smaller δ values. This is due to the smaller gap available for the flow and is essentially a redistribution of the moisture content throughout the flow domain. The buoyancy number, N, measures the contribution to buoyancy of the variation in vapour concentration. The concentration gradient is due to difference in the relative molecular mass between the dry air and water vapour. At 20 ^{o}C, the relative molecular mass of dry air is 28.97 kg/kg-mol, whilst for saturated air it is 28.71 kg/kg-mol. As expected the effect due to mass induced buoyancy is small and corresponds to the trend in Fig. 7.

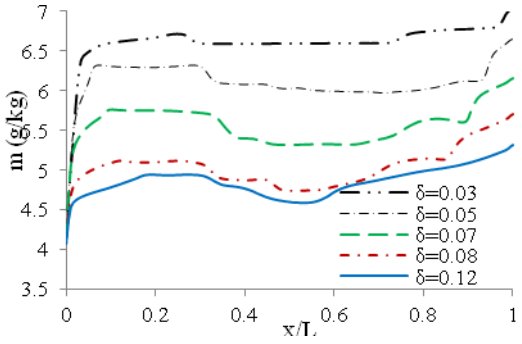

Figure 7: Mass fraction along the mid-height

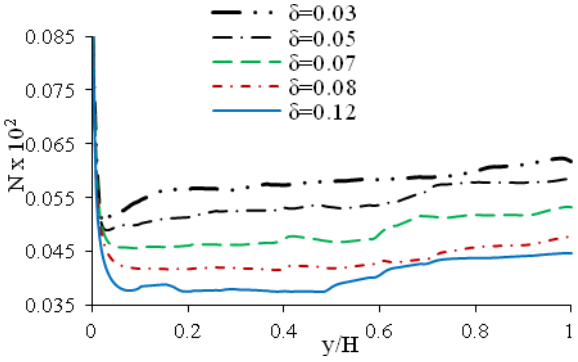

Figure 8: Buoyancy number along the mid-height

The effective diffusion coefficient, D_{eff} of vapour shown in Fig. 9 at the mid-height. The variations and nature of these curves are very similar to the viscosity ratio curves presented in Figure 6, highlighting the fundamental similarity in the diffusive transport mechanisms of momentum and concentration.

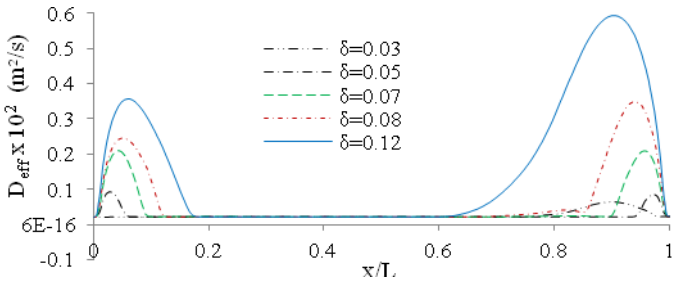

Figure 9: Effective diffusion coefficient of vapour at mid-height

5. Conclusions

The following conclusions can be made from the work presented above:

- The flow field is characterised by low turbulence near the walls while the core area is essentially a stagnant region.
- Given that an appropriate equivalent emissivity is obtained, a 2D simplification of a 3D domain is possible to save computational effort.
- Wall proximity can be seen to affect the overall heat transfer via flow field. The effect of turbulence is greatly reduced as the gap between the walls and the solid objects become smaller.

References

[1] Chen W, Liu W. Numerical and experimental analysis of convection heat transfer in passive solar heating room with greenhouse and heat storage. Solar Energy, 2004;76: 623–33.
[2] Ji Y, Cook MJ, Hanby VI, Infield DG, Loveday DL and Mei I. CFD modelling of double-skin facades with venetian blinds. Proc. Building Simulation, 2007.
[3] Kadem S, Lachemet A, Younsi R, Kocaefe D. 3d-Transient modeling of heat and mass transfer during heat treatment of wood. Int. Communications in Heat and Mass Transfer, 2011;38:717-22.
[4] Laguerre O, Ben Amara S, Flick D. Experimental study of heat transfer by natural convection in a closed cavity: Application in a domestic refrigerator. Journal of Food Engineering. 2005;70:523–37.
[5] Tian SY, Karayiannis TG. Low turbulence natural convection in an air filled square savity. Part II: The turbulence tuantities. International Journal of Heat and Mass Transfer. 2000;43:867-84.
[6] Didier S, Rouger N, Francis D, Francois P. Natural convection in an air-filled cavity: Experimental results at large Rayleigh numbers. Int. Communications in Heat and Mass Transfer, 2011;38:679-87.
[7] Bejan A. Heat Transfer. New York:Wiley; 1993.
[8] Hammou ZA, Benhamou B, Galanis N, Orfi J. Laminar mixed convection of humid air in a vertical channel with evaporation or condensation at the wall. Int. J. Therm. Sci. 2004;43:531–9.
[9] McBrain GD. Natural convection with unsaturated humid air in vertical cavity. Int. J. Heat Mass Transfer. 1997;40(13):3005-12.
[10] Das MK, Reddy SK. Conjugate natural convection heat transfer in an inclined square cavity containing a conducting block. Int. J. Heat Mass Transfer. 2006;49:4987–5000.
[11] Laguerre O, Benamara S, Remy D, Flick D. Experimental and numerical study of cavity filled with solid obstacles. Int. J. of Heat and Mass Transfer. 2009;25:5691-700.
[12] Behnia M, Reizes JA, De Vahl Davis G. Combined radiation and natural convection in a rectangular cavity with a transparent wall and containing a non-participating fluid. Int. J. for Numerical Methods in Fluids. 1990; 10(3):305-25.
[13] Iyi DA, Hasan R, Penlington R. Interaction effects between surface radiation and double-diffusive turbulent natural convection in an enclosed cavity filled with solid obstacles. Proc. of Advances in Computational Heat Transfer, ICHMT , Bath, UK, 2012.
[14] ANSYS FLUENT 13.0 (2010).
[15] Launder BE, Sharma BI. Application of the energy-dissipation model of turbulence to the calculation of flow near a spinning disc. Letters in Heat and Mass Transfer, 1974;1:131–8.
[16] Griffiths B, Chen Q. A Momentum-zonal model for predicting zone airflow and temperature distributions to enhance building load and energy simulations. HVAC & R Research. 2003;9(3):309-25.

Available online at www.sciencedirect.com

SciVerse ScienceDirect

Procedia Engineering 00 (2012) 000–000

Procedia Engineering

www.elsevier.com/locate/procedia

5th BSME International Conference on Thermal Engineering

Heat Transfer from an Isothermally Heated Flat Surface Due to Twin Oblique Slot-Jet Impingement

Muhammad A.R. Sharif[a*]

[a]*Aerospace Engineering and Mechanics Department, The University of Alabama, Tuscaloosa, Alabama 35487-0280, USA*

Abstract

Impinging jets are used for quick and efficient cooling of heated surfaces. For normally impinging jets, one shortcoming is that high heat transfer is achieved only around the impingement region of the heated surface while the remaining parts of the surface under the wall jet region is subjected to significantly lower heat transfer rate. In order to achieve a more distributed heat transfer along an extended heated surface, the use of twin oblique impinging jets separated by a distance is proposed. In this study, convective heat transfer from a heated flat surface due to twin oblique laminar slot-jet impingement is investigated numerically. The flow domain is confined by an adiabatic surface parallel to the heated impingement surface. The twin slot jets are located on the confining surface. The flow and geometric parameters are the jet exit Reynolds number, distance between the two jets, distance between the jet exit and the impingement surface, and the inclination angle of the jet to the impingement surface. Numerical computations are done for various combinations of these parameters and the results are presented in terms of the streamlines and isotherms in the flow domain, the distribution of the local Nusselt number along the heated surface, and the average Nusselt number at the heated surface. It is found that for impingement angles up to 60°, the heat transfer is not desirably distributed. However, at 45° impingement angle, heat transfer is reasonably distributed with a corresponding decrease of about 36% overall heat transfer.

Keywords: Slot-jet impingement; Twin oblique jet impingement, Flat surface impingement; Convtictive heat transfer, Laminar flow

1. Introduction

Impingement flows are extensively used for heating, cooling, and drying processes in multifarious industrial applications due to their superior heat and mass transfer characteristics. The heat transfer coefficient for these typical applications using impingement jet is found to be higher than that of a cross circulation dryer for the same amount of gas flowing parallel to the target surface [1]. Hence, impinging jets are used in many industries where the thermal treatment of materials, cooling of electronic components and turbine blades, and drying of continuous sheets of materials, etc., is imperative. Some of the applications of dehydration impinging jets include manufacturing of printed wiring boards, production of foodstuffs, de-icing of aircraft wings, annealing of metal sheets, tempering of glass, etc.

Although, numerous studies have been conducted on impingement jets, it remains an active domain of research because of the complicated fluid dynamics involved. Polat et al. [2] published a comprehensive review on the numerical analysis of impinging jet flow and heat transfer prior to 1989. Among the recently published studies on jet impingement cooling, the works of Seyedin et al. [1], Morris et al. [3] Morris et al. [4], Cziesla et al. [5], Shi et al. [6], Sahoo and Sharif [7], Lou et al. [8] can be mentioned. This list, however, is not comprehensive by any means. Most of these published studies, experimental and/or numerical, investigated perpendicular single jet impingement on a stationery surface.

* * Corresponding author. Tel.: 1 205 348-8052; fax: 1-205-348-7240
E-mail address: msharif@eng.ua.edu

Nomenclature

c_p	specific heat at constant pressure
D_h	hydraulic diameter of the slot jet
H	normalized jet exit to impingement plate distance
K	thrmal conductivity
L	normalized distance between the inner edges of the twin jets
Nu	local Nusselt number
$\overline{\mathrm{Nu}}$	average Nusselt number
p	pressure
P	non-dimensional pressure
Pr	Prandtl number
Re	jet exit Reynolds number
T	fluid temperature
T_c	cold jet exit temperature
T_h	hot impingement wall temperature
U	non-dimensional velocity component in the x-direction
U_{in}	jet exit velocity
V	non-dimensional velocity component in the y-direction
W	slot-jet width
X	non-dimensional distance in the x-direction
Y	non-dimensional distance in the y-direction

Greek Letters

α	thermal diffusivity
φ	jet impingement angle
ρ	fluid density
μ	dynamic viscosity of the fluid
ν	kinematic viscosity
θ	non-dimensional temperature

Single impinging jets are efficient for localized heat transfer from the impingement location on a surface. For distributed cooling (or heating) of an extended surface, multiple impinging jets can be used. However, the flow physics for multiple impinging jets become very complicated due to the interaction of the spent fluid flow and impinging jet flow. For closely spaced multiple jets, the spent flow from upstream jet moves along the surface as a wall jet and behaves like a cross flow for the downstream impinging jet diverting the impingement process and degrading the heat transfer capability of the downstream jet. Gao and Sunden [9] reported 30% decrease of the stagnation point Nusselt number for the downstream jet. In some applications, it is desirable to recover the spent flow and recycle it as well. Thus the multiple confined impinging jet design needs to be modified with exhaust ports/slots either at the impingement plate or at the confining surface. Saad et al. [10] experimentally investigated multiple confined impinging slot-jet systems with jets and exhaust ports alternatively located on the confining wall. Tzeng et al. [11] experimentally and numerically investigated multiple confined impinging jet heat transfer with jet exhaust ports on the confining wall. Gao and Sunden [9] also experimentally investigated multiple slot jet impingement heat transfer under similar configurations. From these studies it is comprehended that multiple impinging jets with associated exhaust ports can be effective for achieving distributed heat transfer for an extended impingement surface. However, providing the exhaust ports and requiring a spent fluid recollection system makes the design and analysis much more complicated than the single jet impingement system. For some less demanding applications, symmetrical twin jets spaced sufficiently apart can also achieve reasonably distributed and effective heat transfer system. Aldabbagh and Sezai [12] numerically investigated the • flow and heat transfer characteristics of three-dimensional laminar square twin jets impinging on to a heated plane surface confined by a parallel surface. Abdel-Fattah [13] conducted numerical and experimental study of turbulent impinging circular twin-jet flow for isothermal case without any heat transfer. Ozmen [14] experimentally investigated the flow structure characteristics of a confined impinging twin jet for Reynolds numbers up to 50,000 at the various nozzle-to-plate spacing and jet-to-jet spacing without any heat transfer measurement.

It is conjectured that, even more distributed heat transfer is conceivable, if the symmetric twin *oblique* jets are used instead of the normal impinging jet. Several studies on single oblique impinging jets are available in the literature. Shi et al. [15] presented numerical study on heat transfer characteristics under normal and oblique semi-confined impinging slot-jet in the presence of cross-flow. Eren and Celik [16] experimentally investigated cooling of a heated flat plate by an obliquely

impinging slot-jet. Akansu et al. [17] performed an experimental study to determine the effects of inclination of an impinging two-dimensional slot-jet on the heat transfer from a flat plate. More recently, Parida et al. [18] conducted experimental and numerical investigation of confined oblique impingement configurations for high heat flux applications.

In this study, heat transfer from an isothermal hot surface due to symmetric twin oblique impinging jets in a confined domain in the laminar flow regime has been investigated numerically. This particular configuration of the jet impingement heat transfer research still remains relatively unexplored. The objective is to determine if this configuration results in more distributed heat transfer compared to the single normal jet impingement case.

2. Problem Description, and Boundary Conditions

The system of interest is a domain, confined by two parallel flat surfaces as shown in Fig. 1. The surface at the bottom is the impingement surface whose middle portion is the isothermal heat source maintained at a constant temperature T_h (301 K) and the outer portions are adiabatic. The confining parallel surface on top is adiabatic and contains the twin slot-jets. The cold jet exit temperature is T_c (300 K) and the exit uniform velocity is U_{in} impinging at angle φ onto the hot surface. The impingement angle, φ, is measured relative to the impingement surface as shown. For jets impinging normally onto hot surface, φ is set 90°. All geometric lengths are normalized by the hydraulic diameter of the slot, D_h, which for two-dimensional case with infinite span is twice the jet width, *W*. Thus the normalized width of each jet is 0.5. The normalized separation distance between the two surfaces is *H* and the normalized distance of separation between the inner edges of the twin slot-jets is *L*. The space between the two surfaces is filled with air (Pr = 0.71) as the working fluid. Because of symmetry, only the right half of the domain is considered for computation and symmetry conditions are imposed on the symmetry line. No slip condition is applied on all surfaces and pressure outlet condition is imposed at the outflow boundary.

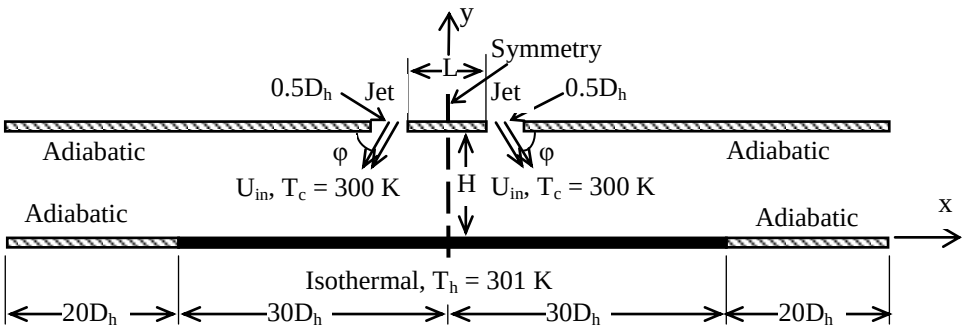

Fig. 1. Schematic of the flow geometry.

3. Mathematical Formulation and Numerical Procedure

The non-dimensional governing equations for the mass, momentum, and energy conservation are given as follows:

$$\frac{\partial U}{\partial X}+\frac{\partial V}{\partial Y}=0 \tag{1}$$

$$U\frac{\partial U}{\partial X}+V\frac{\partial U}{\partial Y}=-\frac{\partial P}{\partial X}+\frac{1}{\mathrm{Re}}\left(\frac{\partial^2 U}{\partial X^2}+\frac{\partial^2 U}{\partial Y^2}\right) \tag{2}$$

$$U\frac{\partial V}{\partial X}+V\frac{\partial V}{\partial Y}=-\frac{\partial P}{\partial Y}+\frac{1}{\mathrm{Re}}\left(\frac{\partial^2 V}{\partial X^2}+\frac{\partial^2 V}{\partial Y^2}\right) \tag{3}$$

$$U\frac{\partial \theta}{\partial X}+V\frac{\partial \theta}{\partial Y}=\frac{1}{\mathrm{Re\,Pr}}\left(\frac{\partial^2 \theta}{\partial X^2}+\frac{\partial^2 \theta}{\partial Y^2}\right) \tag{4}$$

The dimensionless variables for this problem are: $X=x/D_h$, $Y=y/D_h$, , $U=u/U_{in}$, $V=v/U_{in}$, $P=p/\rho U_{in}^2$, and $\theta=(T-T_c)/(T_h-T_c)$ where *x* and *y* are the distances along coordinate directions, *u* and *v* are the dimensional velocity components in the coordinate directions, *p* is the pressure, ρ is fluid density, and *T* is the fluid temperature. The non-dimensional parameters applied in the above formulations are; the Reynolds number, $\mathrm{Re}=U_{in}D_h/\nu$, and the Prandtl number, $\mathrm{Pr}=\nu/\alpha$ where ν and α are the kinematic viscosity and thermal diffusivity of the fluid, respectively. The computations are performed using the ANSYS Fluent V. 13 commercial CFD code [19]. Even though the Fluent code solves dimensional equations, setting the reference density ρ, reference velocity U_{in}, reference length D_h, specific heat at constant pressure c_p, and the temperature difference T_h-T_c, all equal to unity and choosing the viscosity μ as 1/Re, and the

thermal conductivity k as 1/RePr, the non-dimensional governing equations can be solved as dimensional equations. This is what is done in the computations for the present problem. The local Nusselt number on the hot surface is obtained from

$$\mathrm{Nu} = -\partial\theta/\partial Y \tag{5}$$

where Y is the non-dimensional normal distance from the surface. The average Nusselt number on the surface is calculated by integrating the local Nusselt number at the hot surface and then dividing it by the total length of the heated portion of the impingement surface.

A non-uniform finite volume mesh with collocated variable locations is used for the computations. The set of governing equations are integrated over the finite volumes, which produces a set of linear algebraic equations. The convection terms are discretized using the first-order upwind scheme whereas the diffusion terms are discretized using the central difference scheme. The pressure velocity coupling is treated using the well-known PISO method [20]. The set of algebraic equations for each variable are solved sequentially using an iterative method. The solution is considered converged when the normalized residual falls below 10^{-6} for the energy equation and below 10^{-4} for all other variables. The stricter convergence limit for the energy equation is required to ensure global heat balance. Additionally, the total heat flux at the hot impingement plate is also monitored until it became invariant with iteration.

4. Results and Discussion

Computations are performed for a jet exit Reynolds number of 1,000. The normalized separation distance between the two surfaces, *H*, is taken as 6 which puts the impingement surface just outside of the jet potential core region. A rectangular mesh clustered toward the walls with a bias factor of 50 is used in the *y*-direction. The region between the symmetry line and the right edge of the slot-jet in the *x*-direction is meshed with a uniform grid while the rest of the domain up to the outlet is meshed with an expanding grid using a bias factor of 30. A sample mesh is shown in Fig. 2. A systematic grid independence study is performed to obtain the required mesh resolution. The convergence of the local Nusselt number distribution at the hot impingement surface with mesh refinement is shown in Fig. 3. Starting with a coarse mesh (50x80), the grid is successively refined as (100x160) and (150x240). The computed local Nusselt number distribution is plotted from which it is noted that the change is insignificant for refinement beyond the 100x60 mesh. So this mesh is used for further computations.

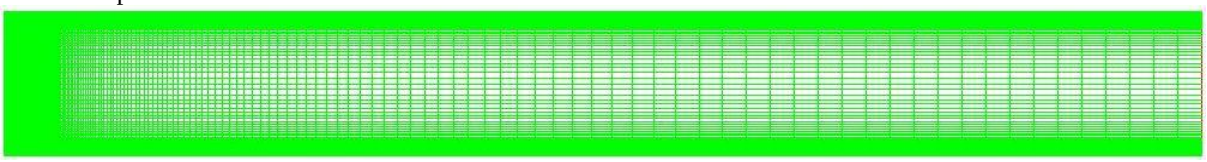

Fig. 2. Sample mesh for the right half of the domain.

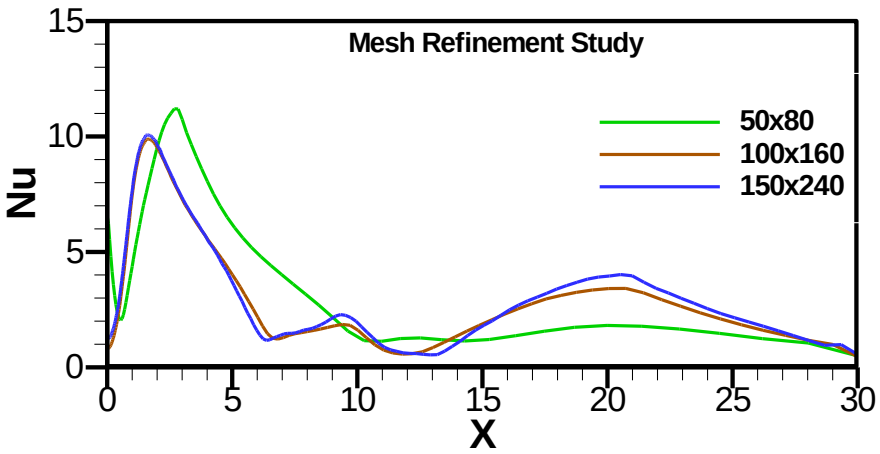

Fig. 3. Convergence of local Nusselt number distribution with mesh refinement.

Further computations are done by varying the impingement angle φ as 90°, 80°, 75°, 70°, 60°, and 45°. Fig. 4 shows the evolution of the streamline isotherm patters with the variation of the jet impingement angles. It is seen that the flow field is characterized by the formation of multiple recirculation bubbles in the domain. The main flow stream impinges on the target hot surface and then follows a meandering path in between the recirculation bubbles toward the outlet and then leaves the domain as a channel flow. Three major bubbles are formed; two on top between the confining wall and the main jet stream and one below between the impingement surface and the main jet stream. Another small clockwise rotating bubble forms, between the symmetry wall and the main jet stream, which grows in size as the impingement angle decreases. The isotherm patterns are compatible with the flowfield showing hot spots near the impingement surface and development of thin thermal boundary layer with large temperature gradients on the hot surface near the jet impingement region. This behaviour is manifested in peak local Nusselt numbers as will be seen later. The above trend continues until the impingement angle goes down to 60°. For φ = 45°, the flow pattern is significantly different. The minor bubble between the symmetry plane and the jet mainstream grows much larger and moves further downstream. The main jet stream is

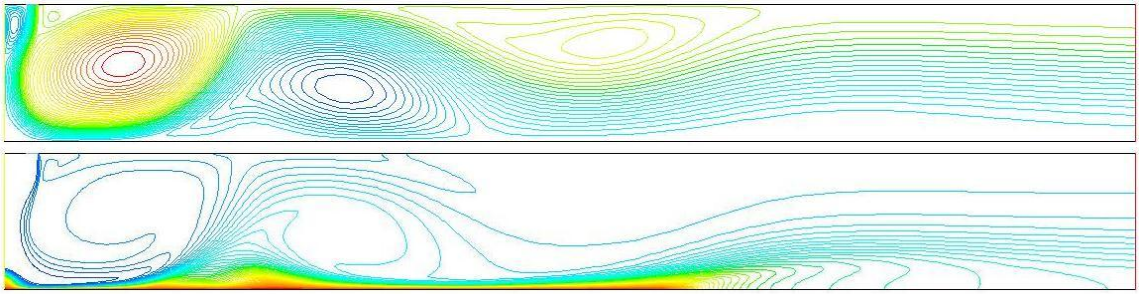

(a) $L = 2$, $\varphi = 90°$

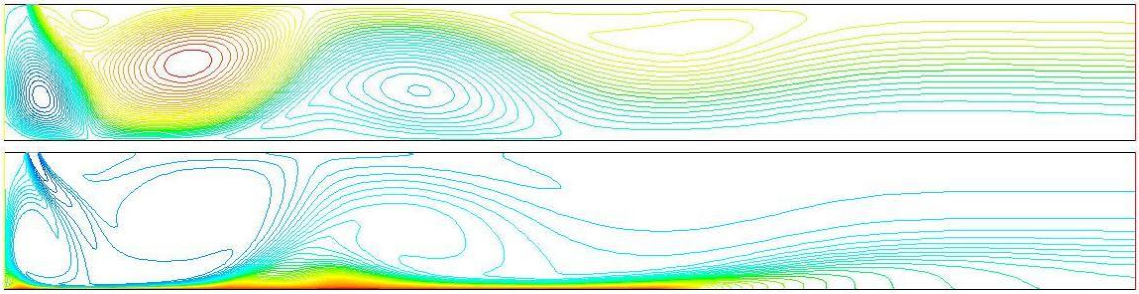

(b) $L = 2$, $\varphi = 75°$

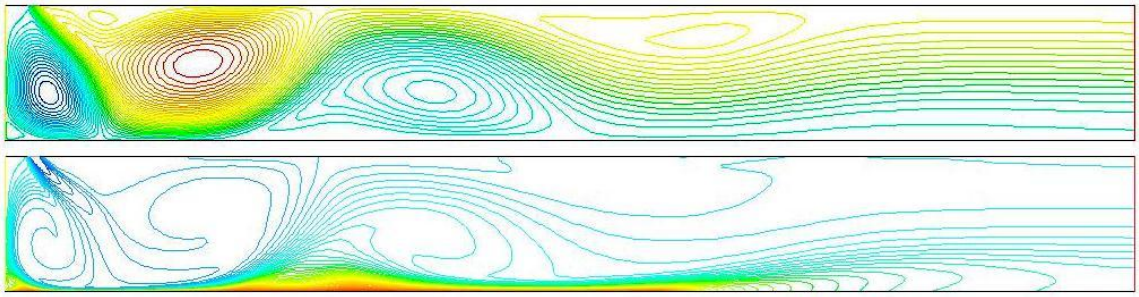

(c) $L = 2$, $\varphi = 60°$

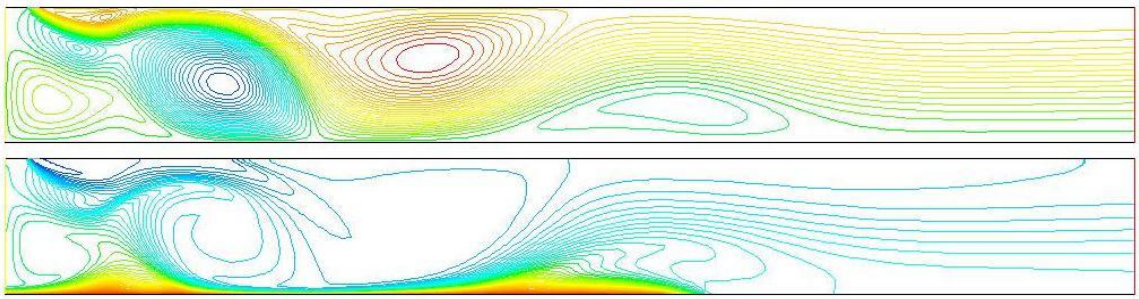

(d) $L = 2$, $\varphi = 45°$

Fig. 4. Streamlines and isotherms.

obstructed by this formation and surface impingement point moves further downstream. Two more minor recirculating bubbles are formed upstream closer to the symmetry plane and under the main jet stream. The first major recirculation bubble near the jet exit and above the main jet stream is now significantly squeezed into a smaller bubble and the second recalculating bubble between the main jet stream and the upper confining surface grows much larger in size and moves upstream. As for the isotherm plot, the thin boundary layer development occurs now over a larger portion of the impingement surface and is shifted downstream toward the jet impingement location.

In order to assess the heat transfer features of the associated impingement cooling processes the distribution of the local Nusselt number on the impingement surface is plotted in Fig. 5 for the above mentioned configurations. The peak Nusselt number remains nearly at 10 (with a slightly decreasing trend), but the peak location gradually shifts downstream as the impingement angle decreases until φ = 60°. For φ = 45°, however, the Nusselt number distribution is drastically different being more distributed with a peak value of about 5 occurring at a downstream location at around X = 13. It may be concluded from this local Nusselt number distribution pattern, that in order to achieve more distributed cooling of an isothermally hot surface by an impinging jet, impingement angles of the order of around 45° is needed. The overall heat transfer process is quantified by the average Nusselt number, $\overline{\mathrm{Nu}}$, at the hot surface, which is plotted in Fig. 6 versus the jet impingement angle φ. It is observed that the $\overline{\mathrm{Nu}}$ remains confined within 2 and 3 as the impingement angle varies. For normal impingement ($\varphi = 90°$), $\overline{\mathrm{Nu}}$ = 2.72, which then slightly increase to 3.15 at $\varphi = 80°$ and then gradually drops to 2.02 at $\varphi = 45°$. This indicates that the overall heat transfer is not largely affected by the jet impingement angle in the range 60° $\leq \varphi \leq$ 90°, and the local Nusselt number can be made more distributed with small sacrifice on the overall heat transfer (36%) making the jet impingement angle φ around 45°.

It needs to be mentioned here that the above findings cannot be claimed as a generalised characteristic because the local and global convection process largely depends on the various relevant parameters such as the jet exit Reynolds number, the jet-to-target surface separation distance, the separation distance between the twin jets, and above all, the oblique jet impingement angle. In this study only one particular combination of these parameters (Re = 1,000, H = 6, and L = 2) are considered except for varying impingement angle. Many other combinations of these parameters should be investigated before any conclusive generalization can be drawn.

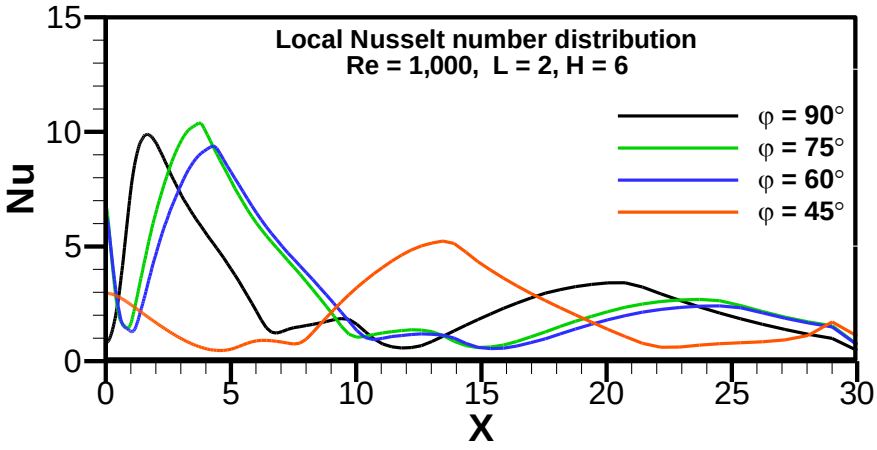

Fig. 5. Local Nusselt number distribution along the hot impingement surface.

5. Conclusions

Heat transfer form an isothermal hot surface confined by a parallel adiabatic wall due to twin oblique slot-jet impingement in the laminar flow regime is investigated numerically using the ANSYS Fluent CFD code [19]. The jet impingement angle is varied from 90° (normal impingement) to 45°. The streamline and isotherm patterns are presented and the local and average Nusselt number variations are plotted. The main objective of this study is to investigate if more distributed the heat transfer (cooling) from the impingement surface can be obtained using twin oblique slot-jets instead of a single normal impinging jet for which major cooling is concentrated near the impingement location on the surface only. Close examination of the local Nusselt number distribution and the average Nusselt number plots reveals that, this is achieved for an impingement angle around 45° yielding a peak local Nusselt number of about 5, but the overall heat transfer is reduced by about 36%. For impingement angles between 60° to 90°, while the overall heat transfer (average Nusselt number) remains fairly constant (3.2 to 2.8), the localized cooling is mainly concentrated around the impingement locations on the hot surface with a peak local Nusselt number of about 10.

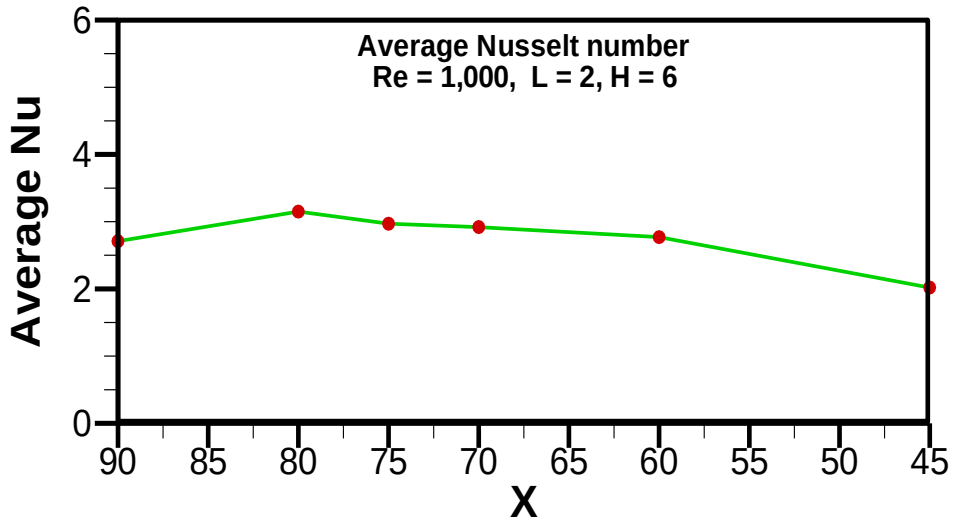

Fig. 6. Average Nusselt number variation at the hot impingement surface against impingement angle.

References

1. S.H. Seyedin, M. Hasan, A.S. Mujumdar, Turbulent flow and heat transfer from confined multiple impinging slot jets, Numerical Heat Transfer, Part A, 27 (1995) 35-51.
2. S. Polat, B. Huang, A.S. Mujumdar, W.J.M. Douglas, Numerical flow and heat transfer under impinging jets, Annual Review of Numerical Fluid Mechanics and Heat Transfer, 2 (1989) 157-197.
3. G.K. Morris, S.V. Garimella, R.S. Amano, Prediction of jet impingement heat transfer using a hybrid wall treatment with different turbulent Prandtl number functions, Journal of Heat Transfer, 118 (1996) 562-569.
4. G.K. Morris, S.V. Garimella, J.A. Fitzgerald, Flow-field prediction in submerged and confined jet impingement using the Reynold stress model, Journal of Electronic Packaging, 121 (1999) 255-262.
5. T. Cziesla, G. Biswas, H. Chattopadhyay, N.K. Mitra, Large-eddy simulation of flow and heat transfer of an impinging slot jet, International Journal of Heat and Fluid Flow, 22 (2001) 500-508.
6. Y. Shi, M.B. Ray, A.S. Mujumdar, Computational study of impingement heat transfer under a turbulent slot jet, Industrial and Engineering Chemistry Research, 41 (2002) 4643-4651.
7. D. Sahoo, M.A.R. Sharif, Numerical modeling of slot-jet impingement cooling of a constant heat flux surface confined by a parallel wall, International Journal of Thermal Sciences, 43 (2004) 877-887.
8. Z.Q. Lou, C. Yap, and A.S. Mujumdar, A Numerical study of a heat sink fin under a laminar impinging jet, Journal of Electronic Packaging, 130 (2008) 345011-345015.
9. X. Gao and B. Sundén, Experimental investigation of the heat transfer characteristics of confined impinging slot jets, Experimental Heat Transfer, 16 (2003) 1–18.
10. N.R. Saad, S. Polat, and W J M. Douglas, Confined multiple impinging slot jets without cross flow effects, International Journal of Heat and Fluid Flow, 13 (1992) 2-14.
11. P. Y. Tzeng, C. Y. Soong, and C. D. Hsieh, Numerical investigation of heat transfer under confined impinging turbulent slot jets, Numerical Heat Transfer, Part A, 35 (1999) 903-924.
12 L. B. Y. Aldabbagh and I. Sezai, Numerical simulation of three-dimensional laminar, square twin-jet impingement on a flat plate, flow structure, and heat transfer, Numerical Heat Transfer, Part A, 41 (2002) 835-850.
12. A. Abdel-Fattah, Numerical and experimental study of turbulent impinging twin-jet flow, Experimental Thermal and Fluid Science, 31 (2007) 1061–1072.
13. Y. Ozmen, Confined impinging twin air jets at high Reynolds numbers, Experimental Thermal and Fluid Science 35 (2011) 355–363.
14. Y.L. Shi, M.B. Ray, and A.S. Mujumdar, Numerical study on the effect of cross-flow on turbulent flow and heat transfer characteristics under normal and oblique semi-confined impinging slot jets, Drying Technology, 21 (2003) 1923-1939.
15. H. Eren and N. Celik, Cooling of a flat plate by an obliquely impinging slot jet, International Communications in Heat

and Mass Transfer, 33 (2006) 372-380.
16. Y.E. Akansu, M. Sarioglu, K. Kuvvet, and T. Yavuz, Flow field and heat transfer characteristics in an oblique slot jet impinging on a flat plate, International Communications in Heat and Mass Transfer, 35 (2008) 873–880.
17. P.R. Parida, S.V. Ekkad, and K. Ngo, Experimental and numerical investigation of confined oblique impingement configurations for high heat flux applications, International Journal of Thermal Sciences, 50 (2011) 1037-1050.
18. ANSYS FLUENT Computational Fluid Dynamics Code Version 13, ANSYS, Inc., http://www.ansys.com/.
19. R.I. Issa, Solution of the implicitly discretized fluid flow equations by operator splitting, Journal of Computational Physics, 62 (1986) 40-65.

Available online at www.sciencedirect.com

SciVerse ScienceDirect

Procedia Engineering 00 (2012) 000–000

Procedia Engineering

www.elsevier.com/locate/procedia

5th BSME International Conference on Thermal Engineering

Large Eddy Simulation of Vortex Shedding with Triangular Cylinder ahead of a Square Cylinder

Akshoy Ranjan Paul[a*], Shrey Joshi[b], Aman Jindal[b], Shivam P Maurya[c], Ajit Verma[c]

[a]*Department of Applied Mechanics,* [b]*Department of Mechanical Engineering,* [c]*Department of Chemical Engineering*
Motilal Nehru National Institute of Technology, Allahabad-211004, India.

Abstract

A two-dimensional Large Eddy Simulation (LES) is conducted for triangular rod ahead of a square cylinder at Reynolds Number, *Re* = 90,000. Vortex shedding is captured when two objects are kept at varying distance with different sizes of the upstream rod, the case under consideration are decided on the basis of the mode of flow (the cavity flow mode and the wake impingement mode) for d/D = 0.2 and 0.6 with L/D lying in various modes of flow. It is observed that the vortex shedding in cavity flow mode is much affected by the upstream rod such that the vortex shedding sometimes in very slightly affected by the shedding from the rear cylinder; whereas in wake impingement mode, the shedding is affected by both the objects. Hence, a superimposition of both the fluctuations is found behind the cylinder.

Keywords: Large eddy simulation (LES); Cavity flow mode (CFM); Wake impingement mode (WIM); vortex shedding; Fast Fourier transformation (FFT).

Nomenclature

C_L	Coefficient of lift, dimensionless
D	side of a square cylinder, cm
d	hydraulic diameter of triangular rod, cm
L	centerline distance between the cylinder and rod, cm
P	pressure, Pa
Re	Reynolds number, dimensionless
St	Strouhal number, dimensionless
t	time, s
u	velocity, m/s
x	direction of flow, cm
μ	dynamic viscosity of fluid, Ns/m^2
Greek symbols	
ρ	density of fluid, kg/m^3

1. Introduction

Flow past bluff bodies remain an area of concern for decades vastly due to the irregular behavior of turbulent vortex shedding behind the bodies, which is manifestation of the turbulence superimposed over periodic vortex shedding. A

* Corresponding author. Tel.: +91-532-227 1212;
E-mail address: arpaul2k@yahoo.co.in

number of computational fluid dynamics (CFD) simulations carried out for flow over bluff bodies using various turbulence models. Various methods of flow control have been applied to reduce drag over bluff bodies in past and one of them includes the use of control rods in front of the body to reduce drag. Igarashi, 1997 used this method to reduce the drag of the square prism. With a small upstream rod, the drag of the square rod was reduced at *Re* = 32,000. Zhang et al., 2006 conducted CFD analysis on circular cylinder in tandem arrangement where vortex shedding behind both the cylinders and their effect on each other were studied with variation in *L*/*D* and *d*/*D*. Vortex shedding characteristics are found to be highly dependent on these geometrical parameters. Moreover, the study distinguishes the behavior of vortex shedding in case of cavity flow mode (for lesser *L*/*D*) and wake impingement mode (for larger *L*/*D*).

Most of the previous studies on vortex shedding have been restricted to low *Re* as the vortex shedding in turbulent flow become highly complicated due to superimposition of turbulence over the periodic shedding. Ferziger, 1990 and Rodi, 1991 showed that the Reynolds Averaged Navier-Stokes (RANS) based CFD code, which uses statistical turbulence models to predict turbulence does not readily capture both periodic shedding and turbulence accurately. The frequency ranges for turbulence together with periodic shedding is large and Direct Numerical Simulation (DNS) is the best way to predict the flow characteristics. However, huge computational cost and time is involved with DNS, which often restricts its use in these cases. Hence, a midway approach called the Large Eddy Simulation (LES) is adopted for this purpose that uses near-wall turbulence models and simulates rest of the flow. LES with extreme fine resolution near the solid boundary (wall) could fetch results as good as a DNS method. The purpose of fine resolution is to avoid leaving the utmost important near-wall region to statistical models or to the so-called 'law of wall'. Hence, the LES model with fine near-wall resolution has a potential to provide accurate computational results. LES model is generally used to predict three-dimensional turbulence. However, Bouris et al., 1999 shows that the quasi two-dimensional turbulence behind the square cylinder is much more accurately resolved with two-dimensional LES as compared to the three-dimensional LES. This does not necessarily imply that the three-dimensionality of turbulence is under question, but rather the present study and the objective are well fetched using two-dimensional LES.

Previous studies on vortex shedding from cylinder in tandem arrangement mainly discussed the effect of vibrations and fluctuations on one another, which are largely done with similar shaped (i.e. circular-circular or square-square) objects arranged in tandem or staggered formation. But the open literature lacks the in-depth study of vortex shedding with dissimilar objects in tandem arrangement. The present study is therefore, attempted to observe the nature of fluctuation when a triangular shaped object (called upstream rod) lies ahead of a square cylinder in flow stream.

2. Computational Methodology

The present study has been conducted at *Re* = 90,000 with a triangular rod ahead of a square cylinder. The computation is conducted on finite-volume technique based commercially available CFD code Fluent 6.3 using two-dimensional LES, which tracks the larger eddies and involves space filtering of unsteady Navier-Stokes equation. These unsteady filtered equations are solved using sub-grid scale models. Fig 2 shows the grid used for the analysis with a triangular cylinder ahead of a square cylinder.

2.1. Geometry and Computational Domain

A Rectangular box of dimension 180×90cm^2 is used as computational domain. A triangular cylinder of varying size ahead of a square cylinder of 10×10 cm^2 cross section is taken. Triangular cylinder is placed 20 cm downstream of the inlet. For properly capturing the wake region of the cylinder the domain has been extended behind the cylinder nearly up to 10 times of the cylinder dimensions as shown in Fig 1, *D* is the side of the square cylinder.

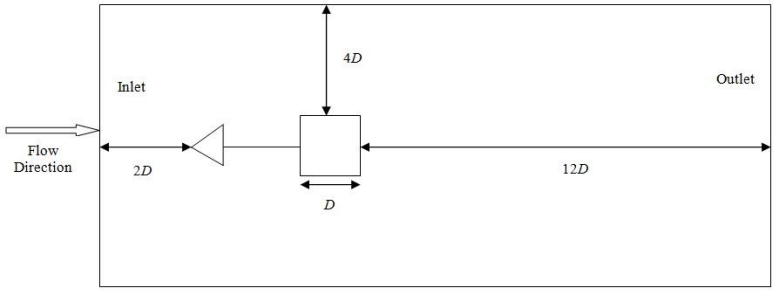

Fig. 1 Schematic diagram of cylinder and rod arrangement in a computational domain

2.2. Grid Generation

Commercial Software Gambit 2.4 is used for grid generation of the problem. In order to obtain a major part of the computational domain as a structured mesh, quad sub-map and tri primitive meshing is used. Number of cells generated are about 1,20,000. The grid independency test is an important part in CFD but is not included here since LES model is highly dependent on the amount of fineness of the grid, keeping first grid points at y+=1 the accuracy is kept highest, hence more fine grid would have resulted in larger computational cost with almost similar accuracy.

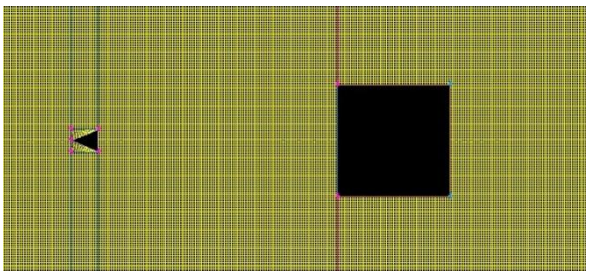

Fig. 2 Grid generation around the square cylinder and the triangular rod

2.3. Governing equations

The governing equations for the present problem are the two-dimensional continuity, momentum equations for steady-state flow, and can be written as follows:

Continuity equation:

$$\frac{\partial \rho}{\partial t} + \frac{\partial (\rho u_i)}{\partial x_i} = 0 \tag{1}$$

Momentum equation:

$$\frac{\partial}{\partial t}(\rho u_j) + \frac{\partial}{\partial x_i}(\rho u_i u_j) = \frac{\partial}{\partial x_i}\left(\mu \frac{\partial u_j}{\partial x_j} \right) - \frac{\partial p}{\partial x_j} \tag{2}$$

The LES uses space filtering of Navier Stokes (momentum equation) equation which is defined as to decompose the velocity into the sum of filtered (resolved) component and a residual that arises due to the unresolved sub-grid scales, the closure is obtained by modelling the residual stress tensor by a simple eddy viscosity model.

2.4. Boundary Conditions

The boundary conditions include the no-slip wall conditions on the edges of both the cylinders and an inlet velocity of 15 m/s from the left face of the domain and zero gauge pressure at exit.

2.5. Solution Methodology

The segregated and implicit solver is selected for discretization of governing equations. The SIMPLE algorithm (Patankar, 1980) is used for the pressure-velocity coupling. PRESTO (Pressure staggering option) is selected for discretizing pressure, whereas, bounded central differencing numerical scheme is chosen for discretizing momentum equations. Convergence criterion for continuity and velocity is taken as 10^{-4}. The computational work has been performed on an IBM workstation with 8 GB RAM and Intel Xeon processor. A typical run time for the CFD simulation was approximately 12 hours.

3. Computational Analysis

The various cases under consideration were decided on the basis of the study of drag for various L/D and d/D as well as the past research which points out to the dependence of vortex characteristics over the spacing between cylinders, two hydraulic diameters for the triangular rod were considered namely d/D= 0.2 and 0.6, and the spacing considered were according to the region in which the spacing lies i.e. either wake impingement mode or in cavity flow mode, so as to capture and study the interaction between the pair of standing vortices from rod and their interaction with the vortices from the cylinder, due to the high computational cost required for Large Eddy Simulations the number of cases are to be as minimum as possible but enough to provide an understanding of the flow characteristics , Zhang et al., 2006 shows that the nature of vortex shedding remains almost similar within a particular mode of flow irrespective of the size of rod, the study involves d/D=0.05 and 0.5, the fluctuation of lift due to vortex shedding might have differ in magnitude but is similar in nature as far as the spacing L/D lies in one mode of flow. The observation in Zhang et al.,2006 has been used in the present study to minimize the number of cases ,hence for d/D=0.2 the flow in wake impingement mode is taken under consideration for L/D>2.7(critical spacing ration =2.7) once a behavior was observed in wake impingement mode the next objective is to analyze the behavior in the cavity flow mode which is fulfilled by placing the rod with d/D=0.6 at lesser than critical length, overall 4 cases have been considered with d/D=0.2 where L/D was kept at 4.5(wake impingement mode) and at 2.7 (critical length) and with d/D=0.6 where L/D was kept at 1.5 and at 2.7 (both cavity flow mode).

4. Results and Discussion

The graphs for C_L versus time is shown in Fig 3, the rod with d/D=0.6 and L/D =2.7 lies near the critical length, the fluctuations of the rod and the cylinder are well in correlation in case of critical length.

The vortex shedding in the two modes varies a lot, the amplitude spectrum versus. Frequency (FFT) shows that there are single frequency fluctuations for rod and cylinder in CFM such that the pair of standing vortex from rod are temporally synchronized with cylinder vortices. Whereas in wake impingement mode the pair of standing vortex are not synchronized leading to two frequency one from the rod and other the consequence of superimposition of cylinder fluctuation by the rod vortices.

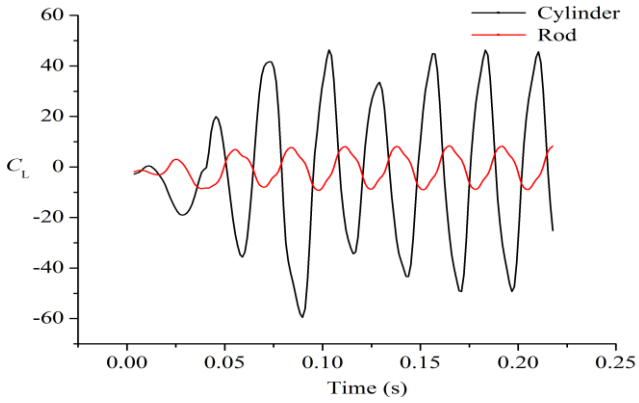

Fig. 3 C_L versus time for d/D=0.6 and L/D=2.7 (nearest critical length)

In CFM the graph shown in Fig 4-5 shows that both the objects have one vibrational frequency which is adjusted such that the Strouhal numbers (St) are equal as in table.1, this shows that the vortex shedding from the rod are synchronized with the cylinder periodic shedding the contour in Fig 10 shows that the when the rod is placed close to the cylinder the vortex shedding from the rod is not disturbed by the cylinder but instead a similar shedding is behind the cylinder itself that creates a symmetric shedding where the field is nor as distorted as in Fig 9. Whereas, in case of WIM, Fig 9 shows that the shedding from the rod is not synchronized with the shedding from the cylinder. Hence it creates a distorted field behind the cylinder owing to the unsynchronized superimposition of the two periodic fluctuations (one from the rod and other from the cylinder).

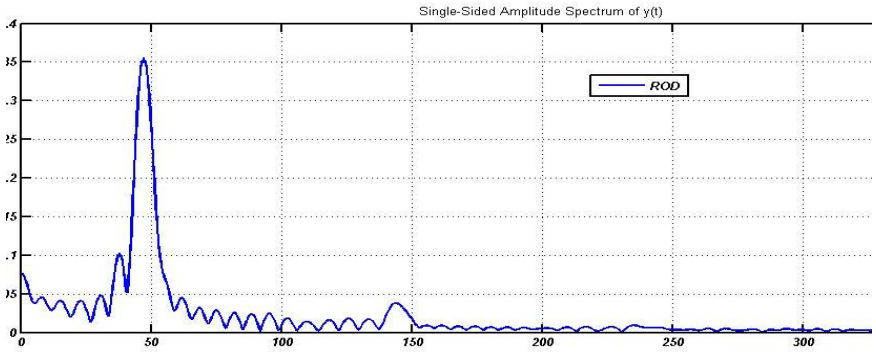

Fig. 4 Amplitude spectrum versus frequency for rod (d/D=0.6 & L/D=1.5, CFM)

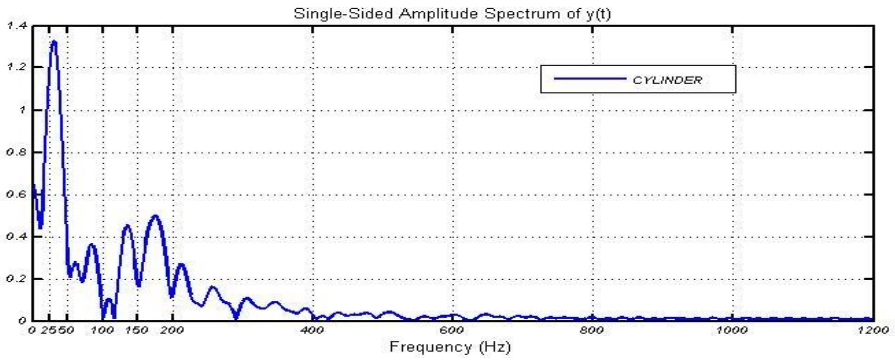

Fig. 5 Amplitude spectrum versus frequency for cylinder (d/D=0.6 & L/D=1.5, CFM)

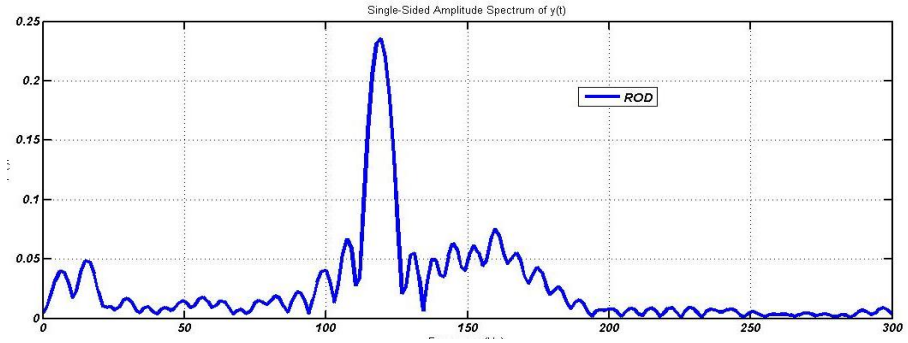

Fig. 6 Amplitude spectrum versus frequency for rod (d/D=0.2 & L/D=4.5, WIM)

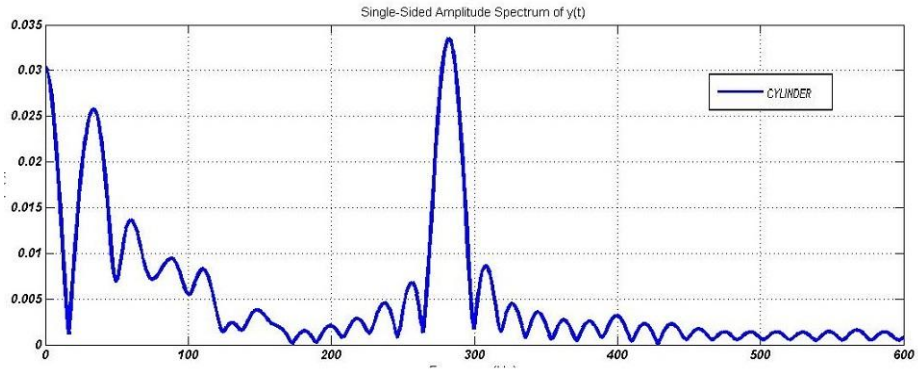

Fig. 7 The graph shows the amplitude spectrum versus frequency for cylinder (d/D=0.2 & L/D=4.5, WIM)

Table 1 Values of Strouhal number (*St*) for various cases

	***d*/*D*=0.2, *L*/*D*=4.5**	***d*/*D*=0.2, *L*/*D*=2.7**	***d*/*D*=0.6, *L*/*D*=1.5**	***d*/*D*=0.6, *L*/*D*=2.7**
Rod	0.183	0.183	0.183	0.184
Cylinder	0.187 and 0.935	0.185 and 0.371	0.185	0.181

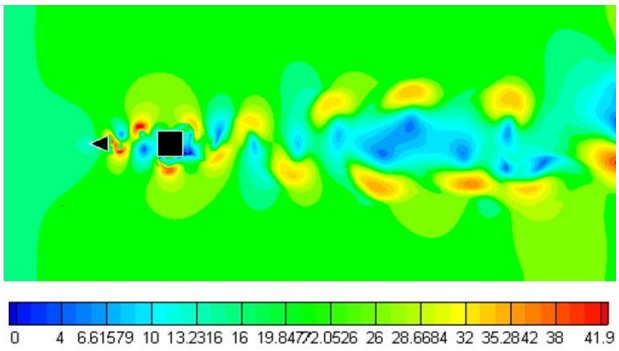

Fig. 8 Velocity contours for the case lying near the critical length (*d*/*D*=0.6, *L*/*D*=2.7)

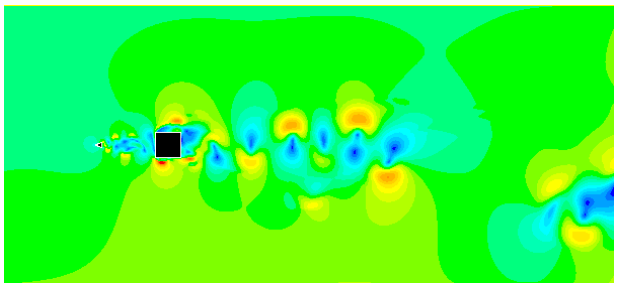

Fig. 9 Velocity contours for the case lying in the WIM (*d*/*D*=0.2, *L*/*D*=2.7)

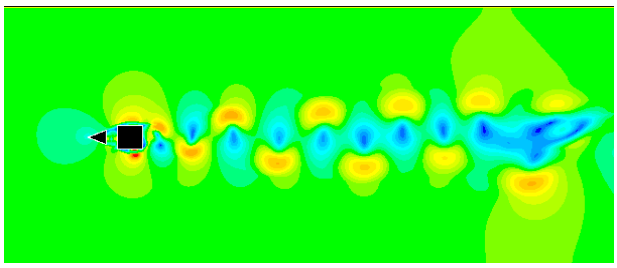

Fig. 10 Velocity contours for the case lying in the CFM (*d*/*D*=0.6, *L*/*D*=1.5)

The fluctuations in Fig 10 are highly synchronized since the cylinder-rod arrangement lies in the CFM. But in Fig 8, the arrangement lies at the critical length where the two modes (CFM and WIM) meet and hence, the shedding behind the cylinder seems to be little synchronized. The distortion is however noticed in Fig.8 in the flow downstream. In Fig 9, the fluctuations from the rod are superimposed over the cylinder fluctuation in such a way that they tend to distort the flow field further, and the wake pattern is no longer synchronized.

5. Conclusions

The computational study conducted could be summarized in the following conclusions

- The vortex shedding in turbulent flow is a highly complex phenomenon since periodic shedding is superimposed by the turbulent fluctuations leading to difficulties in resolving the flow parameters. The use of RANS technique has

been found futile in the past since it cannot capture both properly hence the midway approach Large Eddy Simulation (LES) is used with fine meshing to resolve results with high accuracy.

- The analysis shows that the shedding characteristics largely depend on the spacing and the size of upstream rod. In the CFM, the fluctuations from the rod are synchronized with the fluctuation from the cylinder leading to a single fluctuation frequency in both the cylinder and the rod whereas in case of WIM, the fluctuations from the rod are not synchronized with the cylinder fluctuation leading to two fluctuation frequencies for the cylinder.

References

[1].Igarashi T., 1997, Drag reduction of a square prism by flow control using a small rod, J. of Wind Engineering and Industrial Aerodynamics, vol. 67, pp-141-153.

[2] Zhang P.F., Wang J.J., Huang L.X., 2006, Numerical simulation of flow around cylinder with an upstream rod in tandem at low Reynolds numbers, J. of Applied Ocean Research, vol. 28, pp-183–192.

[3] Ferziger J.H., 1990, Approaches to turbulent flow computation: application to flow over obstacle, J. of Wind Engineering and Industrial Aerodynamics, vol. 35, pp-1-19.

[4] Franke R., Rodi W., 1991, Calculation of vortex shedding past a square cylinder with various turbulence models, Proc. 8th symposium on Turbulent shear flow, Technical University Munich, Springer Berlin, pp-189-204.

[5] Bouris D., Bergeles G., 1999, 2D LES of vortex shedding from a square cylinder, J. of Wind Engineering and Industrial Aerodynamics, vol. 80, pp-31-46.

[6] Patankar S.V., 1980, Numerical Heat Transfer and Fluid Flow, Taylor and Francis Publication, London.

Available online at www.sciencedirect.com

SciVerse ScienceDirect

Procedia Engineering 00 (2012) 000–000

Procedia Engineering

www.elsevier.com/locate/procedia

5th BSME International Conference on Thermal Engineering

Influence of waste granite powder on thermal conductivity of particulate epoxy composites

Arun Kumar Rout[a]*, Purna Chandra Mishra[b], Ashok Kumar Sahoo[b], Susant Kumar Sahu[b]

[a]*Department of Mechanical Engineering, Motilal Nehru National Institute of Technology, Allahabad, 211004, India*
School of Mechanical Engineering, KIIT University, Bhubaneswae, 751024, India

Abstract

This paper describes the development and thermal characterization of a new class of epoxy composites filled with different volume proportions (Φ) of granite particulates. The objective of the present work is to fabricate low cost epoxy based composites filled with five volume proportions (0, 2.7, 6.4, 12.5 and 21.6 vol.%) of granite particulates and to study its effect on the thermal conductivity of epoxy resin. Finite element method (FEM) is implemented to determine the effective thermal conductivity numerically and is validated with the existing theoretical models followed by experiment. A comparison of conductivity between the unfilled and filled samples has been presented. A commercially available finite-element package ANSYS is used for the numerical analysis. Three-dimensional cubes-in-cube lattice array models are constructed to simulate the microstructure of the composite material for various filler concentrations ranging from about 0 to 21.6 vol.%. Guarded heat flow meter test method is used to measure the thermal conductivity of these composites as per the ASTM standard. It is observed that the incorporation of granite results in enhancement of conductivity of epoxy resin and thereby improves its thermal conductivity capability. With addition of 2.7 vol.% of granite powder, the effective thermal conductivity of epoxy is found to increase by about 5% and with addition of 21.6 vol.%, the conductivity improves by about 50%. The experimentally measured conductivity values are compared with the numerically calculated ones and also with the existing theoretical and empirical models. The values obtained using finite element method is found to be in reasonable agreement with the experimental values.

Keywords: Epoxy matrix; Granite powder; Finite element method; Effective thermal conductivity

1. Introduction

In the development of a new polymer matrix composite, it is necessary to know about its thermal, mechanical and other properties before any specific application. Being light weight they are the most suitable materials for weight sensitive applications, but their high cost sometimes restricts for general applications. Use of low cost, easily available fillers is therefore useful to improve such properties and to lower the overall cost of components [1,2]. These properties of the composite mainly depends upon the nature of particle-matrix interface, dispersion of particles in the matrix, filler volume fraction, type of filler etc. A review of literature shows that considerable work has been reported on the subject of heat conductivity in polymers [3,4]. There are many interesting reports are available in the existing literature on experimental as well as numerical and analytical studies on thermal conductivity of some filled polymer composites [5-7]. Procter and Solc [8] have used Nielsen model as a prediction to investigate the thermal conductivity of several types of polymer composites filled with different fillers and confirmed its applicability. Zhao et al.[9] have studied the thermal stability and flammability of rice husk filled high-density polyethylene eco-composites. They observed that the addition of rice husk effectively reduces the thermo-oxidation process of the composite by about 40^0C because of silica content in rice husk. Nayak et al.[10] have evaluated the effective thermal conductivity of pine wood dust filled epoxy composites by numerically and

* Corresponding author. Tel.: +91-9439301549; fax: +0-000-000-0000 .
E-mail address: arun.rout.6314@gmail.com

experimentally. Similarly, Rout and Satapathy [11] have studied the effect of thermal insulation capabilities of rice husk filled epoxy composites. They found that the effective thermal conductivity these composites are reducing with filler addition. Yung et al. [12] have evaluated experimentally thermal properties of epoxy matrix filled with hollow glass microsphere (HGM). They observed that the thermal conductivity, coefficient of thermal expansion, glass transition temperature and dielectric properties are reducing with addition of HGM. Tognana et al. [13] have developed an optical dilatometer to measure the thermal property such as coefficient of thermal expansion of alumina powder filled epoxy composites.

Many theoretical and empirical models have been proposed to predict the effective thermal conductivity of two-phase mixtures. The applicability of these models has been reviewed by Ishida and Rimdusit [5] and Ott [14]. Sweeting and Liu [15] have developed a model to measure thermal conductivity in three principal directions of a composite lamina. Similarly, Bagchi and Nomura [16] have developed a theoretical model for predicting effective thermal conductivity of an aligned multi-wall nano-tube polymer composite. For a two-phase polymer composite, the simplest alternatives would be with the materials arranged in either parallel or series with respect to heat flow, which gives the upper or lower bounds of effective thermal conductivity. For the parallel conduction model: $k_c = (1-\Phi)k_m + \Phi k_f$ (1)

where, k_c, k_m and k_f are the thermal conductivities of the composite, the matrix and the filler respectively and Φ is the volume fraction of filler. For the series conduction model:

$$\frac{1}{k_c} = \frac{(1-\Phi)}{k_m} + \frac{\Phi}{k_f} \quad (2)$$

The correlations presented by equations (1) and (2) are derived on the basis of the Rules of Mixture (ROM). in case of geometric mean model, the effective thermal conductivity of the composite is given by

$$k_c = k_f^{\Phi} \times k_m^{1-\Phi} \quad (3)$$

Using potential theory, Maxwell [17] obtained a simple relationship for conductivity of randomly distributed and non-interacting homogenous spheres in a homogenous medium:

$$k_c = k_m \times \left[\frac{k_f + 2k_m + 2\Phi(k_f - k_m)}{k_f + 2k_m - \Phi(k_f - k_m)} \right] \quad (4)$$

This model predicts fairly well effective thermal conductivities at lower filler concentrations, whereas for high filler concentrations, particles touch each other and form conductive chains in the direction of heat flow and therefore this model underestimates the value of effective thermal conductivities in this region.

Review of literature shows that a large number of particulates have been used as fillers in the past; however, there is no such report available on industrial waste materials like granite powder being used to study the thermal characteristics. Granite is an igneous hard rock with 53.1% SiO_2, 14.1% Fe_2O_3, 12.3% Al_2O_3 and other ceramic oxides by weight [18]. It has high strength, stiffness and better thermal properties. Further, granite powders are the waste largely available in stone crushers and in granite stone mines and these powders not only cause environmental pollution but also trigger health problems to mankind. Besides, though it becomes clear that improved thermal conductivity in polymers may be achieved either by molecular orientation or by the addition of conductive fillers, it is yet to be seen how the incorporation of granite particulates will affects the overall conductivity of the polymer composite. In view of the above, the present work is undertaken to investigate the thermal conductivity of epoxy matrix filled with granite particulates.

2. Experimental details

2.1 Materials

Epoxy LY 556 resin, chemically belonging to the 'epoxide' family is used as the matrix material. Its common name is Bisphenol A Diglycidyl Ether. The low temperature curing epoxy resin (Araldite LY 556) and corresponding hardener (HY951) are mixed in a ratio of 10:1 by weight as recommended. The epoxy resin and the hardener are supplied by Ciba Geigy India Ltd. Epoxy is chosen primarily because it happens to be the most commonly used polymer and because of its insulating nature (low value of thermal conductivity, about 0.363 W/m K). Granite powder is chosen for filler material as it has thermal conductivity of 2.36 W/m.^{0}C, density of 2.59 kg/m^3 and coefficient of thermal expansion of 9.54×10^{-6}/ ^{0}C at 100^{0}C[19]. Moreover, it is renewable, available at low cost and basically the granite powder is considered as a waste product. The powder is collected from School of Sculpture, KIIT University, Bhubaneswar, India.

2.2. Composite fabrication

The low temperature curing epoxy resin (LY 556) and corresponding hardener (HY951) are mixed in a ratio of 10:1 by weight as recommended. Granite particles are reinforced in epoxy resin (density 1.1 gm/cc) to prepare the composites. The dough (epoxy filled with granite) is then slowly decanted into the glass tubes, coated beforehand with wax and uniform thin film of silicone-releasing agent. The composites are cast by conventional hand-lay-up technique in glass tubes so as to get cylindrical specimens (diameter 30 mm, length 100mm). Composite samples of five different compositions, as listed in Table 1 are made. The mean particle size of granite used for preparing the samples is 100 micron. The castings are left to cure at room temperature for about 24 hour after which the tubes are broken and samples are released. Specimens of suitable dimension are cut using a diamond cutter for further physical characterization and thermal conductivity test.

Table 1. List of composite fabricated

Designation	Composition
C1	Epoxy + 0% (vol.)
C2	Epoxy + 2.7% (vol.) Granite Powder
C3	Epoxy + 6.4% (vol.) Granite Powder
C4	Epoxy + 12.5% (vol.) Granite Powder
C5	Epoxy + 21.6% (vol.) Granite Powder

2.3. Experimental determination of thermal conductivity

Unitherm™ Model 2022 is used to measure thermal conductivity of a variety of materials. These include polymers, ceramics, composites, glasses, rubbers, some metals, and other materials of low to medium thermal conductivity. Only a relatively small test sample is required. Non-solids, such as pastes or liquids, can be tested using special containers. Thin films can also be tested accurately using a multi-layer technique. The tests are in accordance with ASTM E-1530 standards.

3. Numerical analysis: Concept of finite element method

The finite element method (FEM), originally introduced by Turner et al. 1956 [20], is a powerful computational technique for approximate solutions to a variety of ‘‘real-world” engineering problems having complex domains subjected to general boundary conditions. FEA has become an essential step in the design or modeling of a physical phenomenon in various engineering disciplines. A physical phenomenon usually occurs in a continuum of matter (solid, liquid, or gas) involving several field variables. The field variables vary from point to point, thus possessing an infinite number of solutions in the domain. The basis of FEM relies on the decomposition of the domain into a finite number of sub-domains (elements) for which the systematic approximate solution is constructed by applying the variational or weighted residual methods. In effect, FEM reduces the problem to that of a finite number of unknowns by dividing the domain into elements and by expressing the unknown field variable in terms of the assumed approximating functions within each element. These functions (also called interpolation functions) are defined in terms of the values of the field variables at specific points, referred to as nodes. Nodes are usually located along the element boundaries, and they connect adjacent elements. The ability to discretize the irregular domains with finite elements makes the method a valuable and practical analysis tool for the solution of boundary, initial, and eigenvalue problems arising in various engineering disciplines. The FEM is a numerical procedure that can be used to obtain solutions to a large class of engineering problems involving stress analysis, heat transfer, fluid flow etc. ANSYS is general-purpose finite element modeling package for numerically solving a wide variety of mechanical problems that include static/dynamic, structural analysis (both linear and nonlinear), heat transfer, and fuid problems, as well as acoustic and electromagnetic problems.

4. Results and discussion

4.1. Numerical analysis

Using the finite element program ANSYS, thermal analysis is carried out for the conductive heat transfer through the composite body. In order to make a thermal analysis, three-dimensional physical models with cubes-in-a-cube lattice array have been used to simulate the microstructure of composite materials for five different filler concentrations. Cubical structure of granite particles is assumed as these structures are similar to the actual sieved granite particulates. Further, the effective thermal conductivities of these epoxy composites filled with granite powder up to about 21.6 % by volume is numerically determined using ANSYS.

4.2. Description of the problem

The important factors that influence the effective properties and can be controlled to an appreciable extent is the microstructure of the composite. Here, microstructure means the shape, size distribution, spatial distribution and orientation

distribution of the reinforcing inclusion in the matrix. Although most composite possess inclusion of random distributions, great insight of the effect of microstructure on the effective properties can be gained from the investigation of composites with periodic structure. System with periodic structures can be more easily analyzed because of the high degree of symmetry embedded in the system. In the numerical analysis of the heat conduction problem, the temperatures at the nodes along the surfaces ABCD is prescribed as $T_1=100^0$C and the convective heat transfer coefficient of ambient is prescribed as 2.5 W/m^2 K at ambient temperature of 27^0C. The heat flow direction and the boundary conditions are shown in Fig.1. The other surfaces parallel to the direction of the heat flow are all assumed adiabatic. The finite element analysis is carried out with cubes-in-cube square periodic array. The cube is assumed as 1mm side length and cubical granite particulates of 100 micron diameter. 8-noded SOLID 70 element is taken with element size of 6 for the present static thermal analysis as shown in Fig. 2. A temperature profile is obtained in ANSYS with the initially assumed value of conductivity. Then the process is iterated till convergence. The temperatures at the nodes in the interior region and on the adiabatic boundaries are unknown. These temperatures are obtained with the help of finite-element program package ANSYS. In the analysis of the ideal case it is assumed that the matrix and filler of the composites are macroscopically homogeneous and isotropic, the thermal contact resistance between the filler and the matrix is negligible, the composite lamina is free of voids and the filler are arranged in a square periodic array/uniformly distributed in matrix. Thermal conductivities of epoxy composites filled with granite particles up to 21.6% by volume are numerically estimated by using the cubes-in-cube model and the numerical results are compared with the experimental results and also with some of the existing theoretical and empirical models. A typical three-dimensional cube-in-cube model with a body centered cubic (BCC) structural arrangement for the composite with granite concentration of 6.4 vol. % is illustrated in Fig. 3. The temperature profiles obtained from FEM analysis for the composites with particulate concentrations of 0, 2.7, 6.4, 12.5 and 21.6 vol% are presented in Figs. 4(a) to 4(e) respectively. It is observed that the temperature difference between the two surfaces is reducing with granite addition and therefore the effective conductivity of the composite is increasing with filler addition.

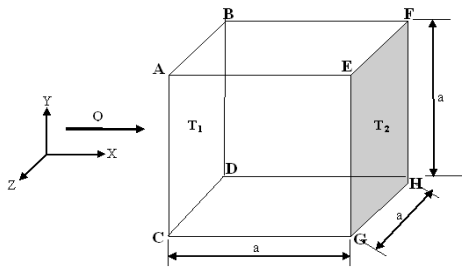

Fig. 1 Heat flow direction and the boundary conditions

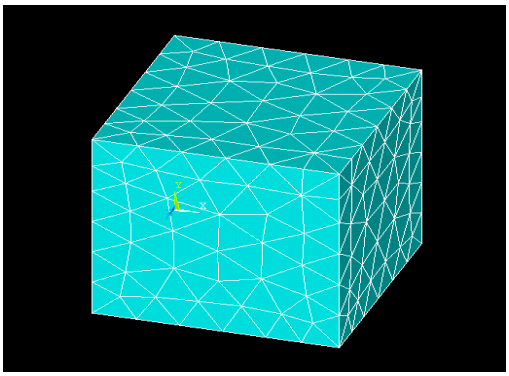

Fig. 2 Meshing with 8-noded SOLID 70

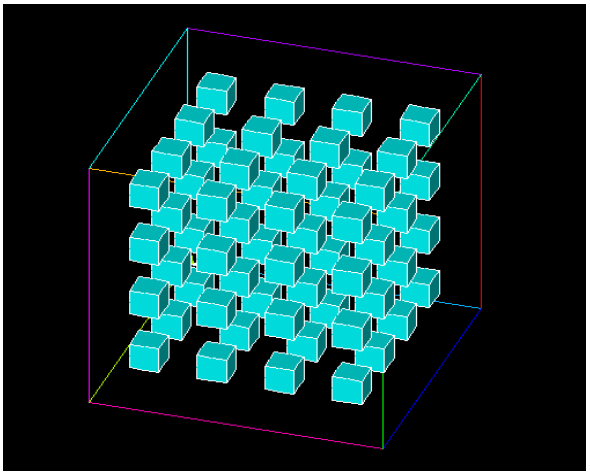

Fig.3 A typical cube-in-cube model for particle concentration of 6.4 vol%.

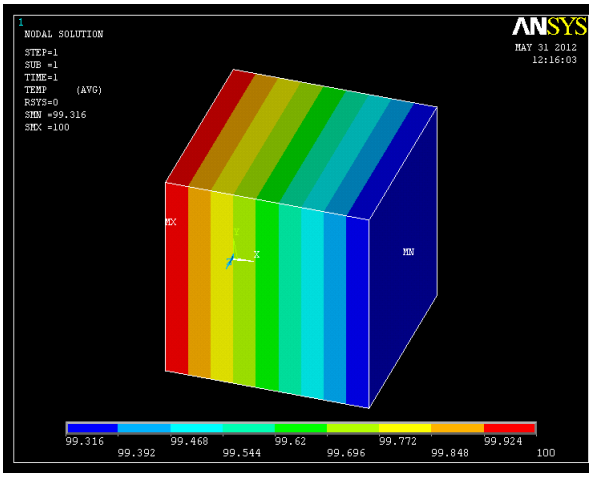

Fig. 4(a) Temperature profile for composite with particle concentration of 0 vol%.

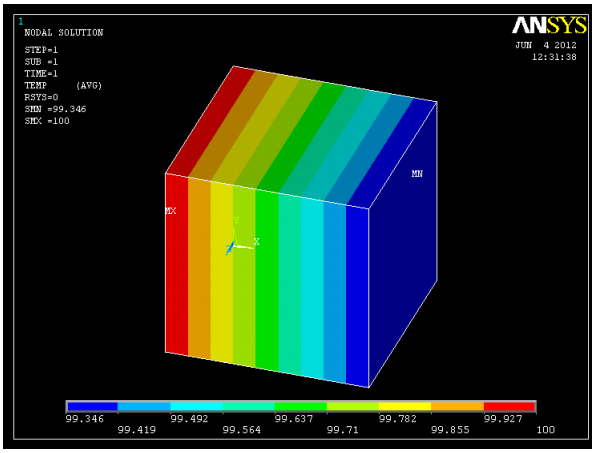

Fig.4(b) Temperature profile for composite with particle concentration of 2.7 vol% granite

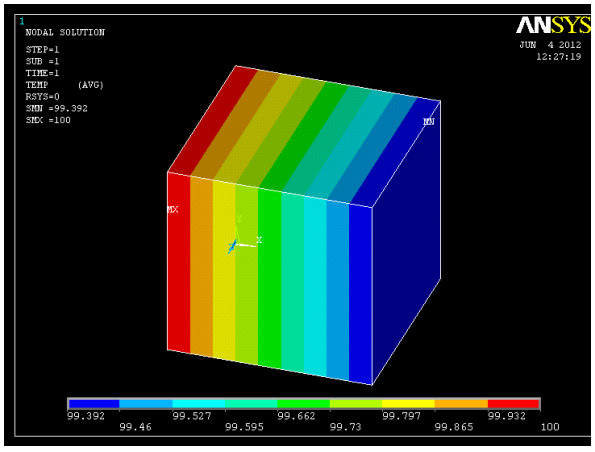

Fig.4(c) Temperature profile for composite with particle concentration of 6.4 vol% granite

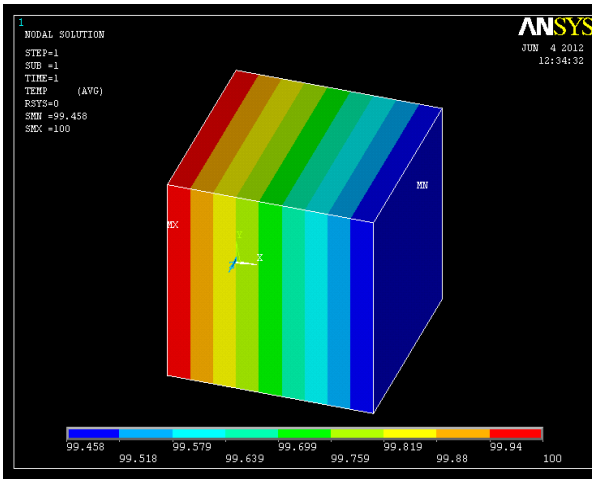

Fig.4(d) Temperature profile for composite with particle concentration of 12.5 vol% granite

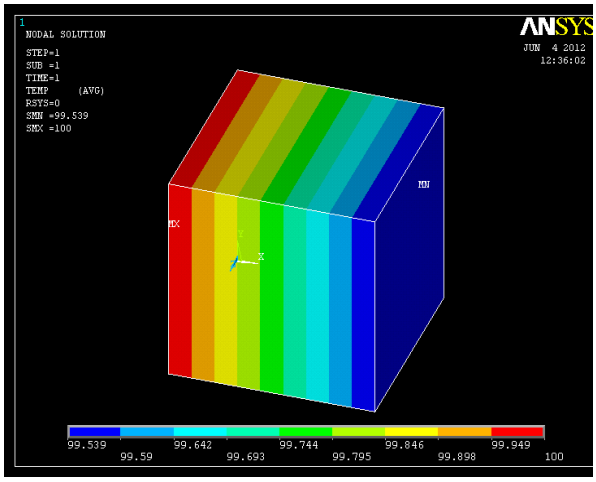

Fig.4 (e) Temperature profile for composite with particle concentration of 21.6 vol% granite

The values of effective thermal conductivities of the particulate filled epoxy composites with varied proportions of granite obtained using Maxwell's correlation, rules-of-mixture model and GMM model and those obtained from FEM analysis are presented in Table 2. It presents a comparison among the results obtained using these models with regard to the values of effective conductivity obtained experimentally. It is noticed that the results obtained from the finite-element analysis using ANSYS are closer to the measured values of effective thermal conductivity for composites of different filler content.

Table 2. Effective thermal conductivities values obtained for different models

Models	Filler content (Vol.%)	Effective thermal conductivities by				
		Rule of mixture (W/m-K)	Maxwell model (W/m-K)	GMM model (W/m-K)	FEM (W/m-K)	Experimental value (W/m-K)
C1	0	0.363	0.363	0.363	0.363	0.363
C2	2.7	0.416	0.382	0.381	0.383	0.392
C3	6.4	0.490	0.410	0.412	0.411	0.423
C4	12.5	0.612	0.458	0.459	0.461	0.473
C5	21.6	0.704	0.539	0.543	0.540	0.548

Table 3.Percentage error with respect to experimental value

Sample	Filler Content (Vol%)	Percentage errors with respect to the experimental value (%)			
		Rule of Mixture (ROM)	Maxwell Model (MM)	GMM model	FEM Model (FEM)
C2	2.7	-6.12	2.55	2.80	2.29
C3	6.4	-15.83	3.07	2.60	2.83
C4	12.5	-29.38	3.17	2.95	2.53
C5	21.6	-28.46	1.64	0.91	1.45

The percentage errors associated with each method for individual composites are given in Table 3. On comparison, it is found that the errors associated with the FEM values with respect to the experimental ones lie in the range of 1.45% to 2.83% and the same for Rules-of-mixture, Maxwell's correlation and GMM model lie in the ranges of -6.12 to -29.38%, 1.64% to 3.17% and 0.91% to 2.95% respectively. It leads to a conclusion that for a particulate filled composite of this kind, the FEM model can very well be used for predictive purpose in determining the effective thermal conductivity for a wide range of particle concentration. Although the distribution of granite particles in the matrix body assumed to be in an arranged manner, it is actually dispersed the resin almost randomly. It is also interesting to note that the incorporation of granite results in improvement of thermal conductivity of epoxy resin.

5. Conclusions

This numerical and experimental investigation on thermal conductivity of granite filled epoxy composites has led to the following specific conclusions: 1. Successful fabrication of epoxy based composites filled with micro-sized granite particulates by hand-lay-up technique is possible. 2. Finite element method can be gainfully employed to determine effective thermal conductivity of these composite with different amount of granite content. 3. The value of effective thermal conductivity obtained for various composite models using FEM are in reasonable agreement with the experimental values for a range of filler contents from about 2.7 vol.% to 21.6 vol.%. 4. The values of thermal conductivity obtained for FEM analysis are in reasonable agreement with respect to the experimental values as well as the values calculated using rule-of-mixture, GMM model and Maxwell's correlation. 5. Incorporation of granite particles results in improvement of thermal conductivity of epoxy resin and there by improves its thermal conduction capability. With addition of 21.6 vol. % of granite, the thermal conductivity improves by about 50%. 6. These composites possess a fairly good potential for application in electronic circuit boards and low cost packaging materials.

References

[1] Hutchings, I.M., 1992. Tribology: friction and wear of engineering materials. CRC Press.
[2] Rothon, R.N., 1999. Mineral fillers in thermoplastics: filler manufacture and characterization. Adv. Polym. Sci. 139, p. 67.
[3] Choy, C.L., Young, K., 1977. Thermal Conductivity of Semi crystalline, Polymers–A Model. J. Polymer 18, p.769.
[4] Hansen, D., Ho, C., 1965. Thermal Conductivity of High Polymers. J. of Poly. Sci. Part A 3, p. 659.
[5] Ishida, H., Rimdusit, S., 1998.Very High Thermal Conductivity Obtained by Boron Nitride-filled Polybenzoxazine. Thermochimica Acta 32, p.177.
[6] Agari, Y., Uno, T., 1986. Estimation on Thermal Conductivities of Filled Polymers. J. of App. Poly. Sci. 32, p. 5705.
[7] Saxena, N.S., Saxena, P.P., Mathew, G., Thomas, S., Gustafsson, M., Gustafsson, S.E., 1999. Thermal Conductivity of Styrene Butadiene Rubber Compounds with Natural Rubber Prophylactics Waste as Filler. J. European Polymer 35, p. 1687.
[8] Procter, P., Solc, J., 1991. Improved thermal conductivity in microelectronic encapsulants. IEEE Trans on Hybrids Manuf Technol 14, p.708.
[9] Zhao, Q., Zhang, B., Quan, H., Yam Richard, C.M., Yuen Richard. K.K., Li Robert, K.Y., 2009. Flame retardancy of rice husk-filled high-density polyethylene ecocomposites. Composite Science and Technology 69, p.2675.
[10] Nayak, R., Dora, P.T., Satapathy, A., 2010. A computational and experimental investigation on thermal conductivity of particle reinforced epoxy composites. Computational Materials Science 48, p.576.
[11] Rout, A.K., Satapathy, S., 2012. Computational and experimental investigation on thermal insulation capabilities of rice husk filled epoxy composites. Computational Thermal Science 4, p.107.
[12] Yung, K.C., Zhu, B.L., Yue, T.M., Xie, C.S., 2009. Preparation and properties of hollow glass microsphere-filled epoxy matrix composites. Composite Science and Technology 69, p.260.
[13] Tognana,S., Salgueiro,W.,Somoza, A.,Pomarico, J.A., Ranea-Sandoval, H.F., 2009. Influence of the filler content on the thermal expansion behaviour of an epoxy matrix particulate composite. Material Science and Engineering B 157, p.26.
[14] Ott, H.J., 1981.Thermal Conductivity of Composite Materials. J. Plastic and Rubber Processing and Application 1, p.9.
[15] Sweeting, R.D., Liu, X.L., 2004. Measurement of thermal conductivity for fiber-reinforced composites. Composites Part A 35, p. 933.
[16] Bagchi, A., Nomura,S., 2006. On the effective thermal conductivity of carbon nanotube reinforced polymer composites. Composite Science and Technology 66, p.1703.
[17] Maxwell, J., 1873. Electricity and Magnetism. Clarendon: Oxford.
[18] Binici, H.,Shah, T., Aksogan, O., Kaplan, H., 2008. Durability of concrete made with granite and marble as recycle aggregates. Journal of Materials Processing and Technology 208, p.299.
[19] Dwivedi, R.D., Goel, R.K., Prasad, V.V.R., Sinha, A., 2008. Thermo-mechanical properties of Indian and other granites. Int. Journal of Rock Mechanics & Mining Sciences 45, p.303.
[20] Turner, M.J., Clough, R.W., Martin, HC, Topp L.J., 1956. Stiffness and Deflection Analysis of Complex Structures. J. of the Aeronautical Sciences 23, p.805.

Available online at www.sciencedirect.com

SciVerse ScienceDirect

Procedia Engineering 00 (2012) 000–000

Procedia Engineering

www.elsevier.com/locate/procedia

5th BSME International Conference on Thermal Engineering

Temperature monitoring and CFD Analysis of Data Centre

N.M.S. Hassan [a] *, M.M.K. Khan[a], M.G. Rasul[a]

[a]*Central Queensland University*
Power and Energy Research Group
Institute for Resource Industries and Sustainability (IRIS)
School of Engineering and Built Environment
Rockhampton, Queensland 4702, Australia

Abstract

This paper presents a computational fluid dynamics (CFD) analysis of airflow, temperature and pressure distribution of the data centre located at CQUniversity, Rockhampton Campus, Australia. The data centre has been modelled and analyzed using CFD code 'Fluent' to study the effectiveness of thermal cooling within the data centre. CoolSim- software was used for designing a graphical user interface (GUI) that allows data centre components to be positioned, sized and characterized in a plan view. The CFD model based on thermal mass and energy balance principles was used to simulate the data centre for predicting the energy consumption, pressure and temperature in a data centre. The effect of various data center parameters on the temperature distribution and the flow field was investigated. The parametric and optimization techniques were used to determine the best possible layout for cooling strategies. The simulation results predict the high temperature zone within the computer rack in the data centre, and provide a detailed 3D analysis of the movement of cold air through the data centre. The results also provide the performance analysis of computer room air conditionings (CRACs) with detailed rack-by-rack inlet and exit temperatures and 3D thermal mapping of the data centre and racks highlighting trouble areas. The model developed is capable of evaluating the airflow rates and thermal loads for optimizing and designing a new or existing data centre.

Keywords: Data centre modeling; Computational fluid dynamics (CFD); CoolSim; Temperature distribution.

1. Introduction

A data centre is a facility used to accommodate computer systems and associated components, such as telecommunications and storage systems. It usually includes redundant or backup power supplies, redundant data communications connections, air conditioning, fire suppression and security devices. On average, existing data centres have required around twice the amount of cooling but many of them are still facing problems with high temperature zones created within the data centres [1]. The technology advances with servers and networking equipment enables the equipment that filled a room, can now be placed in a single rack; creating excessive power and heat problems. Power densities are increasing with many server racks already exceeding 10kW and future predictions of 20kW, 30kW and beyond meaning the traditional computer rack configuration is simply unable to effectively manage. More cooling equipment requires more electrical power to drive it, yet with rising electricity costs, and concerns over carbon footprint, companies are trying to reduce their power use [1].

* Corresponding author. Tel.: +61 7 4923 2123
E-mail address: n.hassan@cqu.edu.au

The cooling infrastructure is an important part of a data center. The complicated connection of chillers, compressors and air handlers create the best possible computing environment, ensuring the long life of the servers installed within and the strength of the organization they support [1]. The common scenario for data centre infrastructure is the deployment of high density equipment. But in most cases data centers are not sufficiently capable of handling the additional cooling requirements resulting from these deployments due to the unwanted conditions such as recirculation or mixing of hot and cool air, poorly controlled humidity and costly wasted cooling capacity [1]. Traditional data centres are not efficient due to poor airflow management. Since airflow and pressure are not visible, it is not easy to develop a plan for improving airflow management without the use of an airflow management modelling tool. As the power density continues to increase in data centers, development of effective and efficient cooling methods becomes necessary.

The main concern for data centre users was the operating reliability. Energy efficiency was less of a priority. Hence most of the data centers were designed based on the worst case scenario [2]. However, with increase in power densities in the data centre reaches to levels that lead to limitations, energy efficiency is now observed as a way to solve these problems. The benefits of reducing energy inputs at various levels are [2]:

- Reduction in costs associated with power use
- Lesser demand on the utility grid, hence improved reliability

CQUniversity's main data centre is located at Information Technology Department (ITD) buildings 19/G-33 at Rockhampton Campus that has no windows and minimal fresh air. This is due to fact that data centers are primarily designed for IT equipment and not for the human. It is important that the operating conditions within the facility are based on the manufacturer's specifications. The American Society of Heating, Refrigerating and Air-Conditioning Engineers (ASHARE) have anticipated the thermal guideline for data centre environments. It has recommended that the server inlet temperature should be between 20^0 C to 25^0 C. ASHRAE guidelines [3, 4] was followed in this study as a thermal guideline for data processing environments.

A number of researchers have undertaken studies on the dynamic optimization of the data centre thermal environment. They mostly focused on the layout design of the data centre. Bash et al. [5] have investigated the need for placing the critical equipment of a data centre at a closer distance. Nakao et al. [6] studied the data centre cooling configurations with different variations. These configurations were - the under floor supply with ceiling exhaust, under floor supply with horizontal exhaust, overhead supply with under floor exhaust and the overhead supply with horizontal exhaust. Noh et al. [7] used three variations for designing the data centre for 5-6 kW rack loads. They used these configurations in telecommunications applications which included under floor supply with ceiling exhaust, overhead supply with under floor exhaust and overhead supply with wall exhaust. Both of these studies have suggested that the under floor supply with a ceiling return is the best option. Schmidt and Iyengar [8] also studied the airflow configurations for high density data center clusters. They used both underfloor and overhead airflow configurations. In this investigation, they detected high temperature gradients in the inlet temperature and they also found that these temperature gradients are in some instances pronounced more in underfloor configurations that the overhead supply design. Therefore, the under floor supply with ceiling return has been chosen for modelling in this study. The cabinet layout scheme, hot aisle/cold aisle is a traditional practice within a data centre for data centre architects, engineers, and end users [1]. This scheme was selected for designing the computer rack configuration. It uses air conditioners, fans, and raised floors as a cooling infrastructure and concentrates on separation of the inlet cold air and the exhaust hot air [1].

Fig.1 shows the hot aisle/cold aisle layout configuration. In the hot aisle/cold aisle, the racks are placed into a series of rows, standing on a raised floor. The front of the racks faces each other and become cold aisles, due to the front-to-back heat dissipation of most IT equipment. Computer Room Air Conditioners (CRACs) situated around the perimeter of the room or at the end of hot-aisles. CRACs deliver cold air under the raised floor. This cold air enters room through perforated raised floor vent tiles and passes through the racks and gets heated up. This hot air then returns to CRAC intake [1, 2].

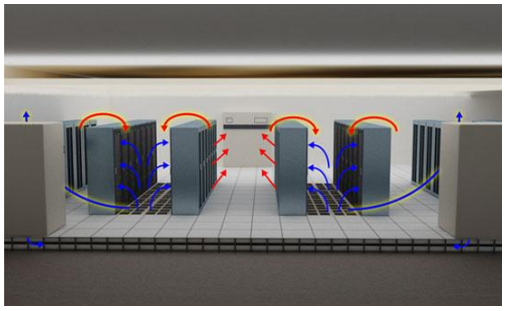

Fig. 1. Hot aisle/Cold Aisle Layout [1]

Energy cost has now become one of the important issues in data centre design as it continues to rise and concerns about global warming due to carbon emissions. The increase in computational capabilities of data centres has resulted in corresponding increases in rack and room power densities [9, 10]. Therefore, it is required to know the phenomena which reduce the energy consumption when designing data centres. CFD is the useful tool for predicting the strategies to optimize the data centre cooling and power savings.

The aim of this project is to develop a cooling model of CQUniversity's computer data centre with a focus on developing technologies and strategies that change the dynamics of data centre cooling to energy cost savings. Therefore, the main objective of this study is to develop a CFD model that accurately maps the distribution of pressure, airflow and thermal mapping of the CQUniversity's data centre to improve cooling efficiency.

2. Research Approaches and Data Centre Description

2.1. Research Approaches

The data centre was modelled and analyzed using CFD code "Fluent" to study the effectiveness of cooling within the racks and aisles of the centre. CoolSim- software was used for designing a graphical user interface (GUI) that allows data centre components to be positioned, sized and characterized in a plan view [11]. Modelling of airflow and temperature distribution in the data centre was performed using Fluent [12]. Fig. 2 shows the 3D view of the data centre of CQUniversity, Rockhampton Campus.

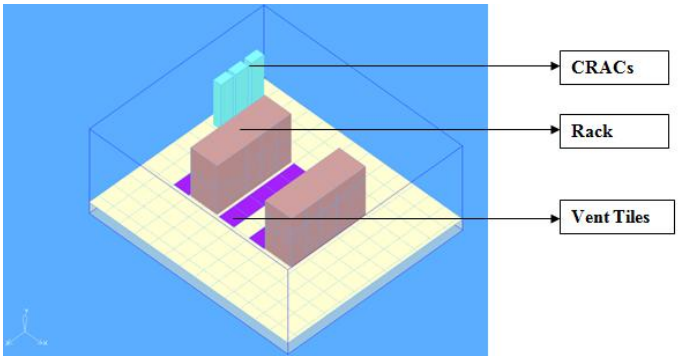

Fig. 2: A 3-D view of a data centre of CQU ITD room

The ITD building (19/G-33) of CQUniversity at Rockhampton has a high-efficiency Heating, Ventilation and Air Conditioning (HVAC) system [13]. Three (down flow type) Computer Room Air-Conditioning (CRAC) units were employed in this room. The raised floor was chosen with the room return facility but no supplemental cooling was selected. The CRACs unit was part of the raised floor room layout with cooling air passing through plenum and venting in the room through vent tiles. The racks were arranged in two rows and can have individual heat load and airflow. Each row consists of 5 racks. Air flow direction and air flow rate were defined for all racks from the specifications model of CoolSim 3.2 software. The front face of rack, which usually was air inlet for the equipment, was placed facing vent tiles. The air-moving device inside the racks was assumed to force air straight through the rack, with a constant velocity across the front and back of the racks. The backside of rack from where hot air passes; faces backside of another rack developing a hot aisle. Each rack was assumed to be a high-performance 3.46 kW rack, with a rack airflow rate of 0.23 m^3/s. This model was considered for hot-humid climate as Rockhampton is in a sub-tropical zone. In this study, 56% openings were chosen for perforated vent tiles.

2.2. *Data Centre Description*

The description of data centre and data centre components, air flow through racks and vent tiles are summarized below.

Data Centre:

Model ID:	Nur-3rdData_Model
Simulation Date:	Mar 7, 2012
Mesh Density:	Medium
Mesh Count:	27812

Data Center Layout:	Raised Floor with Room Return		
Data Center Components:			
	Room Dimensions	8.05 X 7.08 X 2.96	
	Room Floor Area	56.99 sq-m	
	Supply Plenum Height	0.45 m	
	Number of CRAC Units:	3	
	Total Flow Through CRAC Units:	11.704 m^3/sec	
	Supply Air Cooling Capacity:	42055.68 W	
	Number of Rack Rows:	2	
	Total Number of Racks:	10	
	Total Rack Heat Load:	41.12 kW	
	Total Flow Through Racks:	2.562 m^3/sec	
	Number Tile Rows:	3	
	Total Number of Vent Tile:	15	
	Total Flow Through Tiles:	11.707 m^3/sec	
	Ave Flow Through Each Tile Vent:	0.78 m^3/sec 0.78 m^3/sec	
Power:			
	Rack Heat Source:		41.12 kW
	Wall Heat Transfer:		0.89 kW
	Total Cooling Load:		42.01 kW
	Heat Density:		737.18 W/sq-m
	Supply Air Cooling Capacity:		42055.68 W
Temperature Details:			
	Highest Temperature in Data Center Room:		29 ^oC
	Highest Inlet Temperature in Racks rackrow_0_1 Rack number 1:		22 ^oC
Flow Through Tiles:			
	Maximum Flow Through a Vent Tile tilerow_0 Tile number 2:		1.727 m^3/sec
	Minimum Flow Through a Vent Tile tilerow_1 Tile number 4:		0.131 m^3/sec

3. Results and Discussions

The CFD simulation was performed for the model shown in Fig. 2. The results of the room and rack thermal maps and the temperature clouds and the effect on the CRAC return temperatures and CRAC performance and temperature clouds are reported.

The results of room and rack thermal profiles at different plane of the data centre are shown in Fig. 3 through Fig. 9. As discussed earlier, there are 3 CRACs units and the total flow through CRACs is 2.562 m^3/sec. Fig. 3 and Fig. 4 indicate that the thermal profiles were obtained at 3 ft (0.914 m) height and 6 ft (1.83 m) height above the floor respectively. It is seen from these Figures that the temperature rise was found more in higher height (6 ft) than in the smaller height (3 ft). This is shown at the end rack of the data centre. From these Figures, it is evident that the hot exhaust air is being recirculated into the cold aisle and it is mixing with the supplied cold air. This has caused the inlet temperatures of the racks to raise more above the supply temperature. Usually, the flow of air is passing from the vent tiles into to the cold aisle, where the cold air is moved into the server inlets and moved out of the back of the servers into the hot aisle. The hot air is then moved to the sides of the room where it is passed into the CRAC's. Such hot temperature zones cause rise in temperature leading to reliability issues of computer components. Hence it becomes important to employ proper cooling solutions to keep the temperature within the required limits. On the other hand, it is noted that the cooling of any data centre comprises of two

primary components which are the total capacity of cooling system and its related airflow [14].Therefore it is essential to employ both of these parameters to have efficient cooling in the data centre.

Thermal map at mid plane along the width and length at the data centre of CQUniversity are shown in Figure 5 and Fig. 6. Large temperature gradients were observed at outside rack for both cases. Different recirculation pattern was also observed at outside rack. Since hot air leaving into hot aisle is forced into cold aisle from the side as well as from top of the racks.

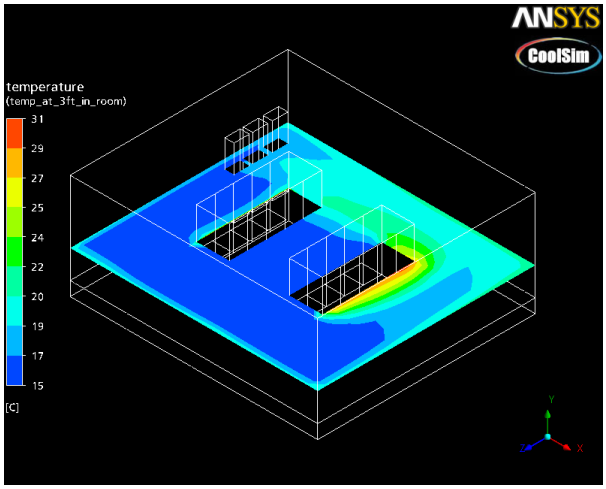

Fig. 3. Thermal map at 3 ft height in the data centre of CQUniversity

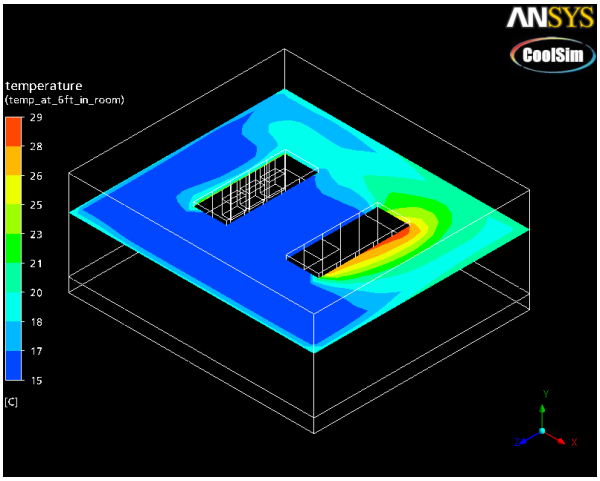

Fig. 4. Thermal map at 6 ft height in the data centre of CQUniversity

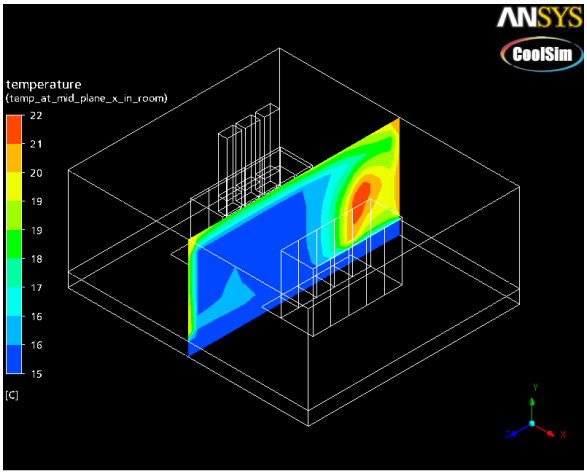

Fig. 5. Thermal map at mid plane along length in the data centre of CQUniversity

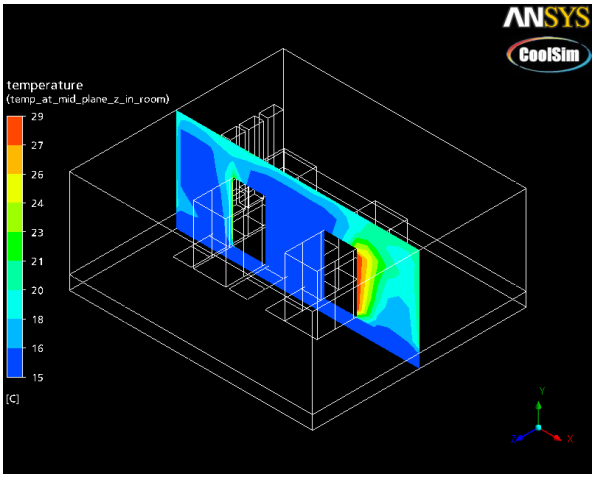

Fig. 6. Thermal map at mid plane along width in the data centre of CQUniversity

Thermal map at three quarter plane along the length and width in the data centre are shown in Fig. 7 and Fig. 8. For both cases, hot and cold air mixing was present, but high temperature zone was found along the width of the data centre. Maximum temperature around 29^0C was observed at three quarter plane along length. It is due to the flow re-circulating from the exhaust side of the cabinet. This high temperature is located at the back of the 2^{nd} rack of the data centre. On the other hand, the low temperature zone was found along the width at three quarter plane. However, high temperature was also seen at both top corners of the rack above floor on this plane. It is due to the server receiving air that is a combination of room air and air leaving from server outlets, instead of the vent tiles in the raised floor.

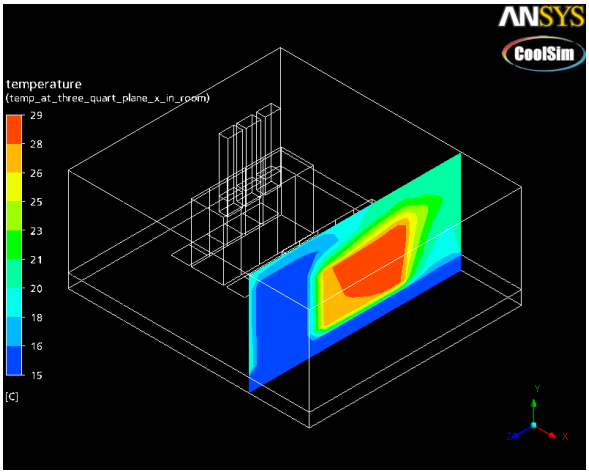

Fig. 7. Thermal map at three quarter plane along length in the data centre of CQUniversity

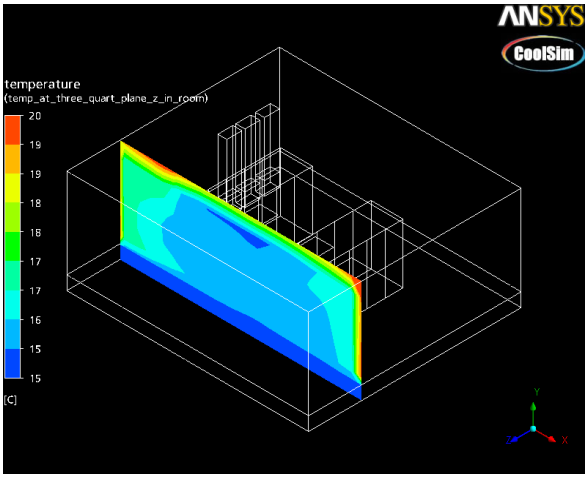

Fig. 8. Thermal map at three quarter plane along width in the data centre of CQUniversity

Rack thermal map is shown in Fig. 9. Figure shows the temperature distribution at both racks along length. This temperature distribution is placed between the back side of the 1st rack and the front side of the 2nd rack. The temperature distributions of both racks were shown nearly 15^0C which is similar to the server inlet temperature but there is one exception at the front section of both racks where the temperature was found slightly higher which is nearly 18^0C-20^0C. This is due to higher dense server causing high recirculation between the inlet and ambient air.

Fig. 10 reports the pressure map in supply plenum. It shows the pressure distribution in the data centre room. As seen from this Fig. 10, the low pressure areas were found at the surroundings of the computer racks. On the other hand very low pressure was observed in the CRACs unit which is nearly -446.18 Pa to -354.86 Pa. As mentioned earlier, the inlet air to the servers is nearly the same temperature as the air at the supply of the CRACs. However, the air in front of the servers at the bottom of the cabinets is moving at a high velocity, causing a low static pressure. Kwok Wu [10] has reported his study that cold aisle efficiently creates a thermal and mass flow boundary between the cold aisle and hot aisle. The cold aisle creates a region for mass to be ensnared, which creates a high static pressure region [10]. Since the cooling flow is increased with increase in power density resulting in an increased airflow to the cold aisle. This is due to cold air entering the racks near the cold aisle region and there is an increase of static pressure of cold air as the cooling flow increases. Lower power density also creates the low static pressure which is due to smaller amount of air-flow from the CRACs ensuing in an insufficient build up of static pressure near the floor of the cold aisle region. This is caused by the higher server inlet temperatures at the servers situated close to the floor.

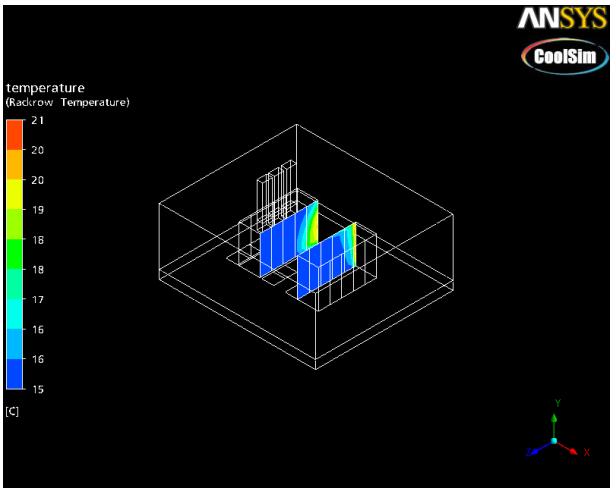

Fig. 9. Rack thermal maps in the data centre of CQUniversity

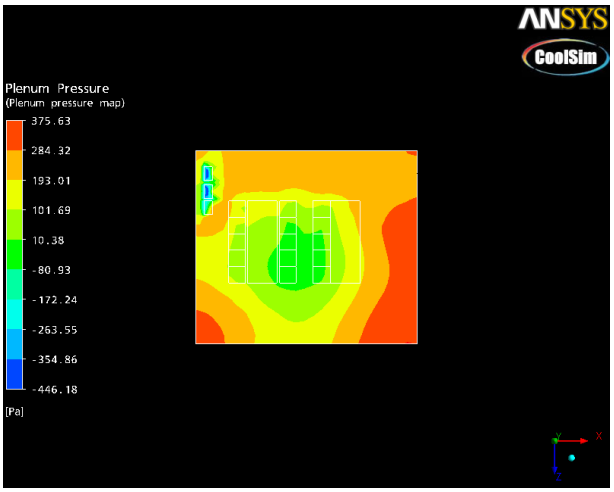

Fig. 10. Static Pressure map in Supply Plenum

The effectiveness of data centre cooling is measured by its ability to maintain data center equipment from overheating despite of the power density of the room [10]. A server is usually assumed overheated if the inlet temperature exceeds 25°C [10]. Another way to evaluate the effectiveness of this solution is temperature of air returning to CRACs units [2]. The temperature clouds and CRAC return and supply temperatures profiles are illustrated in Fig. 11 through Fig. 14. Rack cooling and air flow distribution through tiles reports are summarised in Table 1 and Table 2. It is seen from Fig. 11 and Fig. 12, the maximum temperature clouds were observed at the back of the 2nd rack of the data centre. As seen, there are already hot zones located at the ends of the rack rows.

Fig.13 and Fig.14 show that the maximum supply and return temperatures were 17^{0}C to 18^{0}C and 27^{0}C to 28^{0}C respectively. As discussed earlier in summery report, the maximum inlet temperature to the racks is found 22^{0}C. On the other hand, Table 1 shows that the inlet and exit temperatures to the racks are 18^{0}C and 31^{0}C. These temperatures limits are also meeting the ASHRAE guidelines [3, 4].which are show in Table 1 and Table 2. In addition, this low return temperature in turn reduces the load on CRAC and maintains required supply temperatures.

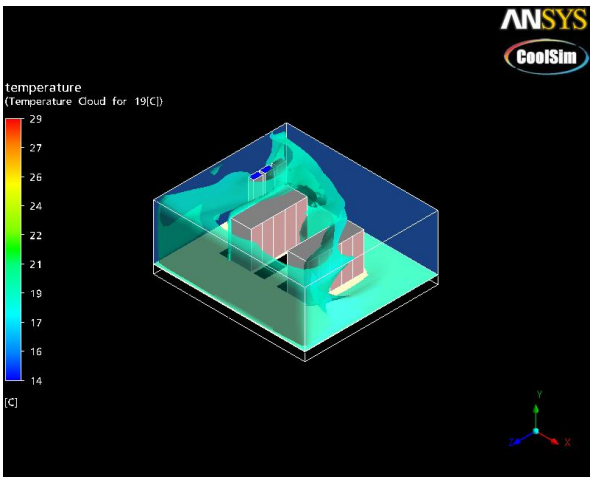

Fig. 11. Low temperature cloud

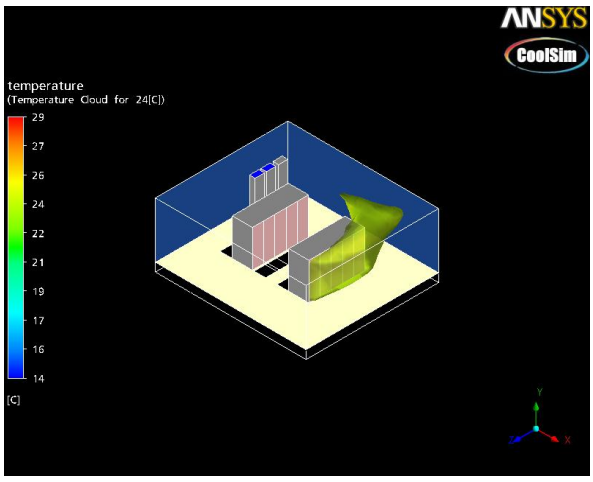

Fig. 12. High temperature clouds

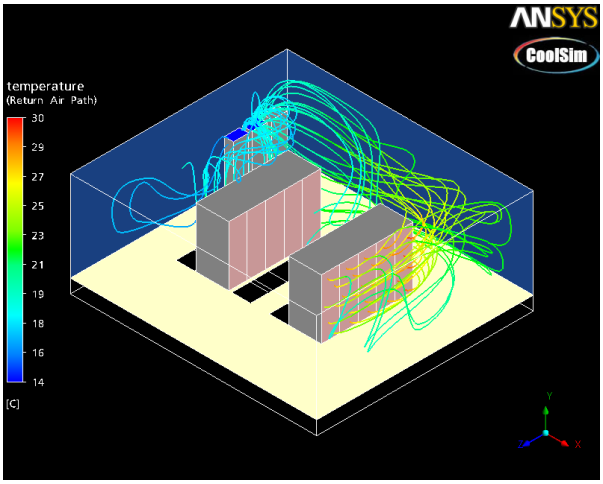

Fig. 13. Return air path

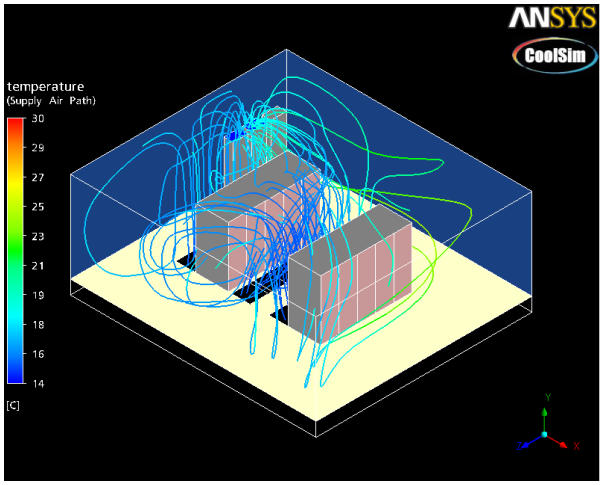

Fig. 14. Supply air path

Table 1: Rack cooling report

Rack Row Name	Inlet Temperature			Ave Exit Temperature (°C)	Flow Rate(m3/sec)	Power (kW)	Cooling Index[#0]	ASHRAE Recommended Inlet Temperature Range for Class I Servers	
	Minimum (°C)	Maximum (°C)	Average (°C)					Recommended[#1] (18 °C - 27 °C)	Allowable[#2] (15 °C - 32 °C)
rackrow_0_1_1 (D , 5)	16	22	18	31	0.225	3.46	0.684	Pass	Pass
rackrow_0_2_1 (D , 6)	15	17	16	28	0.225	3.46	0.857	Pass	Pass
rackrow_0_3_1 (D , 6)	15	16	16	28	0.225	3.46	0.928	Pass	Pass
rackrow_0_4_1 (D , 7)	15	16	16	28	0.23	3.56	0.921	Pass	Pass
rackrow_0_5_1 (D , 8)	15	16	16	29	0.225	3.46	0.910	Pass	Pass
rackrow_1_1_1 (I , 5)	15	18	16	30	0.286	4.73	0.831	Pass	Pass
rackrow_1_2_1 (I , 6)	15	16	15	29	0.286	4.73	0.916	Pass	Pass
rackrow_1_3_1 (I , 6)	15	16	15	29	0.286	4.73	0.953	Pass	Pass
rackrow_1_4_1 (I , 7)	15	15	15	29	0.29	4.82	0.972	Pass	Pass
rackrow_1_5_1 (I , 8)	15	15	15	28	0.286	4.73	0.980	Pass	Pass

[#0] Rack Cooling Index = (Ave CRAC Supply Temp / Maximum Rack Inlet Temp), [#1] ASHRAE 2008 Recommended Inlet Temperature Range for Class-I Severs is 18 °C to 27 °C, [#2] ASHRAE 2008 Allowable Inlet Temperature Range for Class-I Servers is 15 °C to 32 °C.

Table 2: Air flow distribution through tiles

Tilerow Name	Open Area (%)	Flow Rate (m3/sec)	*0 Deviation from Mean Value (%)
tilerow_0_1 (C , 4)	56	0.56	-28
tilerow_0_2 (C , 5)	56	1.727	121
tilerow_0_3 (C , 6)	56	1.637	110
tilerow_0_4 (C , 7)	56	1.468	88
tilerow_0_5 (C , 8)	56	1.245	59
tilerow_1_1 (F , 4)	56	0.503	-35
tilerow_1_2 (F , 5)	56	0.364	-53
tilerow_1_3 (F , 6)	56	0.288	-63
tilerow_1_4 (F , 7)	56	0.131	-83
tilerow_1_5 (F , 8)	56	0.152	-81

tilerow_2_1 (H , 4)	56	0.998	28
tilerow_2_2 (H , 5)	56	0.719	-8
tilerow_2_3 (H , 6)	56	0.595	-24
tilerow_2_4 (H , 7)	56	0.636	-19
tilerow_2_5 (H , 8)	56	0.684	-12

[*0] Deviation from Mean Value = [Tile CFM - Ave Tile CFM] / Ave Tile CFM

4. Conclusion

This study focused on improving and developing a new technology for the data centre industry. It identified the potential high temperature zones within the computer rack in the data centre. The high temperature zones were found at computer racks the along length and width at mid plane of the data centre. Maximum temperature around 29^0C was observed at three quarter plane along the length of the data centre and it was located at the back of the 2nd rack of the data centre. This is due to the flow re-circulating from the exhaust side of the computer rack. The average supply and return (path) temperatures of the CRACs unit were found to be 18^0C and 28^0C respectively and the maximum inlet and exit temperatures to the rack were observed as 18^0C and 31^0C. These temperatures limits were compared with the ASHRAE guidelines, which are in good agreement. No overheated server was found as the inlet temperature did not exceed 27°C [10].The low pressure areas were observed at the surroundings of the computer racks. Very low pressure (-446.18 Pa to -354.86 Pa) was also found in the CRACs unit.

The outcome of this study has the potential to contribute to treating Australian data centre problem in a more competitive way. In particular, this project identified the potential high temperature zone within the computer rack in the data centre, and provided a detailed 3D analysis of how cold air moved through the data centre. The results also provided the performance analysis of computer room air conditionings (CRACs), detailed rack-by-rack inlet and exit temperatures and 3D thermal mapping of the data centre and racks highlighting hot zones. This model could be used for a data centre design to develop a cooling strategy for achieving better thermal performance by the Australian industries. The study could also be used further to determine the impact on cooling resources such as equipment layout, air flow rate, floor tiles, heat load distribution, and other supplementary cooling strategies. It also proposed temperature estimates for given rack loadings.

The further study will be to calibrate and validate this model under different operating conditions and thus will predict the energy cost savings using a CoolDoor. CoolDoor is an innovative refrigerated computer rack door that was developed by CoolDoor Pty Ltd, which changes the cooling dynamics of data centres by pre-cooling the ambient air before it enters a rack. The air passes over the heat generating components and re-enters the room near or at the ambient temperature.

REFERENCES

[1] 42U-Data center cooling, 2012, Retrieved 15 February, 2012 from http://www.42u.com/42u-rack-cooling.htm#airflow.
[2] Mulay, V. P., 2009, Analysis of data center cooling strategies and the impact of the dynamic thermal management on the data center energy efficiency, PhD Thesis, The University of Texas.
[3] ASHRAE, 2004, Thermal Guidelines for Data Processing Environments, Atlanta: American Society of Heating, Refrigerating and Air-Conditioning Engineers, Inc.
[4] ASHRAE TC 9.9, 2008, ASHRAE Environmental Guidelines for Datacom Equipment
[5] Bash C. E., Patel C. D. and Sharma R. K., 2003, Efficient Thermal Management of Data Centers – Immediate and Long-Term Research Needs, Intl. J. HVAC&R Res. 9(2)
[6] Nakao, M., Hayama, H. and Nishioka, M., 1991, which cooling air supply system is better for a high heat density room: Under floor or overhead. Proceedings of International Telecommunications Energy Conference (INTELEC) 12(4), p. 393-400.
[7] Noh H., Song K. and Chun S. K., 1998, The cooling characteristic on the air supply and return flow system in the telecommunication cabinet room. Proceedings of International Telecommunications Energy Conference (INTELEC) 33(2), p. 777-84.
[8]Schmidt, R., and Iyengar M., 2005, "Comparison between Underfloor Supply and Overhead Supply Ventilation Designs for Data Center High-Density Clusters," ASHRAE Transactions, 113 (Part 1)
[9] Patterson, M. K. and Fenwick, D., 2008, The State of Data Center Cooling: A review of current air and liquid cooling solutions, Intel Corporation.
[10] Kwok, Wu, 2008 A comparative study of various high density data center cooling technologies, MSc Thesis, Stony Brook University.
[11] CooSim Inc. version 3.2, 2011, User manual.
[12] ANSYS 13.0, 2010, User manual.
[13] Hassan, N. M. S., Khan, M. M. K., Rasul, M.G. and MTO Amanullah., 2012, Thermal Performance Modelling of Data Centre – A case study, the 9th International Conference on Heat Transfer, Fluid Mechanics and Thermodynamics (HEFAT), 16 – 18 July 2012 , Malta.
[14] Bemis P. and Marshall L., 2010, Improving data center PUE through airflow management, Applied Math Modeling Inc., Concord, NH, USA.